DEPARTMENT OF INDUSTRIAL ENGINEERING

Doctoral School in Materials, Mechatronics and Systems Engineering

XXXVIII *Cycle*

Development of detectors for the monitoring of mixed radiation fields

SUPERVISORS:
Prof. Alberto Quaranta
Prof. Gian-Franco Dalla Betta

PH.D. CANDIDATE:
Matteo Polo

ACADEMIC YEAR 2025/2026

TITLE:
Development of detectors for the monitoring of mixed radiation fields

PH.D. CANDIDATE:
Matteo Polo

SUPERVISORS:
Prof. Alberto Quaranta
Prof. Gian-Franco Dalla Betta

MEMBERS OF THE COMMITTEE:
Prof. Lucio Pancheri
Prof. Passeri Daniele
Dr. Cinausero Marco

DATE:
April 16^{th}, 2026

LOCATION:
Department of Industrial Engineering, University of Trento, Povo, Trento, Italy

Abstract

Scintillators and solid-state radiation detectors play a crucial role in high-energy physics, medical imaging, and clinical dosimetry, where requirements such as radiation hardness, geometric flexibility, and detection efficiency are increasingly demanding. This work presents two complementary developments addressing these challenges through advanced materials and detector design.

First, an innovative thermal neutron detection and imaging device based on 3D silicon sensor technology is investigated within the INFN HYDE2 project. The detector features a microstructured geometry with deep cavities filled with neutron converter materials, designed to enhance neutron capture efficiency while maintaining compatibility with pixelated readout electronics. A comprehensive simulation framework combining GEANT4, TCAD Sentaurus, and Allpix^2 is employed to optimize the cavity geometry by evaluating neutron capture probability, charge generation, transport, and collection efficiency. The integration of detailed particle interaction modeling with advanced charge transport simulations enables an efficient exploration of detector geometries and accurate estimation of performance metrics. The results provide valuable guidelines for optimizing neutron detection efficiency and demonstrate the effectiveness of the proposed multiscale simulation approach.

In parallel, we report the optical and radioluminescent characterization of a novel 3D-printable nanocomposite scintillator based on a photocurable polymer matrix loaded with metal halide perovskites. The material is fabricated via stereolithography, enabling the realization of complex and patient-specific detector geometries. Optical properties were investigated through

spectrofluorimetric analysis and UV–vis transmittance measurements to assess spectral compatibility and transparency in the scintillation-relevant range. Radioluminescence was evaluated under alpha-particle excitation and proton irradiation at different energies, including tests performed under therapeutic proton beams in a clinical environment. Comparative measurements with a commercial plastic scintillator demonstrate promising performance, highlighting the potential of the proposed material for personalized dosimetry and advanced clinical radiation detection.

Overall, these studies contribute to the development of next-generation radiation detectors with enhanced performance, adaptability, and applicability in both clinical and scientific environments.

Contents

List of Figures

List of Tables

List of Abbreviations

Ba	University of Bari
CCE	Charge Collection Efficiency
DRIE	Deep Reactive Ion Etching
GEN	Genesis resin
INFN	National Institute for Nuclear Physics
LNL	National Laboratories of Legnaro
PMT	Photomultiplier tube
PSD	Pulse Shape Discrimination
PSS	Polysiloxane-based resin
PVK	Perovskite

List of Symbols

α	alpha particle
e^-	electron
p^+	proton
n^0	neutron
γ	gamma ray
D	Cavity distance
R	Cavity radius

List of publications

The following publications were produced during my PhD program and represent research works in which I am an author or co-author:

1. M. Polo, J. Ye, L. Pancheri, *et al.*, "Optimization of a 3d micro-structured neutron imaging sensor through combined simulation approaches," *Journal of Instrumentation*, vol. 21, no. 02, p. C02015, 2026

2. M. Polo, J. Ye, R. Mendicino, *et al.*, "Simulating the performance of a 3d silicon sensor for neutron detection," in *Journal of Physics: Conference Series*, IOP Publishing, vol. 3130, 2025, p. 012 016

3. J. C. Delgado, F. Pino, S. Moretto, *et al.*, "A large neutron/gamma detector based on the ej-276g plastic scintillator read out with a multiple sipm arrays," *Nuclear Instruments and Methods in Physics Research Section A: Accelerators, Spectrometers, Detectors and Associated Equipment*, p. 171 139, 2025

4. J. Ye, M. Polo, R. Mendicino, *et al.*, "Tcad simulation of 3d silicon sensors for thermal neutron imaging," *Journal of Instrumentation*, 2025. DOI: 10.1088/1748-0221/20/02/C02011

5. A. Giuri, A. C. Chekkallur, M. Calora, *et al.*, "3d printed ultra-fast plastic scintillators based on perovskite-photocurable polymer composite," *Advanced Functional Materials*, 2025. DOI: 10.1002/adfm.202417653

6. M. Calora, A. Giuri, N. Vanni, *et al.*, "2d metal-halide perovskite-thin polycrystalline films enable bright and fast scintillations," *ACS Applied Optical Materials*, 2024. DOI: 10.1021/acsaom.4c00115

7. F. Pino, J. C. Delgado, M. Polo, *et al.*, "Characterization of a fast neutron irradiation facility using a stilbene scintillation detector," *Nuclear Technology*, 2024. DOI: 10.1080/00295450.2024.2304993

8. J. Delgado, F. Pino, S. Moretto, *et al.*, "Comparative study of sipm arrays performances for neutron detectors," *IEEE Transactions on Nuclear Science*, 2024. DOI: 10.1109/TNS.2024.3387075

9. J. C. Delgado, C. Provenzano, M. Marra, *et al.*, "Study of a metal-halide perovskite cspbbr3 thin film deposited on a 10b layer for neutron detection," *Journal of Physics D: Applied Physics*, 2024. DOI: 10.1088/1361-6463/ad0569

10. M. Polo, R. Mendicino, A. Quaranta, *et al.*, "Characterization of 3d micro-structured timepix detectors for neutron imaging," in *EPJ Web of Conferences*, EDP Sciences, vol. 288, 2023, p. 10 007

11. F. Pino, M. Polo, J. C. Delgado, *et al.*, "Evidence of fast neutron detection capability of the cllb scintillation detector," *Radiation Physics and Chemistry*, 2023. DOI: 10.1016/j.radphyschem.2022.110494

12. M. Polo, F. Pino, J. C. A. Delgado, *et al.*, "Assessment of a nail detector performance for radiation monitoring applications," *European Physical Journal: Special Topics*, 2023. DOI: 10.1140/epjs/s11734-023-00896-4

Chapter 1

Development of innovative detectors

Nowadays, research on novel and innovative radiation detectors is more active than ever. At the Department of Industrial Engineering of the University of Trento, new sensors are being developed following two fundamentally different approaches. On one hand, the well-established 3D silicon sensor technology is being employed in unconventional ways to detect types of radiation that are typically undetectable by standard silicon-based detectors. On the other hand, efforts are being made to develop detectors using new materials that exhibit characteristics currently difficult to achieve with existing technologies.

This thesis explores both approaches, as the processes involved in testing and characterizing innovative detectors are closely related in both cases. Chapter 3 provides a detailed description of a novel 3D silicon sensor designed for neutron imaging applications. Chapter 4, instead, focuses on an innovative polysiloxane scintillator with perovskite components, developed through additive manufacturing techniques to meet the specific requirements of proton therapy applications. Before entering into the details of the two approaches presented in this work, this chapter introduces the current state of the art, followed by the theoretical background underlying particle detection, which is discussed in Chapter 2.

1.1 Neutron detection

For many years, ^{3}He gas-based detectors have been the primary technology used for thermal neutron detection. ^{3}He is mainly a byproduct of the maintenance of thermonuclear warheads, which contain tritium (^{3}H); tritium decays into ^{3}He over a period of 12 years. The accumulated ^{3}He must be removed to avoid degrading the performance of the warheads. Fortunately, since the end of the Cold War, the production of thermonuclear warheads has decreased. On the other hand, this facts, combined with the high demand for ^{3}He in counter-terrorism applications—particularly for detecting the transport of fissile material—has led to a significant increase in its price and a reduction in its availability for scientific research purposes [1]. Therefore, due to the shortage and cost increase of this gas, other detectors had to be developed [2]. These alternative technologies generally aim to exploit one of the reactions described in Section 2.1.4 to produce charged particles, which are more easily detectable. Some proposed solutions are based on inorganic and organic scintillators with embedded converter materials [3]–[8]. The coupling of these scintillators with a Charge-Coupled Device (CCD)—a pixelated sensor operating in the visible spectrum—makes it possible to perform neutron imaging measurements [9].

1.1.1 Semiconductor-Based Detectors for Neutron Detection

In the case of semiconductors, several solutions have been proposed. One approach involves the direct capture and detection of neutrons within the semiconductor itself, such as $LiInSe_2$, LiSe, and BN [10]–[12]. One of the main challenges limiting the widespread adoption of detectors based on these approaches is the difficulty in producing large-scale devices with the required material purity [13]. Another approach involves coupling a silicon detector with the active material, where the sensor is coated with thin films of neutron converter materials. The main drawback of this solution is its relatively low detection efficiency, $\sim$4% in the case of ^{10}B and $\sim$4.4% in the ^{6}Li, that is due to the limited thickness of the active material that can be used. This constraint arises from the need to avoid self-absorption of the charged particles generated by the reaction [14]–[16].

The best performance in terms of detection efficiency is offered by 3D detectors, in which the silicon bulk is drilled [17]–[22]. The cavities are filled with converter material, where the products of neutron capture are charged particles that can be detected by the sensitive volume around the cavities.

Over the past decade, several research groups have been actively investigating three-dimensional (3D) neutron detectors. The most significant results reported by different research groups are summarized below.

1.1.1.1 Kansas State University

The research group at Kansas State University has been one of the most active in this field. A wide range of detector geometries has been investigated using Monte Carlo simulations, considering different structural configurations and various active materials. Both single-sided and double-sided devices were simulated, yielding theoretical detection efficiencies of 35% and 70%, respectively [15], [23]. However, once the first test structures were fabricated, the measured efficiency was found to be significantly lower. This discrepancy was mainly attributed to the fact that dead layers (e.g., oxide layers) were not included in the simulations, as well as to the inability to achieve a 100% charge collection efficiency throughout the entire sensor volume. For the single-layer device, an efficiency of 16.2% was achieved using sinusoidally shaped trenches [24]. One approach adopted to further increase the efficiency involved the use of multiple detector layers, such that the active region of one layer overlapped with the neutron-converting region of the adjacent layer. Using this multilayer configuration, an efficiency of 45% was achieved, which is comparable to that obtained in two-layer detectors [18], [25]. Due to the high geometrical complexity of these devices, the implementation of a readout electronics system capable of addressing individual pixels is practically unfeasible. Consequently, these detectors are not suitable for neutron imaging applications, but they have been successfully employed in wearable devices to aid in the search and localization of special nuclear materials [26].

1.1.1.2 Lawrence Livermore National Laboratory

Another research group working on 3D neutron detectors is based at the Lawrence Livermore National Laboratory. In this case, an opposite geometry was developed, in which silicon p–i–n micro pillars are embedded directly within the neutron-converting material. Excellent performance was observed for small pillar diameters and pitches below 2 μm, with pillar depths of at least 50 μm [27]. After fabricating the silicon detector structure, conformal deposition of the neutron converter was achieved using Chemical Vapor Deposition (CVD) [28]. In terms of detection efficiency, a value of approximately 48.5% was reported for devices featuring pillars 50 μm in height and spaced by 2 μm [19]. As in the previous case, this technology is not immediately suitable for neutron imaging applications.

1.1.1.3 Rensselaer Polytechnic Institute

Regarding the work carried out at Rensselaer Polytechnic Institute, the adopted approach is based on the use of an *n*-type starting substrate, with a thickness of 50 μm and weak doping corresponding to a resistivity of 50 Ω cm, which constitutes the sensitive volume of the sensor. A second layer, *p*-type with a thickness of a few micrometers and heavily doped (10^{-2} Ω cm), forms the *p*–*n* junction. The cavity structure has a honeycomb geometry, consisting of hexagonal cavities 40 μm deep, fabricated by deep reactive ion etching (DRIE). The resulting sensors exhibited excellent electrical properties, characterized by very low leakage currents. As for neutron detection performance, an efficiency of approximately 26% was achieved by filling the cavities with ^{10}B [20]. Although the results are very promising, this technology is not yet readily applicable to neutron imaging applications.

The studies and results obtained at the **University of Trento**, in collaboration with the **Istituto Nazionale di Fisica Nucleare (INFN)** and the **Bruno Kessler Foundation (FBK)**, are presented in Chapter 3.

1.2 Scintillation Materials

Scintillators are extensively used in a wide range of application fields, spanning from medical imaging, such as X-ray radiography, computed tomography (CT), and positron emission tomography (PET), to security systems for luggage and cargo screening at transportation hubs. In addition to medical applications, scintillators are also employed in nondestructive testing, nuclear safety monitoring, and as detectors for high-energy physics experiments in particle accelerators, as well as in many other applications.

Given the widespread use of these materials, research aimed at improving scintillator performance has never ceased. A broad variety of materials has been investigated, including polycrystalline materials, powders, ceramics, single crystals, amorphous materials, and composites. Beyond material composition, the physical state of scintillators spans from inorganic crystalline compounds to organic solids, liquids, and even liquefied gases [29].

1.2.1 3D-Printable Scintillators

As previously described, the development of new scintillators can follow several approaches. In this thesis, we focus on the development and characterization of 3D-printable organic scintillators, in which an organic polymer matrix is used as the host material. For this reason, we provide here a brief overview of the state of the art regarding both the matrix materials and the use of perovskites as detectors.

1.2.1.1 Perovskites as Detectors

In the literature, primary interest in perovskites with general formula AMX_3, where A is a monovalent cation (e.g., alkylammonium or alkali metals), M is a divalent metal (e.g., Pb, Sn, or Ge), and X is a halogen (e.g., Cl, Br, or I), such as $CsPbBr_3$, has largely focused on their use as active materials in photovoltaic cells. However, in recent years, due to their large charge carrier mobility, low cost, good γ-ray hardness, and strong stopping power, they have also become attractive for radiation detection applications [30]–[32].

For radiation detection, inorganic perovskites provide high X-ray stopping power due to the high atomic numbers of their constituent elements (e.g., Pb, Br, and I). For example, $CsPbBr_3$ is a high-Z compound with an effective atomic number of $Z_{\text{eff}} = 65.9$. Single-crystal $CsPbBr_3$ detectors for X-rays and high-energy γ-rays have demonstrated excellent energy resolution, comparable to commercially available detectors [33], [34].

As radiation detectors, perovskite-based scintillators could, in principle, offer unique advantages over conventional scintillating materials in terms of performance, low cost, flexibility, high quantum yield, strong absorption, and fast response (less than 20 ns) [35]. Fast-response scintillators are particularly strategic for applications such as medical imaging in positron emission tomography and high-energy physics experiments at high-luminosity colliders. Moreover, perovskite-based scintillators offer the possibility of tuning the photonic emission in the visible spectrum through modifications of the material's anionic component, thereby improving coupling with photodiodes [36].

Initially, the light yield of single-crystal $CsPbBr_3$ scintillators at room temperature was very low under γ-ray excitation, i.e., $<$330 Ph/MeV [37]. Research efforts in the fabrication of single crystals and nanocrystals of $CsPbX_3$ have, over the years, led to promising results, including low detection limits [13 nGy/s for a thin-film device, much lower than the typical dose used in X-ray diagnostics (5.5 μGy/s)], very fast X-ray response (4.6 ns) [36], and high scintillation light yield at both room and cryogenic temperatures [38].

Highly sensitive scintillator screens for X-ray imaging using $CsPbX_3$ nanocrystals have also been reported [36].

Most of these encouraging results concern scintillation induced by X-rays, γ-rays, or α particles in single crystals, whose growth is time-consuming and limits their application in flexible architectures.

Preliminary work on thin perovskite films is described in [39]. The results obtained there form the basis for the SHINE project, described in 4, where the perovskite are embeded in a polymeric matrix.

1.2.1.2 Polymeric matrix

One of the most commonly employed materials in plastic scintillators is polyvinyltoluene (PVT). This material is the basis of the EJ-212 detector, which is used in this thesis as a reference for the comparison of other scintillator performances. According to the datasheet, PVT exhibits a light yield of 10,000 photons/MeV and a maximum emission peak at 420 nm [40]. These characteristics make it an excellent scintillator. However, one of the most critical issues faced by scintillators based on a carbon chain is their low radiation resistance.

In the case of PVT, after an exposure of 50 kGy[1] [41], yellowing of the scintillator is observed, leading to a decrease in light yield. This effect is due to the fact that the incident radiation, in addition to inducing scintillation, is also capable of breaking chemical bonds. Scission of the C–H bond produces free radicals and hydrogen release from the polymer, and the residual material becomes enriched in unsaturated carbon bonds. These carbonaceous species act as color centers in the polymer, causing a reduction in the light yield. Damage in polymers occurs at lower doses compared to inorganic materials, due to the lower binding energy of organic compounds [42].

For this reason, efforts have been devoted in recent years to the development of new materials able to overcome these limitations. In particular, polysiloxanes have been proposed [43]–[45]. These are polymers composed of repeating siloxane units (-O-R_2Si-O-SiR_2-,). Si–O-based polymers exhibit outstanding features that are not achievable with C-C-based molecules. Their physical properties arise from the flexibility of the siloxane backbone, induced by the long Si–O bond (1.64 Å compared to 1.54 Å for C–C or 1.43 Å for C–O) and the low Si–O torsional barrier. In rigid polymers, solvent casting or extrusion techniques force polymer chains into non-equilibrium conformations, inducing residual stresses that are later released through craze formation. In contrast, silicone rubbers, owing to their elastomeric nature, relax intrinsically to equilibrium conformations, thus avoiding the formation of microcracks.

[1] 1 Gy corresponds to radiation depositing one joule per kilogram of matter.

On the other hand, the flexibility of the Si–O–Si bridge does not imply bond weakness. The thermal stability and chemical inertness of these polymers are explained by the Si–O bond dissociation energy of 4.61 eV, compared to 3.59 eV for C–C and 3.71 eV for C–O bonds. This property arises from the partial ionic nature of the Si–O bond [42]. The excellent radiation hardness, up to a dose of 54 kGy from a γ source, was confirmed and reported in [41], where it is shown that after irradiation the scintillator does not exhibit significant variations in its optical properties, unlike what is observed for EJ212.

This silicon-based matrix, in which the perovskites are embedded, constitutes the foundation of the detectors developed within the **SHINE project** (see Chapter 4), which aims to combine the excellent properties of PVKs and polysiloxanes within a single device.

Chapter 2

Introduction to radiation detectors

In nature, there are multiple sources of radiation. This chapter presents the main mechanisms through which radiation interacts with matter. These interaction processes form the basis for the operation of radiation detectors. The purpose of a detector is to interact with incoming radiation and produce a measurable signal, which can then be processed to extract the relevant information. Unless otherwise stated, the information was obtained from [46], [47].

2.1 Interaction of radiation with matter

In this section, the interaction mechanisms of different types of radiation with matter are examined in detail. Radiation can be categorized into two main groups based on their electric charge:

- **Charged particles:** heavy charged particles such as alpha particles (α or He^{+2}) and protons (p^{+}) or lighter as electrons (e^{-});
- **Neutral particles:** neutrons (n^{0}), X-rays, and gamma rays (γ).

Charged particles primarily interact with matter through Coulomb interactions. In contrast, neutral particles, lacking electric charge, interact with matter via different mechanisms. The following subsections provide details on the processes that govern the interaction of radiation with matter.

2.1.1 Heavy Charged particles

Heavy charged particles primarily interact through Coulomb interactions between their electric charge and the electrons of the atoms in the medium. Such interactions can result in either the excitation of an electron to a higher energy state or the ionization of the atom by removing the electron.

The quantity that describes the energy lost by the particle along its trajectory is known as the *linear stopping power*, denoted by S, and is given by the Bethe formula, shown in (2.1):

$$S = -\frac{dE}{dx} = \left(\frac{e^2}{4\pi\epsilon_0}\right)^2 \frac{4\pi z^2 N_A Z\rho}{m_e c^2 \beta^2 A}\left[\ln\left(\frac{2m_e c^2\beta^2}{I}\right) - \ln(1-\beta^2) - \beta^2\right] \tag{2.1}$$

where $v = \beta c$ is the velocity of the incident particle, ze is its electric charge, and Z, A, and ρ are the atomic number, atomic mass, and density of the target material, respectively. N_A is Avogadro's number, m_e is the electron mass, and I is the mean excitation energy of the target material. The second and third terms within the square brackets are relativistic corrections, which become significant when $\beta > 0.1$.

Furthermore, the formula (2.1) can be used to determine the range R of heavy charged particles, given their initial kinetic energy T:

$$R = \int_T^0 \left(-\frac{dE}{dx}\right)^{-1} dE \tag{2.2}$$

If the energy loss is plotted as a function of the penetration depth, the well-known Bragg curve is obtained. Figure 2.1 shows a typical example for an α particle. As can be observed, the energy loss is initially low, then increases with distance, reaching a maximum (the Bragg peak) before dropping to zero as the particle comes to rest.

By further analyzing Eq. 2.1, it can be observed that different charged particles exhibit different values of $-\frac{dE}{dx}$. In particular, charged particles

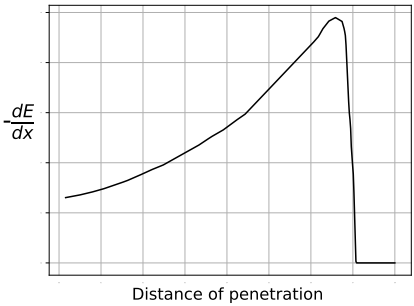

FIGURE 2.1: Bragg curve of an α particle penetrating a target. The energy deposition increases with depth, reaches a peak, and then drops to zero as the particle is completely stopped.

with the same velocity but different electric charges lose their kinetic energy at different rates. For instance, an α particle loses energy more rapidly than a proton when both have the same velocity, due to its higher charge.

Another important factor is the linear dependence on the target material's density ρ. Materials with higher density result in a higher stopping power, meaning charged particles lose energy more rapidly in denser media.

These considerations imply that by studying the energy loss as a function of the incident particle energy, it is possible to infer the type of particle. This relationship is illustrated in Fig. 2.2.

Additionally, the figure shows that all particles tend to approach a constant value of energy loss, which corresponds to a minimum in the stopping power curve—typically around 2 MeV/(g/cm^2) in low-density materials. Particles exhibiting this minimum energy loss are commonly referred to as *Minimum Ionizing Particles* (MIPs). Electrons often fall into this category; however, due to their relatively low mass, they must be treated as relativistic particles. Their interaction with matter differs significantly from heavier particles and is discussed in detail in Section 2.1.2.

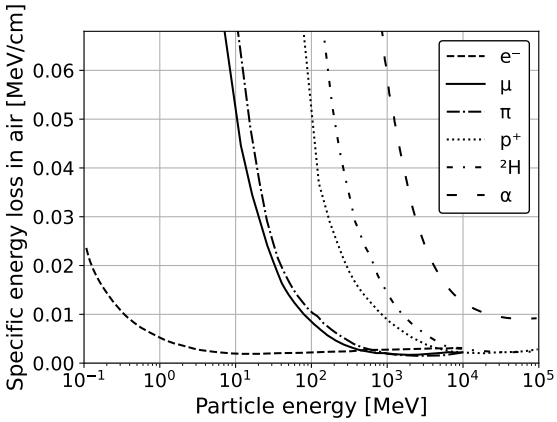

FIGURE 2.2: Variation of the specific energy loss in air as a function of the energy of charged particles.

2.1.2 Electrons

As previously described, electrons—due to their low mass—can travel at relativistic velocities. Because of this, they are easily deflected and can be readily accelerated or decelerated. It is well known that accelerated charged particles emit radiation, a phenomenon referred to as bremsstrahlung. For this reason, the total energy loss of an electron consists of two main contributions: collisional losses (col) and radiative losses (rad). The total energy loss per unit length can thus be expressed as:

$$\frac{dE}{dx} = \left(\frac{dE}{dx}\right)_{\text{col}} + \left(\frac{dE}{dx}\right)_{\text{rad}} \tag{2.3}$$

The detailed expressions for these two components are provided in (2.4) and (2.5). Dove For electron energies below 1 MeV, the radiative losses are negligible.

$$\left(\frac{dE}{dx}\right)_{\text{col}} = \left(\frac{e^2}{4\pi\epsilon_0}\right)^2 + \frac{2\pi N_a Z\rho}{m_e c^2 \beta^2 A}\left[\ln\left(\frac{E(E+m_e c^2)^2\beta^2}{2I^2 m_e c^2}\right) + (1-\beta^2) - \left(2\sqrt{1-\beta^2} - 1 + \beta^2\right)\ln 2 + \frac{1}{8}\left(1-\sqrt{1-\beta^2}\right)^2\right] \quad (2.4)$$

$$\left(\frac{dE}{dx}\right)_{\text{rad}} = \left(\frac{e^2}{4\pi\epsilon_0}\right)^2 \frac{Z^2 N_a \left(E+mc^2\right)\rho}{137 m_e^2 c^4 A}\left[4\ln\frac{2(E+m_e c^2)}{m_e c^2} - \frac{4}{3}\right] \quad (2.5)$$

2.1.3 Gamma rays

The γ rays can interact with matter through three different mechanisms. Depending on their energy and the atomic number (Z) of the target material, one of these effects tends to dominate. The three mechanisms are:

- Photoelectric effect
- Compton scattering
- Pair production

Figure 2.3 shows which of the three interaction processes is dominant as a function of the gamma-ray energy (E_γ) and the atomic number (Z) of the material.

2.1.3.1 Photoelectric Absorption

In this effect, the incident photon is completely absorbed by one of the bound electrons in the target atom. As a result, the electron gains sufficient energy to be ejected from its orbital. The photoelectron that is emitted carries an energy given by:

$$E_{e^-} = E_\gamma - E_b \quad (2.6)$$

where E_b is the binding energy of the electron and $E_\gamma = h\nu$ is the energy of the incident photon. The resulting vacancy may lead to the emission of

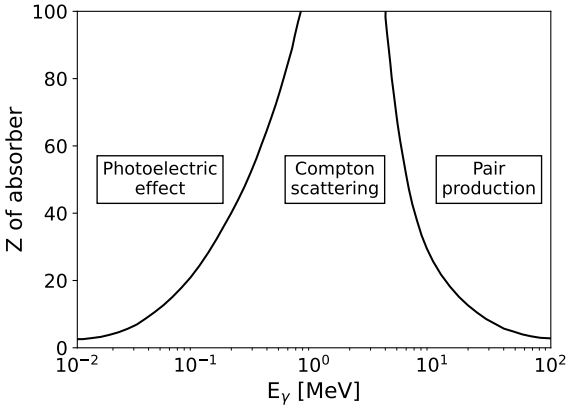

FIGURE 2.3: Graphical representation of the dominant interaction process of gamma rays as a function of gamma-ray energy (E_γ) and the atomic number Z of the material. The two lines represent the values of Z and E_γ at which two interaction processes have equal probability.

characteristic X-rays, due to the transition of another electron from a higher energy level or from the continuum to fill the vacancy.

The photoelectric effect is predominant at low photon energies. While no exact analytical expression describes the probability of this interaction, a good empirical approximation is given by Equation 2.7. As seen from this relation, increasing the atomic number Z of the target enhances the likelihood of the photoelectric effect. The exponent n in the empirical formula depends on the energy of the incoming photon and typically lies within the range $n \in [4, 5]$, as reported in [48].

$$\sigma_{ph} \propto \frac{Z^n}{E_\gamma^{3.5}} \tag{2.7}$$

2.1.3.2 Compton scattering

As the energy increases, the dominant interaction mechanism becomes the Compton effect. In this process, the incident γ photon is scattered from its original trajectory by an angle θ, interacting with an electron of the target atom. During the interaction, the photon transfers part of its energy to the electron. A graphical representation of Compton scattering is shown in Fig. 2.4.

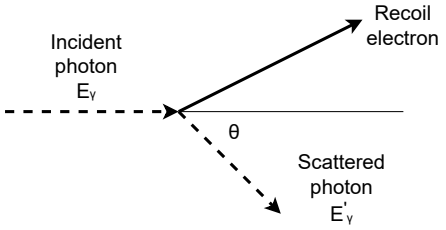

FIGURE 2.4: Graphical representation of Compton scattering.

Based on Fig. 2.4, and by applying the classical conservation laws of energy and momentum, the energy of the scattered photon can be derived as shown in (2.8).

$$E'_\gamma = \frac{E_\gamma}{1 + \frac{E_\gamma}{m_e c^2}(1 - \cos\theta)} \tag{2.8}$$

2.1.3.3 Pair production

In the case of high-energy γ photons, the dominant interaction mechanism is pair production, in which the following reaction occurs:

$$\gamma \rightarrow e^- + e^+ \tag{2.9}$$

This reaction has an energy threshold of $2m_e = 1.02$ MeV. The energy exceeding this threshold is converted into the kinetic energy of the resulting

e^+ and e^-. These two particles can lose energy through bremsstrahlung, emitting photons. If these photons possess sufficient energy, they can generate additional e^+e^- pairs. This chain of reactions leads to what is known as an *electromagnetic shower*, which continues until the remaining energy falls below the pair production threshold. The pair production process becomes the dominant interaction mechanism for photon energies above approximately 10 MeV.

2.1.4 Neutrons

Regarding the interaction of neutrons with matter, due to their lack of electric charge, they can interact only with atomic nuclei through nuclear reactions. Neutrons are classified as thermal (or slow) if their energy is below 0.5 eV, epithermal if their energy is between 0.5 eV and 0.5 MeV, and fast if their energy is above 0.5 MeV. The interaction processes that may occur with matter depend primarily on the neutron energy. The two main reactions are:

- Neutron capture, which is predominant for thermal neutrons
- Scattering, which is predominant for fast neutrons

In the epithermal neutron energy range, the probability of the two reactions is intermediate.

2.1.4.1 Slow neutron

In the case of neutron capture, a reaction occurs in which the nucleus absorbs the neutron. Very often, this reaction produces a metastable nucleus that can return to the ground state by emitting either a particle or a gamma photon (γ). The main reactions of interest in the field of slow neutron detection are the following:

$$
\begin{cases}
^{3}\mathrm{He(n,p)}^{3}\mathrm{H} \quad Q_{\text{value}} = 0.76\ \text{MeV} \\
^{6}\mathrm{Li(n,}^{3}\mathrm{H)}\alpha \quad Q_{\text{value}} = 4.78\ \text{MeV} \\
^{10}\mathrm{B(n,}^{3}\mathrm{H)}^{7}\mathrm{Li} \quad Q_{\text{value}} = 2.79\ \text{MeV} \\
^{10}\mathrm{B(n,}^{3}\mathrm{H)}^{7}\mathrm{Li}^{*} \quad Q_{\text{value}} = 2.31\ \text{MeV} \\
^{157}\mathrm{Gd(n,}\gamma)^{158}\mathrm{Gd} \quad Q_{\text{value}} = 7.937\ \text{MeV}
\end{cases}
$$

The quantity Q denotes the energy released in the reaction. As can be seen, the reaction with ^{6}Li releases the particle (α) with the greatest amount of energy; however, as shown in Figure 2.5, this reaction has the lowest cross-section (σ). Also, in Figure 2.5, it can be observed that the reaction with ^{157}Gd has the highest cross-section, but the drawback of this reaction is that it involves the emission of γ rays. This can sometimes cause issues when gamma contamination must be minimized. Therefore, the choice of one isotope over another must always be carefully made based on the specific requirements of the application.

2.1.4.2 Fast Neutrons

In the case of fast neutrons, the predominant form of interaction is elastic scattering. From basic calculations based on the conservation of momentum and energy, the following equation can be derived, as shown in (2.10):

$$E_r = \frac{4A}{(1+A)^2} \cos\theta\, E_n \tag{2.10}$$

where E_r is the energy of the recoil nucleus, A is the atomic mass of the target nucleus, θ is the scattering angle between the incoming neutron (of energy E_n) and the recoil nucleus.

Considering a head-on collision ($\theta = 0$), the maximum energy transferred to the nucleus becomes:

[0] 1 barn = 10^{-28} m^2.

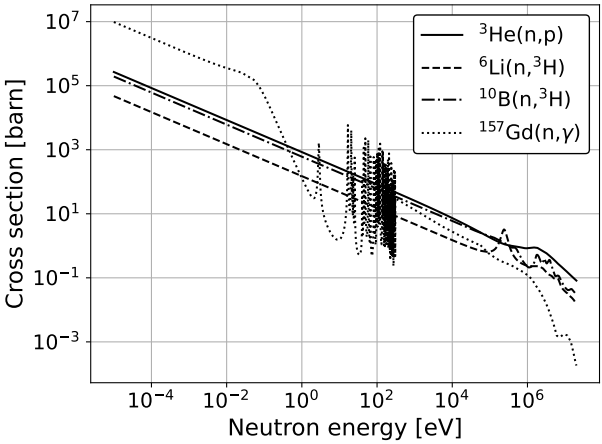

FIGURE 2.5: Neutron absorption cross-sections (1 barn = 10^{-28}m^2) of the main isotopes used for thermal neutron detection. The region around 10^2, eV for ^{157}Gd corresponds to resonances in the cross-section due to excited energy levels of the ^{158}Gd nucleus [49].

$$E_{R_{\max}} = \frac{4A}{(1+A)^2} E_n \tag{2.11}$$

From this expression, it is evident that the maximum energy transfer occurs when the target nucleus has a low atomic mass A. As shown in Table. 2.1, the highest energy transfer occurs with a hydrogen nucleus ($^{1}_{1}$H), and only 18 collisions are needed to thermalize a 2 MeV neutron. In contrast, for a uranium nucleus ($^{238}_{92}$U), approximately 2200 collisions are required.

For this reason, fast neutrons are more likely to transfer energy through collisions with materials containing a high concentration of hydrogen, such as water. Therefore, water is commonly used as a neutron shield. Similarly, fast neutron detectors often rely on materials composed of low-A molecules, such as organic compounds.

Nucleus	$E_{R_{max}} / E_n$	Collisions for Thermalization
$^{1}_{1}$H	1.00	18
$^{2}_{1}$H	0.89	25
$^{4}_{2}$He	0.64	43
$^{12}_{6}$C	0.28	110
$^{238}_{92}$U	0.02	2200

TABLE 2.1: Neutron moderation capability of different nucleus.

2.2 Radiation Detectors

Now that the interaction mechanisms between radiation and matter has been described, we can introduce and discuss the general properties of radiation detectors. This section provides a general overview, while the specific characteristics of the detectors studied in this thesis will be discussed in detail in the following chapters.

2.2.1 Detector Operation Modes

Radiation detectors can operate in two principal modes: *pulse mode* and *current mode*.

2.2.1.1 Pulse Mode

In pulse mode, the detector system is designed to register individual interaction events between the radiation and the sensitive medium. This approach preserves both the timing and the amplitude information of each event.

The equivalent circuit for this mode is illustrated in Fig. 2.6, where R represents the input resistance and C the equivalent capacitance of the system. The time constant $\tau = RC$ determines the response of the circuit. Let t_c be the charge collection time in the detector. Two limiting cases can be identified:

- **Small** RC **(**$\tau \ll t_c$**)**: In this configuration, the output signal $V(t)$ closely follows the current generated by the detector. This mode is ideal when timing information is more critical than energy resolution.
- **Large** RC **(**$\tau \gg t_c$**)**: In this case, the circuit integrates the detector current. The peak amplitude of the signal is directly proportional to the total charge collected, following $V_{\max} = Q/C$. This mode allows the extraction of energy information from the amplitude of the pulse.

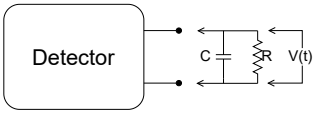

FIGURE 2.6: Equivalent circuit of pulse mode detector

2.2.2 Energy resolution

In many applications involving detectors, one of the main objectives is to measure the energy distribution of the incident radiation. In order to evaluate the ability of a detector to provide this type of information, it is useful to study its behavior in response to a monoenergetic source. In theory, the response in this case should be a Dirac delta[1], but due to the non-ideal nature of the detector, fluctuations are present, resulting in a Gaussian distribution. The quantity used to evaluate the performance of a detector is the "energy resolution", whose definition is given in equation 2.12.

$$R = \frac{FWHM}{E_0} \tag{2.12}$$

Where FWHM indicates the Full Width at Half Maximum and E_0 the centroid of the Gaussian. A graphical representation is shown in Fig. 2.7.

[1] $\delta(x) = \begin{cases} 0, & x \neq 0 \\ \infty, & x = 0 \end{cases}$ such that $\int_{-\infty}^{\infty} \delta(x)\, dx = 1$.

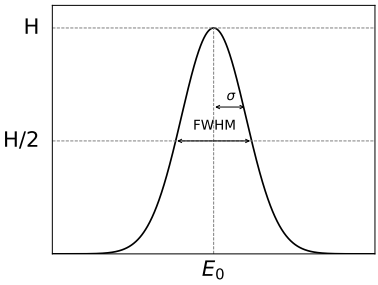

FIGURE 2.7: Definition of energy resolution. From theory, it can be derived that FWHM = 2.35 σ

As discussed previously, in the interaction with radiation in the detector, a discrete number of particles is generated that contribute to the formation of the signal. Thus, it can be stated that the average signal amplitude is given by $E_0 = KN$, where N is the number of generated particles, and K is a constant. For this reason, it is possible to determine the theoretical maximum resolution that can be obtained based on the Poisson distribution, leading to:

$$R\big|_{\text{Poisson limit}} \equiv \frac{\text{FWHM}}{E_0} = \frac{2.35K\sqrt{N}}{KN} = \frac{2.35}{\sqrt{N}} \tag{2.13}$$

This limit is valid only if the generation of the n-th charge is independent of the others. If this is not the case, a lower energy resolution can be obtained, given by the formula:

$$R\big|_{\text{Statistical limit}} = \frac{2.35K\sqrt{N}\sqrt{F}}{KN} = 2.35\sqrt{\frac{F}{N}} \tag{2.14}$$

Where F, called the Fano factor, is defined as:

$$F: = \frac{\sigma_{exp}^2}{\sigma_{Poisson}^2} \tag{2.15}$$

This factor can be calculated and is equal to 0.115 for silicon and 0.13 for germanium [50].

Obviously, the FWHM determined by Poisson statistics represents the lower theoretical limit. In reality, the energy resolution is always worse due to additional noise sources, so the total FWHM is given by the sum of each individual noise contribution, as:

$$(FWHM)^2_{ovreall} = (FWHM)^2_{statistical} + (FWHM)^2_{noise} + ... \tag{2.16}$$

2.2.3 Efficiency

Another fundamental quantity for every detector is its efficiency. Typically, two different types of efficiency are defined: *absolute* and *intrinsic*. The absolute efficiency ϵ_{abs} is defined as

$$\epsilon_{abs} = \frac{\text{number of detected events}}{\text{number of particles emitted by the source}} \tag{2.17}$$

The value of ϵ_{abs} certainly depends on the properties of the detector, but also on the experimental geometry, mainly the distance between the source and the detector. For this reason, the intrinsic efficiency ϵ_{int} has also been introduced, and is defined as:

$$\epsilon_{int} = \frac{\text{number of detected events}}{\text{number of particles hitting the detector}} \tag{2.18}$$

In the case of an isotropic source, the two definitions are related by the following equation:

$$\epsilon_{abs} = \epsilon_{int} \cdot \frac{\Omega}{4\pi} \tag{2.19}$$

Where Ω is the solid angle subtended by the detector with respect to the source placed at a distance d, as shown in the Fig. 2.8.

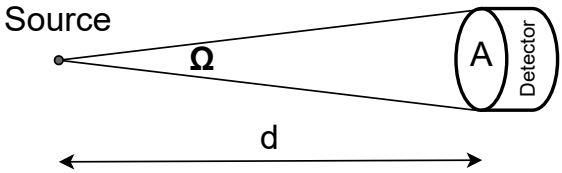

FIGURE 2.8: Geometry of intrinsic efficiency with respect to the detector-source configuration.

Chapter 3

3D silicon detector for neutron imaging

In this chapter, after a brief introduction to neutron imaging and silicon radiation detectors, the solution proposed for neutron detection in neutron imaging applications is presented. This solution was developed within the HYDE2 project (HYbrid DEtectors of neutrons 2) through a collaboration between the University of Trento (UNITN), Fondazione Bruno Kessler (FBK), and the Trento Institute for Fundamental Physics and Applications (TIFPA) [21]. The simulations presented in this work build upon preliminary measurements performed on test samples [51], which exhibited suboptimal performance. Indeed, during the preliminary measurements, a leakage current significantly higher than expected and a neutron detection efficiency considerably lower than that predicted by simulations were observed. Additional simulations were therefore carried out to investigate the origin of this behavior. An innovative approach combining GEANT4 [52], Sentaurus TCAD [53], and Allpix^2 [54] was employed to identify the optimal device configuration in a fast and efficient manner.

Compared to the work presented in [55], the proposed methodology organizes the three simulation tools within a parallel workflow, thereby decoupling nuclear reaction kinematics from charge transport and significantly reducing the overall computational cost. The simulation outputs

are merged only at the final stage. Moreover, in addition to the ^{6}Li converter material considered in [55], this study also investigates the use of ^{10}B as an alternative neutron converter. Comparisons between preliminary experimental measurements and simulation results are also provided.

3.1 Neutron Imaging

Non-destructive techniques can be helpful in revealing the interior of various materials and engineering components. X-ray imaging is the most commonly used method; however, in recent years, neutron imaging has emerged as a complementary technique, as it can provide additional information compared to X-rays [56].

The imaging technique is based on the different abilities of materials to absorb radiation. In this method, the object under analysis is placed between the source and the detector. Due to the varying transmittance of the materials, an image is formed on the detector. A simplified representation of the experimental setup is shown in Fig. 3.1.

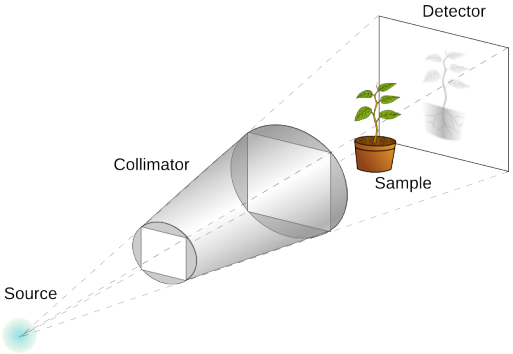

FIGURE 3.1: The principle of a transmittance imaging technique. The detector behind the object measures the transmitted beam [57].

X-rays interact with matter and are absorbed by elements with high atomic numbers (Z), making it difficult to extract useful data from materials with low atomic numbers. For this reason, neutron radiography has gained

attention due to the opposite interaction behavior of neutrons compared to X-rays [47], [58].

In Fig. 3.2, it can be seen that the two techniques provide complementary information. Specifically, in Fig. 3.2a, the metallic parts of the camera are clearly visible, while in Fig. 3.2b, the plastic photographic film is clearly distinguishable - something not detectable using X-rays alone.

(A) X-ray imaging (B) Neutron imaging

FIGURE 3.2: Comparison between X-ray and neutron imaging. [57]

The main factors that have hindered the widespread adoption of neutron imaging are the difficulty of generating and managing a neutron beam and the challenges associated with neutron detection. For this reason, many solutions have been proposed to address the problem of neutron detection, as described previously in Chapter 1. As mentioned above, a solution has been developed within the Hyde2 project. A detailed description of this approach will be provided in Section 3.3, following a brief introduction to silicon detectors.

3.2 Silicon radiation detector introduction

3.2.1 Semiconductor material

Semiconductors are materials that exhibit electrical properties intermediate between those of conductors and insulators. This is primarily due to their relatively small band gap, which in the case of silicon is approximately 1.1 eV. As a result, electrons can be thermally or optically excited into the

conduction band with relative ease. Figure 3.3 graphically illustrates the difference in band gap among insulators, semiconductors, and conductors.

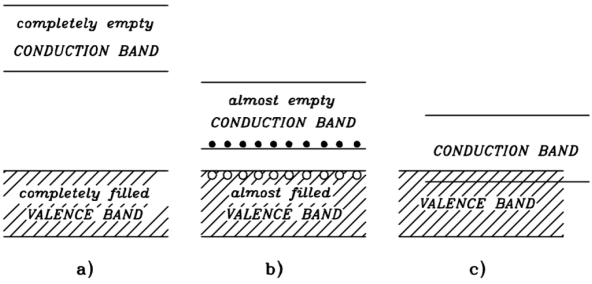

FIGURE 3.3: Energy band structure of (a) insulators, (b) semiconductors, and (c) conductors [50].

This relatively small band gap leads to a significant number of electrons being promoted to the conduction band, thereby enabling excellent energy resolution in radiation detection applications. It is important to note that each electron promoted to the conduction band leaves behind a vacancy—referred to as a hole—in the valence band. This process is known as the generation of an electron–hole pair (e–h pair).

In silicon, the transition between the valence and conduction bands is indirect, meaning that the electron must change its momentum during the excitation process. This requires the interaction with a phonon to conserve momentum. Consequently, the effective energy required to generate an e–h pair in silicon is approximately 3.6 eV.

In practice, pure silicon is rarely used in device fabrication. Instead, small amounts of impurities are deliberately introduced in a controlled process known as doping, to tailor the material's electrical properties. When silicon atoms in the crystal lattice are replaced with donor atoms (such as phosphorus or arsenic), the resulting material is classified as n-type, characterized by an excess of conduction-band electrons. In contrast, substituting with acceptor atoms (such as boron or gallium) results in p-type silicon, where charge transport is dominated by holes in the valence band. In the

following, N_D denotes the donor atom concentration and N_A denotes the acceptor atom concentration.

3.2.2 Carrier Transport

In a semiconductor at thermal equilibrium, there is no net movement of charge carriers except for random thermal agitation. However, this condition no longer holds when an external electric field is applied or when a non-uniform distribution of charge arises due to external perturbations.

When an electric field is applied, the charge carriers begin to move under its influence. This process is known as drift. The drift velocities of electrons and holes are given by:

$$\nu_n = -\mu_n \mathcal{E} \qquad \nu_p = \mu_p \mathcal{E} \tag{3.1}$$

where μ_n and μ_p denote the electron and hole mobilities, respectively, and $\mathcal{E}$ the electric field. At room temperature ($T = 300, \mathrm{K}$) and low doping concentrations, typical values are μ_n = 1450 $\mathrm{cm^2 V^{-1} s^{-1}}$ and μ_p = 500 $\mathrm{cm^2 V^{-1} s^{-1}}$ [59].

A second possible scenario is the presence of a non-uniform carrier distribution within the semiconductor. In this case, the system tends to restore equilibrium through carrier motion from regions of high concentration to regions of low concentration. This process is referred to as diffusion. The resulting particle fluxes are expressed as:

$$\mathbf{F}_n = -D_n \nabla n \qquad \mathbf{F}_p = -D_p \nabla p \tag{3.2}$$

where $\mathbf{F}_i$ is the carrier flux, D_i is the diffusion coefficient and ∇i represents the spatial gradient of carrier concentration.

When both drift and diffusion effects are considered, the total current density for each carrier type is given by

$$\mathbf{J}_n = q\mu_n n\mathcal{E} + qD_n\nabla n \tag{3.3}$$

$$\mathbf{J}_p = q\mu_p p\mathcal{E} - qD_p\nabla p \tag{3.4}$$

The mobility and diffusion coefficient, which are temperature-dependent (T), are related through the Einstein relations:

$$D_n = \frac{kT}{q}\mu_n \qquad D_p = \frac{kT}{q}\mu_p \tag{3.5}$$

3.2.3 Carrier Generation and Recombination

Carrier generation can occur through various processes that promote electrons into the conduction band, leading to the formation of electron-hole pairs (e-h). These processes include:

- **Thermal generation:** In this case, e-h pairs are generated due to thermal agitation. This effect introduces a noise component superimposed on the signal of interest. A common approach to mitigate this noise is to cool the sensor to a low temperature. It is important to recall that the intrinsic carrier concentration exhibits the following temperature dependence:

$$n_i \propto T^{3/2} \cdot e^{-\frac{E_g}{2kT}} \tag{3.6}$$

- **Interaction with radiation:** When radiation interacts with silicon, the incident energy can be transferred to the material, providing sufficient energy to generate e-h pairs. In silicon, approximately 3.6 eV is required to generate each pair.

If the generated carriers enter a region with a strong electric field, an **impact ionization** process may occur, leading to charge multiplication. This happens because electrons gain enough kinetic energy to create additional e-h pairs through collisions. Some devices are specifically designed to exploit

this phenomenon, using it as an intrinsic gain mechanism to enhance device sensitivity.

Once minority carriers are generated (e.g., electrons in a p-type semiconductor such as silicon), the system tends to return to thermal equilibrium. The transition from the excited state to the ground state occurs through the recombination of minority carriers with majority carriers. In silicon, this process predominantly involves crystal defects, which introduce localized energy states near the center of the bandgap. The time required for the system to return to equilibrium is referred to as the **minority carrier lifetime**, typically denoted as τ.

3.2.4 p-n junction

The structure at the core of many electronic devices—including particle detectors—is the p-n junction, which consists of the coupling between a p-type and an n-type silicon semiconductor, as shown in Fig. 3.4.

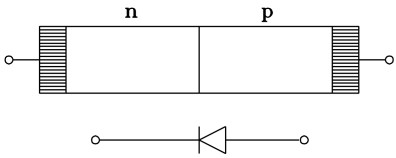

FIGURE 3.4: Graphical representation of a p-n junction [50].

Figure 3.5 illustrates what happens when two isolated silicon elements are in equilibrium until the moment they come into contact. In the latter case, free electrons from the n-type region diffuse into the p-type region, and holes from the p-type diffuse into the n-type region. This diffusion leads to the formation of fixed charges—positive in the n-type side and negative in the p-type side—resulting in a region depleted of mobile charge carriers, known as the depletion region.

This process gives rise to an electric field that opposes further diffusion.

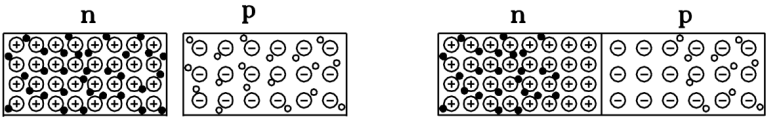

(A) PN junction without connection (B) PN junction with connection

FIGURE 3.5: Comparison between a PN junction with and without connection [50].

A qualitative representation of the charge distribution, the resulting electric field, and the corresponding potential—called the built-in potential (V_{bi})—is shown in Fig. 3.6.

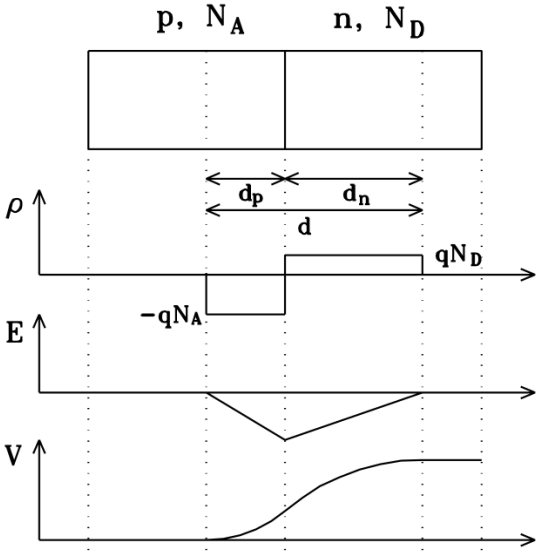

FIGURE 3.6: Graphical representation of the charge density (ρ), electric field (**E**), and potential (**V**) in a p-n junction. The depletion region (**d**) is also highlighted. [50].

Once an external potential is applied, the system obviously shifts from its state of thermal equilibrium. In the case of a semiconductor detector, the applied bias is positive on the n-type material and negative on the p-type. This increases the potential barrier at the junction, resulting in an

enlargement of the depletion region (**d**), which is defined by the following equation:

$$d = \sqrt{\frac{2\epsilon\epsilon_0 \left(N_A + N_D\right)}{qN_A N_D} \left(V_{bi} - V\right)} \tag{3.7}$$

where V_{bi} is defined by the following expression:

$$V_{bi} = \frac{kT}{q} \ln\left(\frac{N_A N_D}{n_i^2}\right) \tag{3.8}$$

The depletion region plays a crucial role in radiation detectors, as radiation passing through this region can generate electron-hole pairs. These charge carriers are separated and collected by the respective electrodes due to the electric field, producing an electrical signal that carries information about the incident radiation.

Ramo's Theorem It is important to note that the term "charge collection" is somewhat misleading. In fact, the electrical signal extracted from a sensor is not directly due to the collected charges, but rather to their motion, which induces a current on the electrodes. This induced current is described by Ramo's Theorem [60], which states that the instantaneous current $i(t)$ induced on an electrode by a charge q moving with velocity $\mathbf{v}(t)$ in a device with weighting field $\mathbf{E}_w$ is given by:

$$i(t) = -q\,\mathbf{v}(t) \cdot \mathbf{E}_w \tag{3.9}$$

The weighting field $\mathbf{E}_w$ is a hypothetical electric field defined by setting the electrode of interest to potential equal to 1, all other electrodes to zero potential, and removing all space charges from the system. It is essential to emphasize that this field does not correspond to the actual electric field within the device but is used exclusively for the calculation of the induced current.

Ramo's Theorem emphasizes that the induced current depends solely on the motion of the charge and the geometry of the electrodes (through the weighting field), and not on the actual electric field or the forces acting on the charge.

3.2.5 Charge-Sensitive Amplifier

Once the charge is generated, it must be collected and amplified to extract the relevant information. This is commonly achieved using a charge-sensitive amplifier (CSA). A simplified schematic of such a circuit is shown in Fig. 3.7.

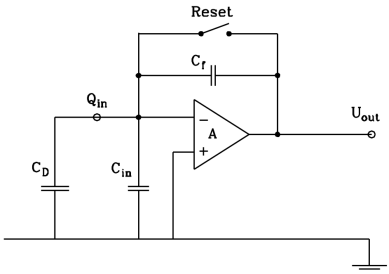

FIGURE 3.7: Simplified schematic of a charge-sensitive amplifier. The reset switch restores the system to its initial state and is often replaced by a high-value resistor [50].

This configuration enables the generation of an output voltage signal proportional to the charge collected by the sensor. In the ideal case of infinite amplifier gain A, the output voltage is given by:

$$U_{out} = -\frac{Q_{in}}{C_f + \frac{C_D + C_{in} + C_f}{A}} \overset{A \to \infty}{=} -\frac{Q_{in}}{C_f} \tag{3.10}$$

From this expression, it is evident that a low input impedance is required to ensure that the entire input charge is transferred to the feedback capacitor C_f. C_D denotes the detector capacitance, while C_{in} is the capacitance to ground of the amplifier, typically dominated by the gate capacitance of the input transistor.

The output signal from the CSA often requires further filtering and amplification before it can be processed. A common solution involves the use of an RC-CR shaper, which transforms the signal into a peaked waveform. The peak amplitude is proportional to the collected charge, facilitating easier analysis. Additionally, the shaper acts as a filter, enhancing the signal-to-noise ratio.

3.3 HYDE2 Detector Description

Building on the extensive experience gained in 3D detector fabrication and characterization for High Energy Physics applications, the University of Trento, in collaboration with FBK and TIFPA, decided to develop a device in which, starting from a planar structure and using the technology employed for 3D detectors, cavities are created and filled with an active material that enables the conversion of neutrons into charged particles, as introduced in Section 1. The HYDE2 detector is a 3D micro-structured hybrid pixel module composed of 256×256 pixels, each with a size of 55×55 μm^2. The substrate consists of p-type silicon with a nominal resistivity in the range of 10–30 kΩ·cm. On the top side, n^+ implants with metal contacts are used to connect the sensor to the readout electronics. On the backside, a p^+ layer and an aluminium layer are deposited. The term *hybrid* refers to a device in which the sensor and the electronics are manufactured separately and later connected using the bump-bonding technique. A schematic illustration of this process is shown in Fig. 3.8.

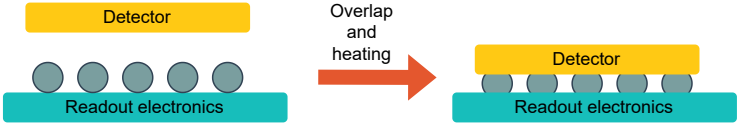

FIGURE 3.8: Simplified illustration of the bump-bonding process, where the detector is connected to the readout electronics. The gray spheres, typically made of indium, serve as interconnects. After aligning the two components, the assembly is heated, causing the spheres to melt and establishing an electrical connection between each pixel and its dedicated readout channel [50].

For the readout electronics, the well-established Medipix technology will be used. Versions 2 and 3 of Medipix are designed for 55 μm pixels, which motivated the choice of this pixel size [61].

The 3D microstructure refers to the fact that the detector is not planar but contains cavities filled with neutron-converting materials. These materials capture neutrons and emit charged particles, which then generate a signal

in the silicon. The cavities are produced using the Deep Reactive Ion Etching (DRIE) technique, which alternates a protective coating step with ion bombardment to remove material. Repetition of the process enables the fabrication of high-aspect-ratio cavities. A graphical representation of this process is shown in Fig. 3.9. This process is performed after all the standard steps for fabricating a planar device have been completed.

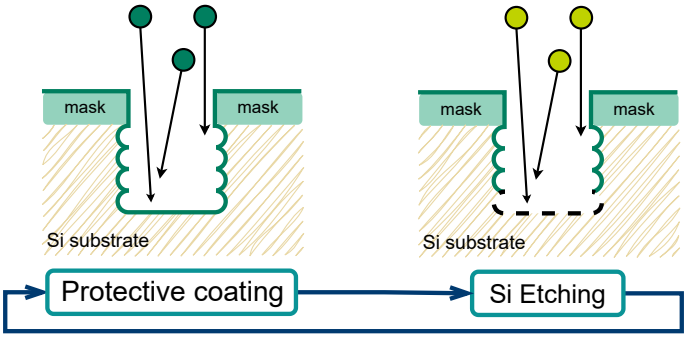

FIGURE 3.9: Graphical representation of the Deep Reactive Ion Etching (DRIE) process. In each cycle, a limited amount of material is removed; repetition of the process allows reaching the desired depth [62].

After the DRIE process, a high density of defects remains on the silicon surfaces, preventing proper device operation. For this reason, an additional step is required, consisting of cavity passivation. This process involves the deposition of an insulating material, typically SiO_2 o Al_2O_3 [63], to stabilize the surfaces. A comprehensive discussion material selection is provided in Section 3.4.

A schematic overview of the HYDE2 device is presented in Fig. 3.10.

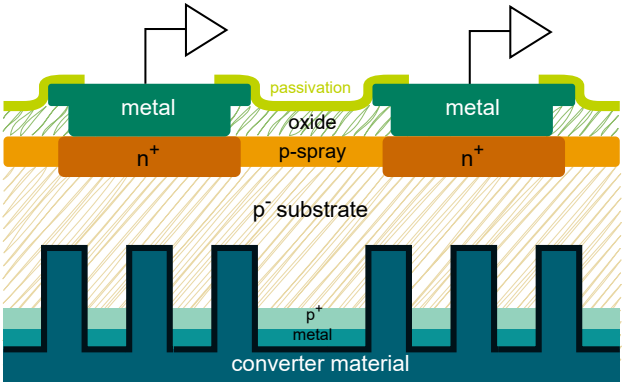

FIGURE 3.10: Graphical representation of the HYDE2 device (not to scale). The black line separating the converter material from the rest of the structure corresponds to the passivation layer deposited after the DRIE process. The back side of the sensor denotes the region containing the converter material. The reverse bias is applied through the back metallization.

3.4 Simulation results

The simulation is divided into three parts. In the first part, GEANT4 is used to conduct Monte Carlo simulations. These results represent the upper limits of the detection capture efficiency of the device, as in this case, only the energy released by the particles in the silicon is considered. The second part of the simulation is performed using Synopsys TCAD simulation. This allows the determination of the electric field maps and the weighting potential within the sensor for devices with different geometries.

These preliminary simulations can be useful as a starting point for understanding the detector efficiency by taking into account both the neutron capture efficiency and the charge collection efficiency. To obtain this information, the previously acquired preliminary data were merged using a modified version of the Allpix^2 software.

3.4.1 GEANT4 Simulation

GEANT4 is an open-source software toolkit widely used for simulating the passage of particles through matter [52]. In this case, Monte Carlo simulations are essential due to the complexity of the problem. The detector design requires consideration of both the neutron capture process within the active material and the kinematics of the reaction products, which cannot be solved analytically because of the non-trivial detector geometry.

In the present work, a thermal neutron beam with an energy of $E_n = 25$ meV is employed to evaluate the capture efficiency as a function of the geometry of the sensor and the active material. The capture efficiency (ϵ_{cap}) is defined as the number of charged particles generated in neutron capture events that release at least 50 keV of energy inside the silicon bulk. The choice of this threshold is motivated by the fact that, at this value, the signal-to-noise ratio remains acceptable.

Two possible conversion materials are considered: ^{10}B and ^{6}Li. The main characteristics of the neutron capture reactions are summarized in Table 3.1. However, lithium in its pure metallic form is highly reactive and

therefore unsuitable. A chemically stable alternative, lithium fluoride (LiF), is adopted instead [64]. In the simulations, the material densities are $\rho_{^{10}B} = 2.34\ \mathrm{g/cm^3}$ and $\rho_{^6LiF} = 2.64\ \mathrm{g/cm^3}$ [65].

Material	Reaction	Q_{value} [MeV]	σ [b]	Branching ratio
^{6}Li	^{6}Li(n,α)^{3}H	4.78	$8.7{\cdot}10^2$	100%
^{10}B	^{10}B(n,α)^{7}Li	2.79	$3.6{\cdot}10^3$	94%
	^{10}B(n,α)^{7}Li*	2.31		6%

TABLE 3.1: Q-value, cross-section (σ), and branching ratio (BR) of the two conversion materials used for thermal neutron detection [66].

For the simulations, the **QGSP_BIC_HP** PhysicsList was adopted. According to the documentation, this list is suitable for collider physics applications, and the **HP** extension is particularly accurate for neutrons, as it activates the High Precision neutron models for neutron energies below 20 MeV [67].

As a reference case, a planar configuration was simulated, consisting of a 275 μm thick silicon substrate, while the thickness of the converter material was varied. In this geometry, relatively low efficiency is expected. As illustrated in Fig. 3.11, once a neutron is captured, two charged particles are emitted. For these particles to be detected, they must reach the silicon bulk without being absorbed in the conversion layer. Since the range of an α particle in this energy range is only about 10–15 μm [68], a strong absorption effect is present.

The results are shown in Fig. 3.12. The maximum efficiency, about 4.5%, is obtained for a thickness of 20 μm using ^{6}LiF as the active material. For thicknesses below 8 μm, ^{10}B provides better efficiency. This behaviour is explained by the different ranges of the reaction products and the different capture cross-sections.

The energy spectra of the collected events (Fig. 3.13) highlight that, due to the geometry of the detector and the resulting trajectory of the reaction

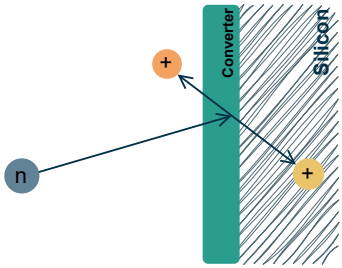

FIGURE 3.11: Schematic representation of the neutron detection process in a planar detector.

products, only one of the two charged particles can generally reach the silicon bulk. This is evidenced by the end-point of the spectrum corresponding to the more energetic reaction product, and not the sum of the two particle.

In addition, the γ-detection efficiency was estimated with GEANT4 for a 275 μm planar device, obtaining a value of 0.35% for $E_\gamma = 611$ keV. This result confirms an excellent γ rejection factor, which is essential since background gamma radiation cannot be neglected in neutron detection applications.

Building upon the planar results, a structured geometry was considered, where cylindrical cavities are etched into the silicon bulk. The adjustable parameters include the cavity radius R, the inter-cavity distance D, and the active material. The cavity depth is also relevant, with higher values generally improving efficiency. However, technological limitations restrict the maximum depth achievable with DRIE etching to about 25 μm for small R and D, as reported in [69]. This limit arises from heat dissipation and mechanical stability constraints. Therefore, the depth was fixed at 25 μm. The simulated geometry is shown in Fig. 3.14.

The first noticeable feature is the shape of the energy spectrum, as shown in figure 3.15, since in both cases the probability of detecting both charged particles is non-zero, particularly for ^{6}LiF, where the particle range is larger. Regarding the deposited energy, the difference in the mean energy is due

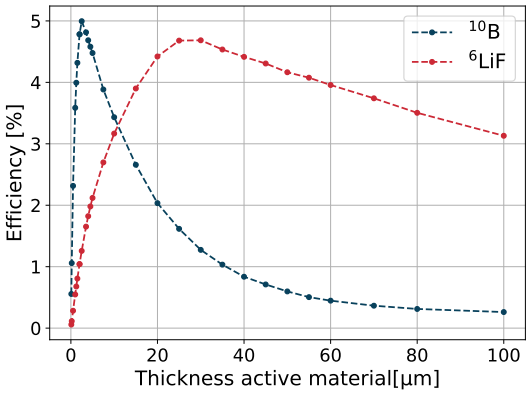

FIGURE 3.12: Detection efficiency in the planar detector case. Energy threshold: 50 keV.

to the fact that the probability that the emitted particles travel into the adjacent cavity is non-zero. As a result, the mean energy is lower, although this effect improves the overall detection efficiency.

The simulated efficiency as a function of R and D is reported in Fig. 3.16, where a threshold of 50 keV for the charge particle are used. For ^{10}B, a maximum efficiency exceeding 30% is achieved for $R \simeq 2.5$ μm, while for ^{6}LiF the peak efficiency is about 16% at larger values of R. These values represent upper limits, since charge collection effects are not included in this step of the simulation. Consequently, in a hypothetical case, it is possible that a particular geometry—although optimal from a purely neutron absorption perspective—may not allow for the collection of the charges that are generated.

For this reason, a more detailed analysis was carried out by extracting the energy deposition maps, in order to determine where the majority of the energy is effectively deposited. To further analyse the detector response, energy deposition maps were generated, providing the spatial distribution of the energy released in the active volume. A mesh with 500 nm cubic cells was implemented to record the deposited energy, using a scoring

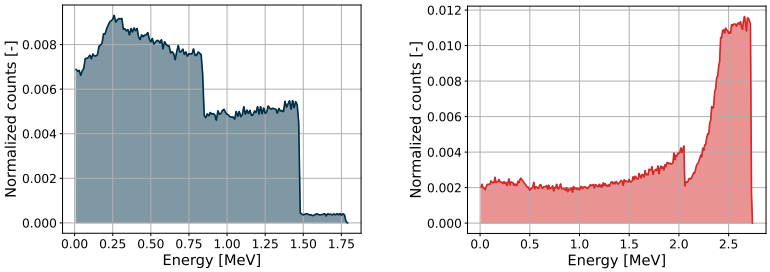

(A) ^{10}B (B) ^{6}Li

FIGURE 3.13: Energy spectra in the planar detector case for the two active materials: (a) ^{10}B and (b) ^{6}Li. Normalized to the total number of recorded events.

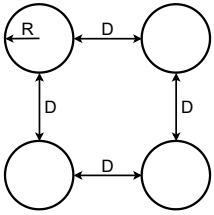

FIGURE 3.14: Configuration of etched cylindrical cavities in the silicon substrate.

mesh defined through the *boxMesh* command. This approach enables the extraction of the spatial distribution of energy deposition.

The results are presented in Fig. 3.17. In the case of ^{10}B, the energy deposition is concentrated mainly near and between the cavities, while for ^{6}LiF it is more broadly distributed, extending beyond the end of the cavities into regions that should ideally be efficiently depleted, where the charge collection efficiency (CCE) could potentially approach 100%. The collection of charges generated between cavities requires either penetration of the electric field into the inter-cavity regions or diffusion of carriers into the bulk, followed by drift toward the electrodes. The next step is to investigate the electrical properties of the device, and the corresponding results are

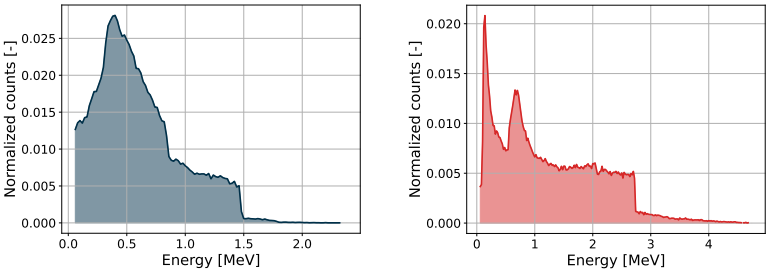

(A) ^{10}B (B) ^{6}Li

FIGURE 3.15: Energy spectra in the 3D detector case for the two active materials: (a) ^{10}B and (b) ^{6}Li. Normalized to the total number of recorded events.

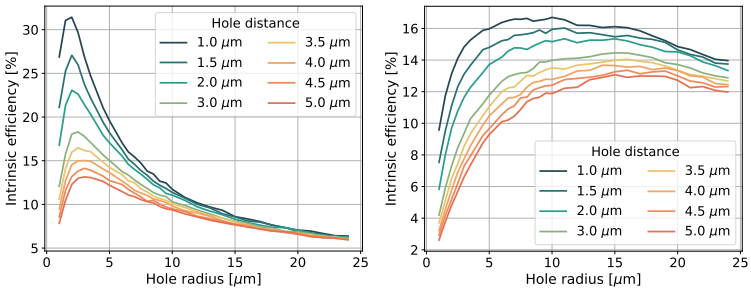

(A) ^{10}B (B) ^{6}LiF

FIGURE 3.16: Intrinsic efficiency of the HYDE2 device as a function of cavity radius R and inter-cavity distance D, for two active materials: (a) ^{10}B and (b) ^{6}LiF.

reported in the following sections.

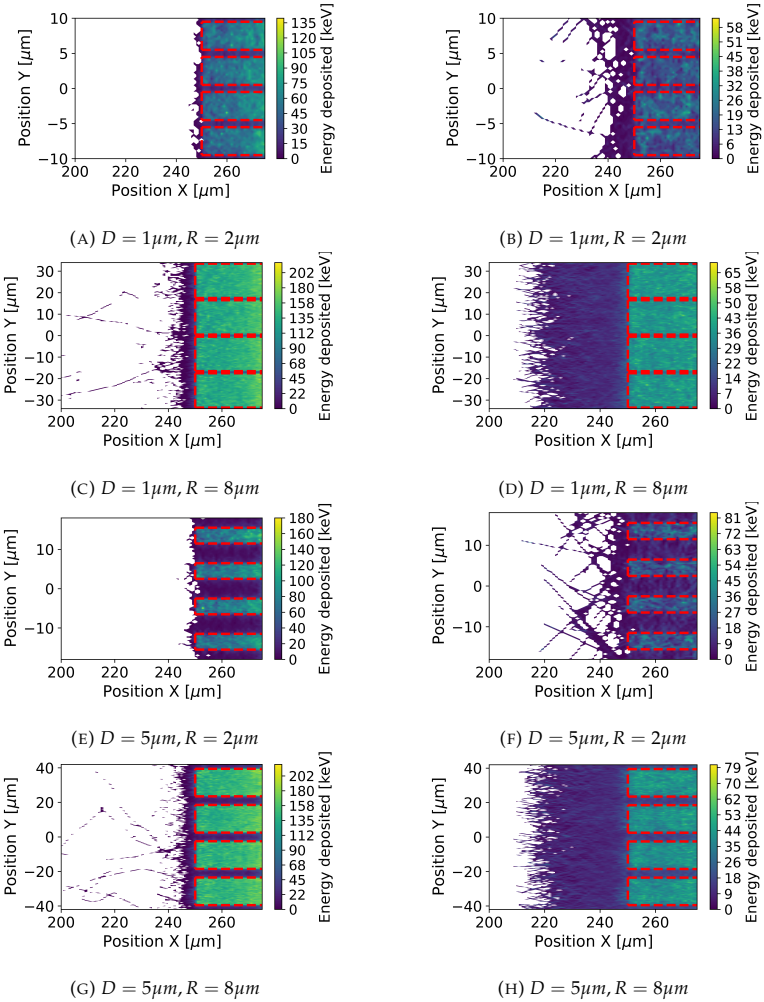

(A) $D = 1\mu m, R = 2\mu m$

(B) $D = 1\mu m, R = 2\mu m$

(C) $D = 1\mu m, R = 8\mu m$

(D) $D = 1\mu m, R = 8\mu m$

(E) $D = 5\mu m, R = 2\mu m$

(F) $D = 5\mu m, R = 2\mu m$

(G) $D = 5\mu m, R = 8\mu m$

(H) $D = 5\mu m, R = 8\mu m$

FIGURE 3.17: Energy deposition maps for different detector geometries. The first column corresponds to ^{6}LiF, while the second row corresponds to ^{10}B. The mesh size is 500×500 nm. The color scale indicates the mean energy deposited by the charged particles generated in neutron capture reactions.

3.4.2 TCAD simulation

Technology Computer-Aided Design (TCAD) refers to the use of computer simulations to develop and optimise semiconductor process technologies and devices [70].

Unlike GEANT4, which is based on the Monte Carlo approach, this study employs the Finite Element Method (FEM). In FEM, the structure under investigation is divided into a large number of small subdomains (finite elements), and the differential equations that govern the physical phenomena are solved locally for each element. The global behaviour of the system is then obtained by combining the responses of all individual elements.

One of the most important aspects of this kind of simulation is the selection of appropriate element sizes. This choice is crucial in order to obtain physically accurate results without introducing an excessive computational costs due to the number of elements. An overly fine mesh significantly increases the computational time, possibly making the simulation intractable. In the limiting case where the mesh elements are infinitesimally small, the computational time would approach infinity.

For the simulation geometry, a simplified model was used, consisting of a single pillar and two adjacent blocks acting as the substrate. While this representation is an approximation of the actual detector geometry, it allows for a considerable reduction in computational cost, which is essential due to the high number of parameters under study. A graphical representation of the simulated domain is shown in Fig. 3.18.

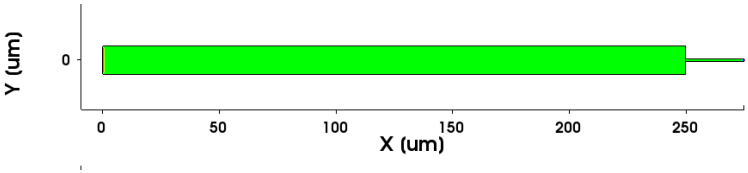

FIGURE 3.18: Simulated geometry used for the FEM analysis.

Regarding mesh sizing, a coarse grid ranging from 1 μm to 500 nm was used in the bulk region. In contrast, in the pillar region—where the geometry is

more complex and the charge deposition at the silicon–passivation layer interface is particularly relevant—a much finer mesh was necessary. In this region, the grid resolution reaches down to nanometer scale. The simulation software automatically generates an adaptive mesh, which provides a smooth transition between coarse and fine regions. Figure 3.19 shows a zoomed-in view of the geometry around $Y = 250\,\mu$m and $X = 0$, as referenced in Fig. 3.18. In this figure, the boron layer is also shown in its expected position, represented by the light-blue patterned regions located on the sides of the silicon pillar. Since, from an electrical point of view, it does not provide any contribution to the simulation, it is included here only for completeness and will not be shown in the following figures.

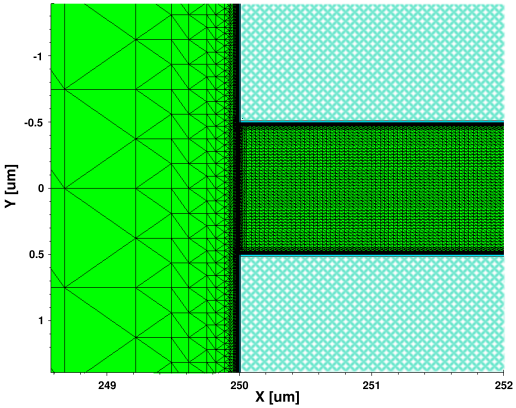

FIGURE 3.19: Zoom of the simulated mesh near $X = 0$ and $Y = 250\,\mu$m.

The substrate material used was boron-doped silicon with a concentration of 10^{12} atoms/cm^3. For the implantation step, a concentration of 10^{20} atoms/cm^3 was adopted for both n and p+ implants. Since the cavity formation through DRIE is performed after the creation of the p+ region over the entire device surface, the implantation was applied only at the pillar end and not along its entire perimeter. To simulate different types of surface passivation, an insulating layer (shown in magenta in Fig. 3.20) was introduced. Fixed charges were then deposited at the interface between

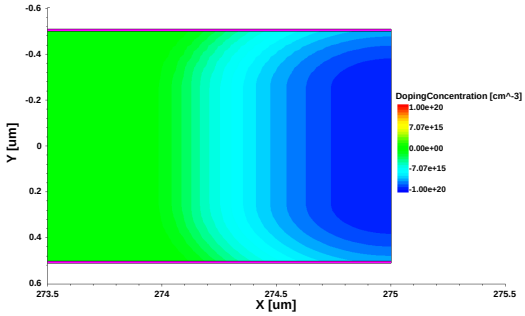

FIGURE 3.20: Enlargement of the p+ implantation and of the deposition of the passivation layer (in magenta)

the two materials in order to reproduce the charge induced by different passivation layers. In particular, the tested values were Q_{ox} = -1·10^{11} cm^{-2} for Al_2O3, Q_{ox} = +1·10^{11} cm^{-2} for SiO2 [63], and Q_{ox} = 0 for the ideal case without passivation. The latter, however, is only a theoretical scenario, since the absence of passivation leads to a non-functional device due to the damage caused by the DRIE process.

Regarding the tested geometries, the cavity radius was fixed at 2.5 μm. From an electrical perspective, the bulk plays a marginal role in these simulations, while the pillar dimension represents the most critical part of the device. In particular, pillar diameters of $D = 1, 2, 3, 4$, and 5 μm were considered, corresponding to the values used in the GEANT4 simulations.

After defining the simulation geometry and the relevant test parameters, a first simulation was performed in the quasi-stationary regime in order to extract the IV curve and the electric field map of the device. This initial simulation is of vital importance since, as previously discussed, a low current value leads to a device with an improved signal-to-noise ratio. Therefore, this step enables the identification of geometries that optimize such performance.

For the simulations, the Shockley–Read–Hall (SRH) doping-dependent

recombination model was employed, where the recombination rate is expressed as in (3.11) [71]:

$$R_{SRH} = \frac{np - n_{i,eff}^2}{\tau_p(n + n_1) + \tau_n(p + p_1)}, \tag{3.11}$$

where $n_1 = n_{i,eff} \exp\left(\frac{E_{trap}}{kT}\right)$ and $p_1 = n_{i,eff} \exp\left(-\frac{E_{trap}}{kT}\right)$, with $n_{i,eff}$ denoting the effective intrinsic carrier concentration, and τ_p and τ_n the carrier lifetimes. In our simulations, E_{trap} was set to 0, corresponding to the absence of defects in the silicon; however, this parameter may be considered in future studies. When doping dependence is included to evaluate the lifetimes, the Scharfetter relation is used, as reported in (3.12) [72], which originates from experimental observations:

$$\tau_{dop}(N_{A,0} + N_{D,0}) = \frac{\tau_{max} - \tau_{min}}{1 + \left(\frac{N_{A,0}+N_{D,0}}{N_{ref}}\right)^{\gamma}}. \tag{3.12}$$

According to [72], $N_{ref} = 10^{16}$ cm^{-3}, $\gamma = 1$, $\tau_{max} = 10^{-5}$ s for electrons and $3 \cdot 10^{-6}$ s for holes, and $\tau_{min} = 0$ s. In our simulations, all values were taken from [72], except for τ_{max}, which was set to 1 ms for both carriers, as this represents a more realistic value for detector-grade silicon [73].

The above model applies to bulk recombination. At the silicon/insulator interface, introduced by the cavity passivation layer, a modified version of (3.11) is required. In this case, the concept of surface recombination velocity (SRV) is included, a key parameter that quantifies the recombination rate of charge carriers at surfaces or interfaces [74]. The modified expression is given by (3.13):

$$R_{SRH,surf} = \frac{np - n_{i,eff}^2}{(n + n_{i,eff})/S_p + (p + n_{i,eff})/S_n}. \tag{3.13}$$

Compared to (3.11), two factors, S_p and S_n, are introduced, which account for the surface recombination velocity (SRV). Both can be evaluated using (3.14):

$$S_{p,n} = S_0 \left[1 + S_{ref} \left(\frac{N_i}{N_{ref}} \right)^{\gamma} \right]. \tag{3.14}$$

In the presence of surface defects, the SVR value tends to be relatively high, strongly affecting device performance. The simulated S_0 values were 0, 10^2, 10^3 and 10^4 cm/s, corresponding respectively to the ideal case of no recombination, a low recombination level, a moderate recombination level, and poor surface passivation [75], respectively. We use the default values $S_{\text{ref}} = 10^{-3}$ cm/s and $\gamma = 1$.

3.4.2.1 Quasi-static simulation

In the first simulation, the I-V characteristic is determined. The results are reported in Fig. 3.21, showing a strong dependence on Q_{ox}.

In the case of $Q_{ox} = 0$, which is not realistic since passivation is mandatory to mitigate the damage introduced by the DRIE process, a strong dependence on S_0 is observed. This implies that if the passivation is not uniformly deposited, regions with incomplete coverage can lead to a significant increase in leakage current. The current rise around $\sim$50 V is attributed to the complete depletion of the bulk, where the depletion region reaches the pillar.

For negative Q_{ox}, the optimal condition is obtained, as the leakage current is strongly suppressed and no dependence on S_0 is observed. In this case, the negative charge in the Al_2O_3 layer attracts positive charges from the p-type bulk to the interface, resulting in an accumulation regime. While this condition is beneficial for minimizing leakage current, it has the drawback that, for very small cavities, the accumulation layer cannot be fully depleted. Consequently, the depletion region is prevented from extending into the pillar, as illustrated in Fig. 3.22.

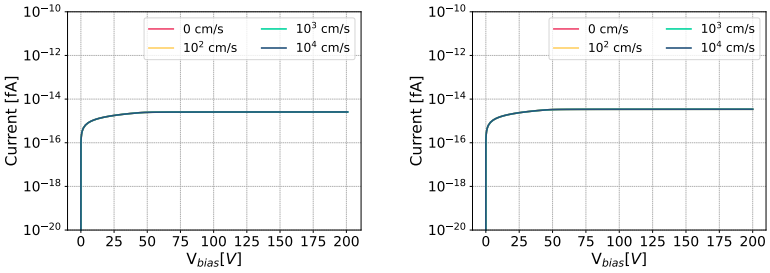

(A) $D = 1\,\mu$m, $Q_{ox} = -10^{-11}$ cm^{-2} (B) $D = 5\,\mu$m, $Q_{ox} = -10^{-11}$ cm^{-2}

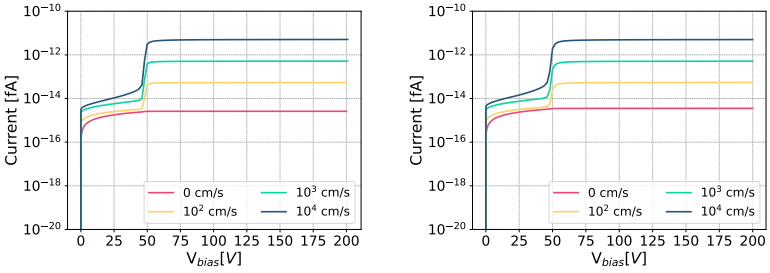

(C) $D = 1\,\mu$m, $Q_{ox} = 0$ cm^{-2} (D) $D = 5\,\mu$m, $Q_{ox} = 0$ cm^{-2}

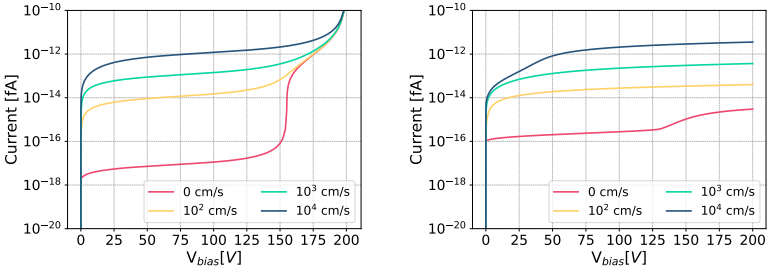

(E) $D = 1\,\mu$m, $Q_{ox} = 10^{-11}$ cm^{-2} (F) $D = 5\,\mu$m, $Q_{ox} = 10^{-11}$ cm^{-2}

FIGURE 3.21: IV curve of the detector at different S_0 values in four configurations featuring different values of Q_{ox} and D. The cavity radius hole is fixed at R=2.5μm. In Figures 3.21a and 3.21b there is no S_0 dependence so all the curves are superimposed.

In the case of positive Q_{ox}, a strong dependence on S_0 is observed. Therefore, any imperfection in the deposition process may act as a generation–recombination center, leading to an increase in leakage current. Furthermore, since SiO_2 attracts negative charges at the interface, an inversion layer may form. This inversion layer facilitates conduction by providing an additional density of minority carriers that feed the interface traps, ultimately increasing the leakage current, as shown in Fig. 3.21e and Fig. 3.21f.

Based on these results, it can be concluded that in order to limit the leakage current, Q_{ox} should be negative. This condition can be achieved by employing an Al_2O_3 passivation layer.

When analysing the electric field maps shown in Fig. 3.22a and Fig. 3.22c, it can be observed that in the case of negative Q_{ox}, the electric field remains uniform within the bulk of the sensor for both $D = 1\,\mu$m and $D = 5\,\mu$m. However, within the pillar region the electric field is negligible. This effect is more pronounced for $D = 1\,\mu$m, where the reduced dimensions combined with the negative surface charge prevent full depletion of the pillar. For $D = 5\,\mu$m, the pillar starts to deplete, as shown in Fig. 3.22c. Increasing V_{bias} does not significantly alter this behaviour.

In contrast, for positive Q_{ox}, the device is almost fully depleted, with a strong electric field inside the pillar but not in the bulk. While such a configuration may appear beneficial for charge collection, the associated high leakage current prevents the extraction of a usable signal from the detector. Therefore, the negative Q_{ox} scenario represents the most favourable solution.

For this reason, the case of negative Q_{ox} was selected for the continuation of the transient simulations.

Figure 3.23 presents a magnified view of the electric field map in the pillar region, highlighting the detailed field distribution within the pillar.

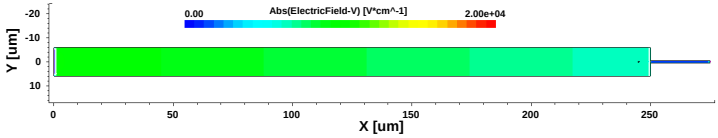

(A) D=1 μm, Q_{ox}=-1·10^{11} cm^{-2}

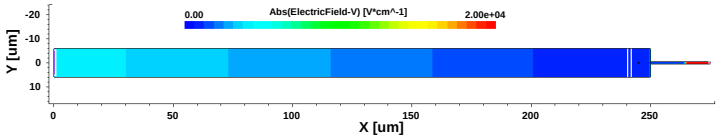

(B) D=1 μm, Q_{ox}=+1·10^{11} cm^{-2}

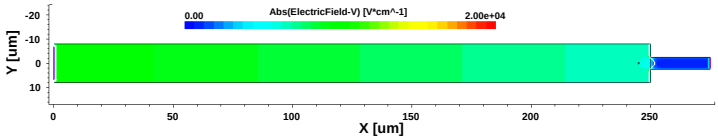

(C) D=5 μm, Q_{ox}=-1·10^{11} cm^{-2}

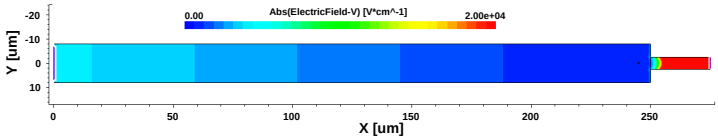

(D) D=5 μm, Q_{ox}=+1·10^{11} cm^{-2}

FIGURE 3.22: Map of the electric field inside the device as a function of D and Q_{ox}, with the white line denoting the limits of the depletion region. A V_{bias}=200V was applied.

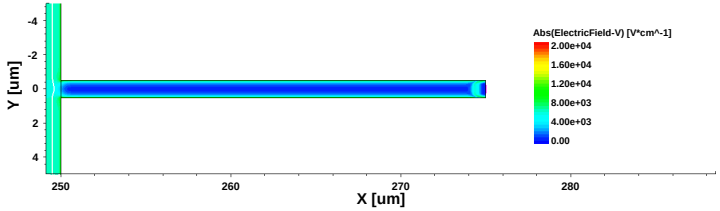

(A) D= 1μm, Q_{ox}=-1·10^{11} cm^{-2}

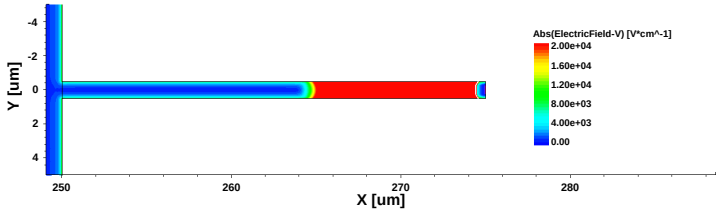

(B) D=1 μm, Q_{ox}=+1·10^{11} cm^{-2}

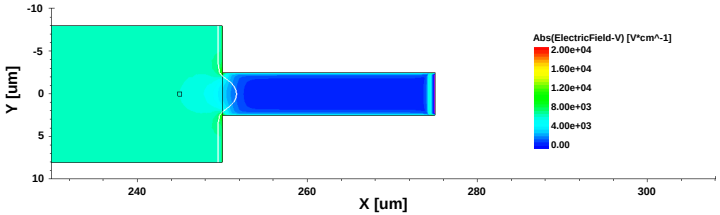

(C) D=5 μm, Q_{ox}=-1·10^{11} cm^{-2}

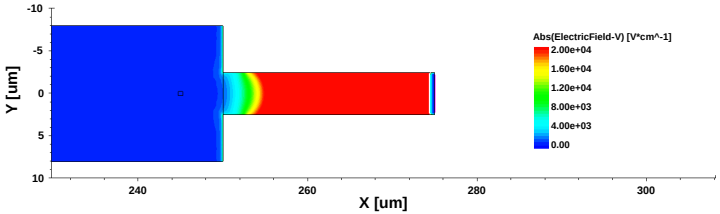

(D) D=5 μm, Q_{ox}=+1·10^{11} cm^{-2}

FIGURE 3.23: Map of the electric field inside the pillar as a function of D and Q_{ox}, with the white line denoting the limits of the depletion region, which are not visible in the case of positive Q_{ox}. A bias voltage of $V_{\text{bias}} = 200\,\text{V}$ was applied.

3.4.2.2 Transient simulation

Transient simulations are essential to study the time-dependent behavior of the device. However, this type of simulation is extremely computationally expensive; therefore, only the case with negative Q_{ox} and with D = 1 and D= 5 μm was considered. These results are used as a golden standard for the validation of the simulations performed with Allpix^2. In the case of TCAD simulations, transient analysis requires importing a previously computed static simulation at the optimal bias voltage, which allows the device to be efficiently depleted and to establish a sufficiently strong electric field; in this case, $V_{\text{bias}} = 200$ V. To evaluate the charge collection efficiency as a function of the charge deposition position, three points were selected: one inside the bulk, one at the beginning of the pillar, and one close to the p^+ implant. A graphical representation of the selected points and their positions is reported in Fig. 3.24.

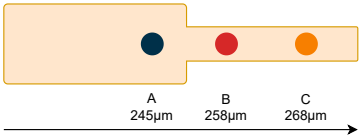

FIGURE 3.24: Positions of charge deposition selected for transient TCAD simulations.

Charge deposition was modeled using the *OpticalGeneration* module, which enables the injection of a constant number of charges within a defined region and allows for the simulation of the transient system response. For each simulation, $50{\cdot}10^3$ charges were deposited. The simulation results are reported in Fig. 3.25. As can be observed, the signal shape differs significantly depending on the deposition point. In the case of point C, where the electric field is negligible, charges first diffuse before reaching the bulk region and subsequently drifting. This leads to a longer signal with a slower rising edge. Conversely, in the case of point A, the signal exhibits a much faster rise time, since the drift process dominates. Point B represents an intermediate situation. From the intergal of the signals,

the collected charge Q_{coll} can be extracted. Dividing Q_{coll} by the injected charge Q_{in} yields the charge collection efficiency (CCE).

In Fig. 3.26, the CCE results are reported for the two cases $D = 1\,\mu$m and $D = 5\,\mu$m. As can be observed, the deeper the charge transport occurs within the pillar, the lower the CCE becomes. This behavior is due to the dominance of diffusion, which increases the probability of charge recombination and consequently reduces the CCE. For $D = 1\,\mu$m and $S_0 = 10^4$ cm/s, the CCE can decrease to approximately 50%, since surface effects become particularly significant in very small cavities. The case $S_0 = 0$ is considered as the reference standard for the simulations performed with Allpix^2, as described in Section 3.5.

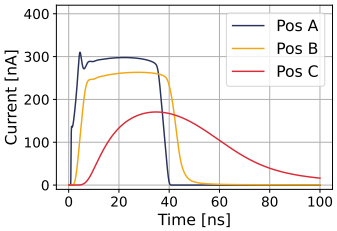

(A) D =1 μm, $S_0 = 0$ cm/s

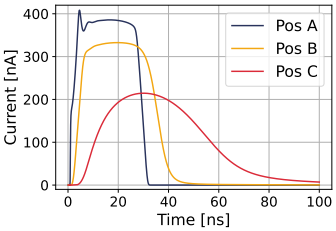

(B) D =5 μm, $S_0 = 0$ cm/s

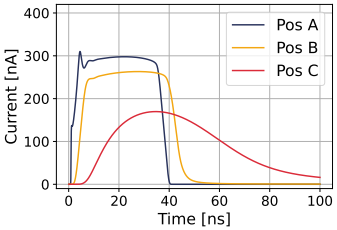

(C) D =1 μm, $S_0 = 100$ cm/s

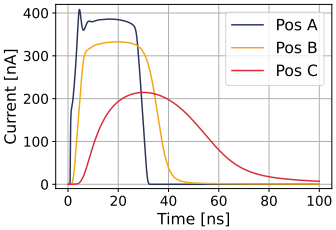

(D) D =5 μm, $S_0 = 100$ cm/s

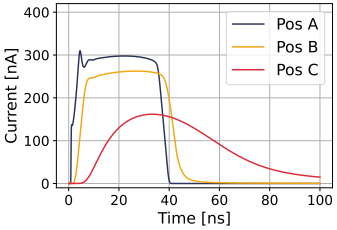

(E) D =1 μm, $S_0 = 1000$ cm/s

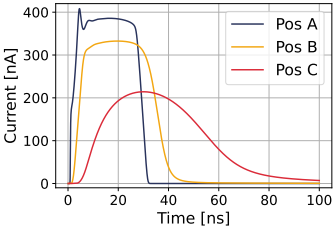

(F) D =5 μm, $S_0 = 1000$ cm/s

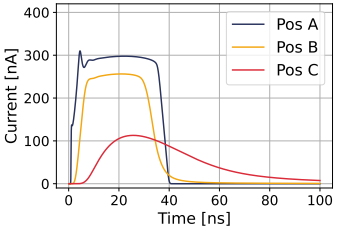

(G) D =1 μm, $S_0 = 10000$ cm/s

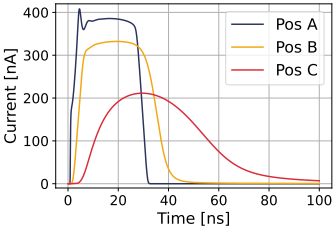

(H) D =5 μm, $S_0 = 10000$ cm/s

FIGURE 3.25: Comparison of the signals obtained from transient simulations: on the left D=1 μm, on the right D=5 μm, for different values of S_0.

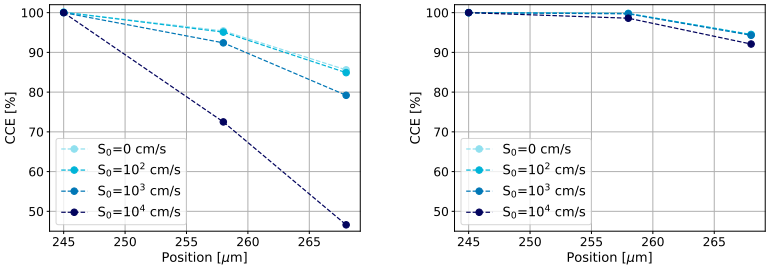

(A) D=1 μm (B) D=5 μm

FIGURE 3.26: Charge Collection Efficiency (CCE) as a function of the cavity spacing and of S_0.

3.5 Allpix^2

As described earlier, the core of this work is the development of an alternative method for the simulation of this specific detector model, where both the reaction geometry and the subsequent charge collection must be taken into account once the charged particles, generated by neutron capture, interact with the silicon detector.

The software framework chosen to address this problem is Allpix^2, which allows importing results from Geant4 and TCAD simulations. In particular, Geant4 provides the energy deposition map, thus incorporating the full reaction kinematics, while TCAD is used for two purposes: (i) extraction of the electric field and the weighting potential, since their geometry is not trivial to generate, and (ii) providing transient simulation benchmarks for validating the Allpix^2 results. This hybrid approach offers the advantage of significantly faster transient simulations, thanks to the mixed Monte Carlo and deterministic methods that reduce the computational cost [76].

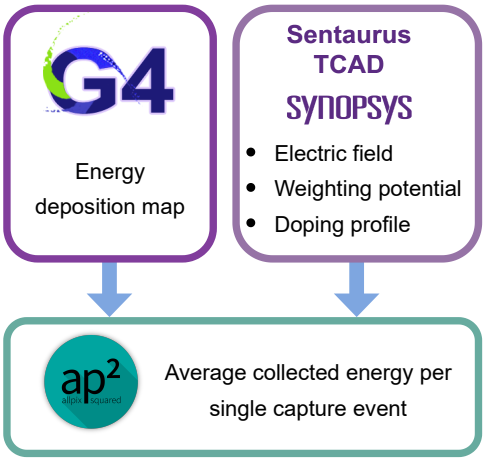

FIGURE 3.27: Workflow of the simulations combining the three different software tools.

The purpose of this approximation is to evaluate the ideal geometries for the considered class of detectors. The optimal detector geometry is determined by the selection of the active material (m), the cavity spacing (D), and the cavity radius (R), which jointly maximize both the capture efficiency (ϵ_{cap}) and the collected energy per single capture event ($\mathcal{N}$)[1]

In more formal terms, let a point $\mathbf{P} = (\epsilon_{\text{cap}}, \mathcal{N})$ be defined, whose coordinates represent a feasible combination of ϵ_{cap} and $\mathcal{N}$ resulting from a particular geometry. A geometry $\mathbf{P}^* = (\epsilon_{\text{cap}}(R^*, D^*, m^*), \mathcal{N}(R^*, D^*))$ is considered a valid solution if the corresponding point dominates[2] all other combinations, subject to the constraint that geometries yielding excessively low signals or insufficient efficiency must be excluded.

Allpix^2 does not natively support the simulation of 3D detectors of this type, where cavities are present due to material removal. While it is possible to insert 3D electrodes, these are treated as collection electrodes. In such cases, once charges reach the electrodes they are collected, and their motion terminates. In contrast, in detectors with cavities, charges that reach the cavity surfaces cannot exit. For this reason, a modification of the Allpix^2 source code was required.

In particular, the *Transient Propagation Module* was modified. This module includes the parameter $SurfaceReflectivity$, which ensures that charges are reflected back into the material when they encounter a surface. By exploiting this parameter and adapting the code, it was possible to simulate charge transport first within the pillars and subsequently within the bulk. According to the documentation, the surface reflectivity parameter (SR) can vary within the interval $[0, 1]$. Each time a particle crosses a boundary,

[1] **Definition of** $\mathcal{N}$ Let the device domain Ω be discretized into cells $i \in \Omega$, with energy deposition E_i and charge collection efficiency C_i in each cell. The average collected charge per capture event is

$$\mathcal{N} = \frac{1}{N_{\text{cap}} I_{e\text{-}h}} \sum_{i \in \Omega} E_i \, C_i \tag{3.15}$$

where $I_{e\text{-}h} = 3.6\,\text{eV}$ is the average ionization energy in silicon and N_{cap} is the number of captured neutrons.

[2] A point (x^*, y^*) from a set $S = \{(x, y) \in \mathbb{R}^2 : x \geq X_{\text{th}},\ y \geq Y_{\text{th}}\}$ is said to **dominate** another point $(x, y) \in S$ if $(x^*, y^*) \succeq (x, y)$, where $\succeq$ denotes component-wise comparison ($x^* \geq x$ and $y^* \geq y$) with at least one strict inequality ($x^* > x$ or $y^* > y$).

a random number (RN) is generated in the range $[0, 1]$. If RN>SR, the transport process is terminated.

Geometry handling only requires the addition of a few control lines in the detector configuration file, which makes the modified code relatively easy to use.

The modules used for the simulations were:

1. GeometryBuilderGeant4
2. DepositionPointCharge
3. DopingProfileReader
4. ElectricFieldReader
5. WeightingPotentialReader
6. TransientPropagation
7. PulseTransfer

The *GeometryBuilderGeant4* module was used to define the device geometry. The *DepositionPointCharge* module was employed to deposit charges within the device, similarly to the *OpticalGeneration* module used in TCAD simulations (see Section 3.4.2.2). Due to the higher computational efficiency of Allpix^2, charge deposition was performed by scanning the entire pillar length and part of the bulk across several geometries with D=1,2,3,4,5 μm.

The *DopingProfileReader*, *ElectricFieldReader*, and *WeightingPotentialReader* modules were used to import data from TCAD simulations, as the default Allpix^2 generator is not capable of handling such quantities for complex geometries. To convert **tdr** files, which contain the results of the TCAD simulations, into a format importable by Allpix^2, the provided `mesh_converter` tool was used. For the calculation of the weighting potential, the difference in electrostatic potential between the cases V_{bias}=201 V and V_{bias}=200 V was computed, as suggested in the Allpix^2 manual.

The *TransientPropagation* module enables the simulation of charge transport within the detector, with 3D handling activated. Transport consists of a combination of drift and diffusion. Drift is implemented using drift velocity, dependent on doping concentration, based on the "Masetti model." Charge transport in the electric field is solved using a fourth-order Runge-Kutta method. After each drift step, a Gaussian diffusion step is applied, with σ determined by the Einstein relation:

$$\sigma = \sqrt{\frac{2k_bT}{e}\mu t} \tag{3.16}$$

where μ is the mobility, T the temperature (fixed at 300 K), and t the time step. In the modified version of the code, charges reaching a surface are reflected back into the sensor.

At each step, the induced charge on the collection electrode is computed using the Shockley–Ramo theorem. The induced charge at step n (Q_n^{ind}) is given by:

$$Q_n^{ind} = \int_{t_0}^{t_1} I_n^{ind} = q\left(\phi(x_1) - \phi(x_0)\right) \tag{3.17}$$

where $\phi(x_j)$ denotes the weighting potential calculated at point j.

Finally, the *PulseTransfer* module was used to combine all collected charges into a single signal per pixel.

The simulation results obtained for the CCE using Allpix^2 are shown in Fig. 3.28. A good agreement between the two different approaches is observed. It should be noted, however, that Allpix^2 does not yet implement the treatment of surface velocity recombination, which—as previously discussed—can play a significant role in certain configurations. For this work, only the case $S_0 = 0$ was studied. Future developments will address the implementation of $S_0 \neq 0$.

After determining the CCE as a function of the charge-deposition position and using Eq. 3.15, we estimated the average number of charges collected in

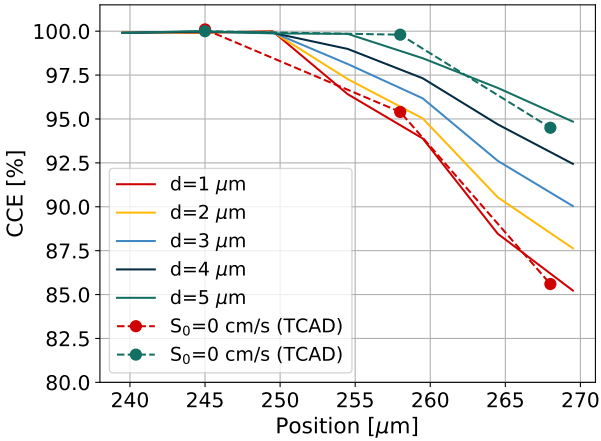

FIGURE 3.28: CCE simulation results obtained with Allpix^2, compared with TCAD results for the S_0 case. The TCAD results are considered as the reference standard.

a neutron-capture event. This quantity, together with the intrinsic detector efficiency, is one of the two parameters that must be maximized to obtain the optimal geometry. As shown in Fig. 3.29, the boron-based detector favors geometries with small cavities, whereas the lithium-based detector is dominated by configurations with larger holes. These results represent an excellent starting point for estimating the theoretical performance of the devices. They also provide, a priori, an indication of which geometries are most suitable for a given active material. The next step is undoubtedly the fabrication of such devices, ensuring that all parameters optimized in this simulation study are properly met. In Sec. 3.6, we report the first experimental results obtained from the initial test devices.

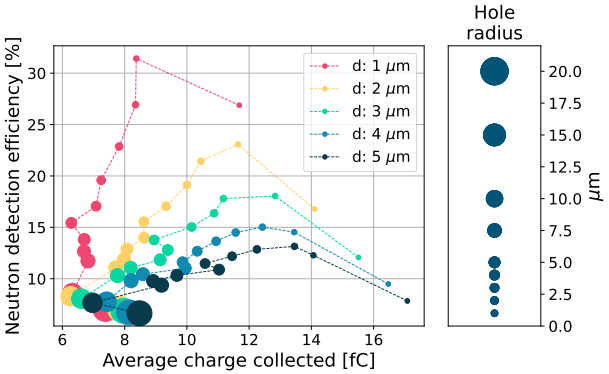

(A) ^{10}B

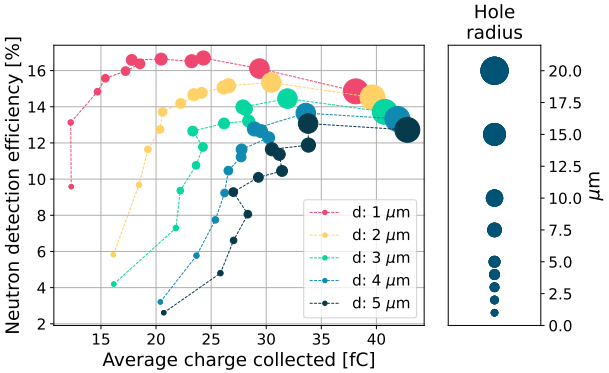

(B) ^{6}LiF

FIGURE 3.29: Graphical representation of the neutron capture efficiency versus the average number of collected charges per single capture event, for the two active materials. The optimal configurations are those that maximize both quantities simultaneously, i.e., all configurations located in the upper-right region. The marker size represents the cavity dimension under consideration.

3.6 Preliminary measurement

3.6.1 I-V curve

Within the project, several test structures were fabricated to evaluate the device performance. The first measurement performed was the current-voltage (I–V) characterization, carried out using a Keithley 4200A-SCS Parameter Analyzer. From the very beginning, several issues emerged: the devices exhibited an anomalous behavior, with a sudden increase in current around 80 V in the cavity-based structures, as shown in Fig. 3.30. This effect was not observed in the planar structure, which was specifically fabricated to assess how the presence of cavities affects the device performance.

By superimposing the simulated values (normalized by volume to account for the different dimensions), a good agreement is observed between the measurements and an intermediate simulated condition between $Q_{ox} = -1 \cdot 10^{11}$ cm^{-2} with $S_0 = 10^4$ cm/s and $Q_{ox} = -1 \cdot 10^{10}$ cm^{-2} with $S_0 = 10^3$ cm/s. This indicates that the deposition of Al_2O_3 was not performed adequately, both in terms of thickness and uniformity. It is worth noting that appreciable differences were observed among the various diodes, which share similar geometries but were located in different regions of the wafer. This inadequate passivation prevents proper device biasing, as the leakage current becomes too high, ultimately hindering the extraction of measurable signals.

Therefore, based on these results, it is important to highlight how simulations are extremely useful for accurately understanding the detector behavior and, consequently, for providing valuable insights to improve the fabrication process. We hope that the next set of samples will not suffer from the same issue, so that we can properly assess whether the final simulation results obtained with the new approach are reliable.

3.6.2 α Measurements

In addition to the leakage current characterization, measurements using an α radioactive source were performed to evaluate whether α particles could

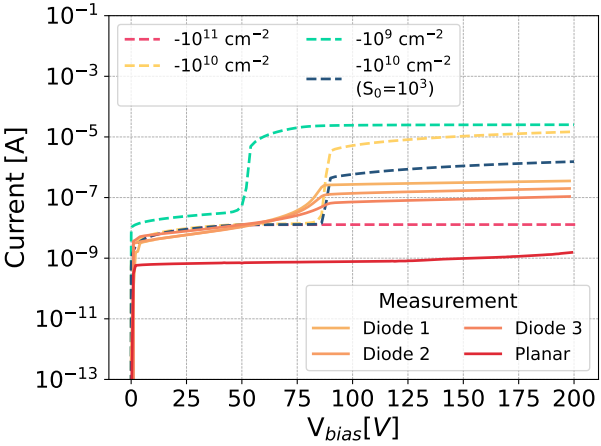

FIGURE 3.30: Comparison between measured and simulated (volume-normalized) values for the first test devices. Simulations were performed with $S_0 = 10^4$ cm/s, except for the blue dashed curve, which corresponds to $S_0 = 10^3$ cm/s. A planar structure measurement is also included to evaluate the contribution introduced by the cavities in the device.

be detected by the device.

The α detection capability of the diode was investigated using a dedicated readout chain. The diode, previously mounted on a custom electronic support board, was connected to a Cremat CR-150-R5 evaluation board hosting a Cremat CR-110-R2 charge-sensitive preamplifier. Data acquisition and power supply management were handled by a CAEN DT5780 dual digital multi-channel analyzer. The DT5780 was equipped with the DPP-PHA firmware, which implements trapezoidal signal filtering [77].

An ^{241}Am radioactive source, emitting α particles with an energy of 5.5 MeV, was used for the measurements [78]. To minimize α energy loss in air, both the diode and the evaluation board were placed inside a vacuum chamber. With this setup, it was possible to acquire both the energy spectrum (Fig. 3.31) and the corresponding voltage signals (Fig. 3.32). Measurements were performed by positioning the source alternatively on the front side

and on the back side of the diode, the latter corresponding to the drilled side.

A clear difference can be observed in both the spectral shape and the signal waveform between the two irradiation configurations. In particular, back-side exposure results in a broader energy spectrum with a peak shifted toward lower energies. This behavior can be attributed to two concurrent effects. First, when α particles impinge on the back side, they can enter the sensitive volume at different depths, ranging from regions close to the surface to regions near the bottom of the drilled cavities. Second, since the diode could not be biased at the optimal voltage due to the increase in leakage current, the charge carriers generated by the α interaction must partially move by diffusion before reaching the depleted region. This results in slower signal formation, as illustrated in Fig. 3.32, increased charge recombination, and, consequently, a larger dispersion in the measured energy spectrum.

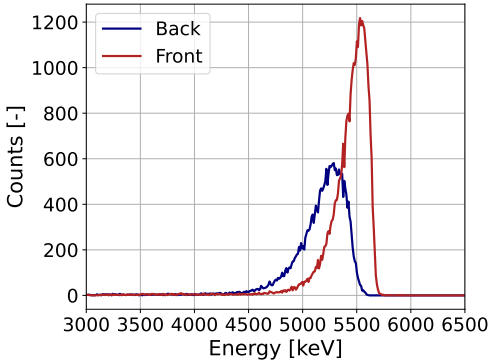

FIGURE 3.31: ^{241}Am energy spectrum acquired for front-side and back-side source exposure using a drilled diode biased at $V_{\text{bias}} = -80$ V. The signal energy is determined from charge integration. The same calibration parameters were applied for both configurations.

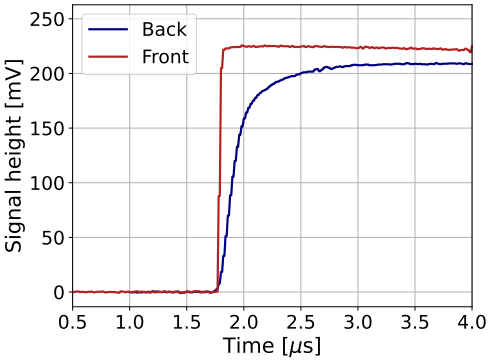

FIGURE 3.32: Voltage signals at the output of the charge-sensitive preamplifier in response to an α particle for front-side and back-side source exposure. The diode bias voltage is $V_{\text{bias}} = -80$ V.

3.7 Future Perspective

In this chapter, the system for simulating the detector for neutron imaging has been described in detail. The capabilities presented are certainly very promising. Regarding the next steps, it will be essential to improve the fabrication process, particularly the surface passivation after the DRIE process, i.e., the deposition of Al_2O_3.

Once this issue is addressed, it will be necessary to find a method to fully fill the cavities with such a high aspect ratio with the active material. Preliminary measurements presented in [51] showed a significantly lower efficiency compared to simulations, due to incomplete cavity filling. In a recent attempt using laser ablation for filling, the microscopic scans of the samples revealed insufficient results. As shown in Figure 3.33, only a thin layer ranging from $\sim$200 nm to $\sim$1 μm was deposited, demonstrating that this technique is inefficient for filling cavities of this geometry.

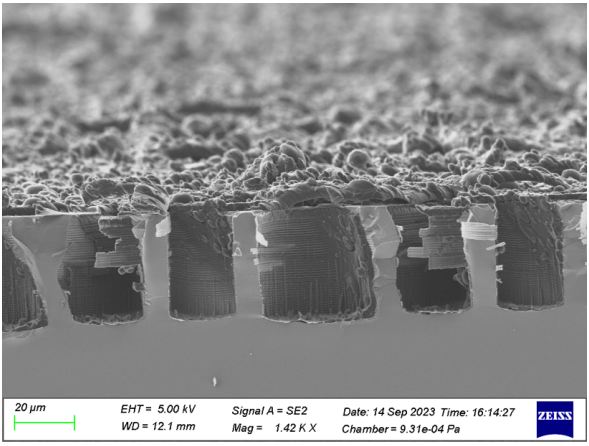

FIGURE 3.33: Test of cavity filling with boron. As can be seen, the filling is completely insufficient.

After solving these fabrication issues, neutron detection tests will be necessary. This could be performed using a ^{252}Cf source or a particle accelerator. For example, the CN facility at the INFN laboratories in Legnaro uses a

proton beam on a Be target to generate a neutron flux higher than that of a ^{252}Cf source.

Finally, another area that can be further developed is the electronics. One possibility is moving from a hybrid technology to a monolithic structure, where both the detection layer and the readout electronics are implemented on the same silicon substrate. This eliminates the need for bump bonding but introduces more complex design and technical challenges compared to developing the two parts independently. A first production test of a monolithic device has been performed, showing promising results with α source measurements [79].

Chapter 4

3D-Printed Scintillators

4.1 Introduction to Scintillator Detector

A scintillator detector is a type of radiation detector capable of interacting with ionizing radiation and, in this process, emitting light in the visible spectrum or in its vicinity. The light emission process, which arises from the de-excitation of the material, is known as fluorescence. An introduction to this mechanism is provided in Section 4.2.

An optimal scintillator material should meet several requirements:

- high efficiency in converting radiation energy into light,
- linear response over the energy range of interest,
- high transparency to ensure efficient light collection,
- suitable shaping time to maximize radiation collection,
- Refractive index of about 1.5, to optimize coupling with the readout electronics and minimize internal reflection.

Clearly, achieving all these properties simultaneously with a single material is practically impossible. Nevertheless, depending on the application requirements, it is possible to select scintillator materials that best match the desired characteristics. In general, scintillators can be divided into two main categories:

- Organic scintillators,
- Inorganic scintillators.

Since this chapter will mostly focus on organic scintillators, their detailed discussion is deferred to the following sections. For completeness, however, we briefly summarize the main features of inorganic scintillators below.

Inorganic Scintillators The scintillation mechanism in inorganic materials depends on their crystalline structure. When excited by ionizing radiation, electrons are promoted from the valence band to the conduction band. Direct radiative recombination is generally inefficient, especially for visible photon emission. To overcome this, small amounts of impurities, known as *activators*, are introduced into the crystal. These create intermediate energy levels that facilitate electron de-excitation with the emission of visible photons. A schematic representation of this mechanism is shown in Fig. 4.1.

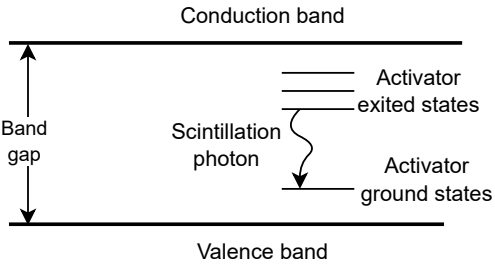

FIGURE 4.1: Simplified energy level diagram of an inorganic scintillator with activator impurities.

One of the most widely used inorganic scintillators is crystalline sodium iodide doped with thallium, NaI(Tl). In this material, the energy required to excite an electron is approximately 20 eV. Thus, a 1 MeV γ-ray interaction generates about 5×10^4 photons. From Poisson statistics, this implies a theoretical energy resolution of roughly 12%, which is significantly worse

than that achievable with semiconductor detectors. This limited resolution is a drawback, yet the possibility of producing relatively large detectors (e.g., cylindrical crystals of about 2 inches in diameter) at comparatively low cost has ensured the continued widespread use of NaI(Tl) scintillators in many applications.

4.1.1 Conversion of Light into Electrical Signal

As described earlier, scintillators are capable of emitting light when interacting with radiation. However, this light is often very weak, typically consisting of only a few thousand photons. For this reason, it is necessary to collect and amplify the signal. The main solutions are:

- Photomultiplier Tubes (PMTs)
- Silicon Photomultipliers (SiPMs)

4.1.1.1 Photomultiplier Tubes

A PMT is capable of collecting light incident on a semitransparent surface called the photocathode. When photons interact with the photocathode, electrons are emitted via the photoelectric effect. These electrons are then accelerated into an amplification stage located behind the photocathode. In this stage, a series of dynodes are present. Each time an electron strikes a dynode, it triggers the emission of several secondary electrons, producing an avalanche multiplication process. These electrons are subsequently transported to the next dynode stage. Typically, a PMT can includes from 8 to 14 dynode stages. This amplification process allows a standard PMT to reach a gain of 10^5–10^7, while maintaining an excellent signal-to-noise ratio. To achieve this, the dynodes must be properly biased at progressively higher voltages. A single bias voltage V_{bias} of the order of $\sim$1 kV is supplied, and a resistor chain distributes the potential so that each dynode is correctly polarized. The charge generated at the last dynode is collected at the anode, and this signal can then be extracted and processed by the readout electronics. [80].

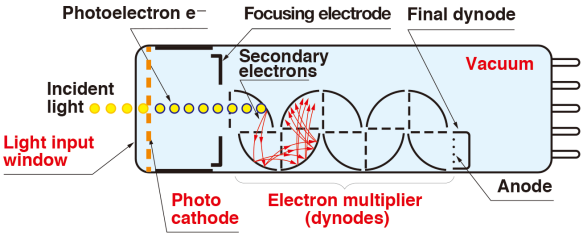

FIGURE 4.2: Schematic overview of a PMT [80]

A key parameter characterizing a PMT is the quantum efficiency (QE), defined in (4.1). Typical values are in the range of 20%–30% in the blue spectral region, since QE strongly depends on the wavelength [46].

$$\mathrm{QE} = \frac{\text{number of photoelectrons emitted}}{\text{number of incident photons}} \tag{4.1}$$

Because the amplification relies on electrons traveling between dynodes separated by several millimeters, the PMT gain drastically decreases in the presence of a magnetic field. This is due to the Lorentz force deviating the electron trajectories [81]. Furthermore, the requirement for a high V_{bias}, the sensitivity to magnetic fields, and the relatively large size of the amplification stages limit PMT applications, motivating the development of alternative technologies.

4.1.1.2 Silicon Photomultipliers

Silicon photomultipliers (SiPMs) are composed of an array of many single-photon avalanche diodes (SPADs), typically ranging from hundreds to thousands, connected in parallel to a common cathode and anode. The SiPM output signal is proportional to the number of cells triggered by incident photons. For operation, bias voltages below 100 V are sufficient, and SiPMs are insensitive to magnetic fields. They also provide high quantum efficiency, reaching values up to 40%. Optimized versions are available with enhanced sensitivity in specific wavelength regions, such as green

(RGB-SiPMs) or blue (NUV-SiPMs). Additionally, they exhibit pixelation that can be exploited for spatial reconstruction, and their small dimensions make them easier to handle [82].

4.2 Organic Scintillator

The fluorescence process in organic scintillators arises from transitions in the energy-level structure of a single molecule and therefore can be observed from a given molecular species independent of its physical state. This implies that a regular crystalline structure is not required in order to obtain scintillation. Fluorescence typically occurs in aromatic molecules. One widely encountered fluorescent substance (fluorophore) is quinine, which is present in tonic water, as shown in Fig. 4.3.

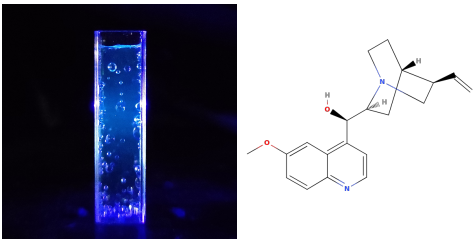

(A) (B)

FIGURE 4.3: (a) Fluorescence of tonic water under UV light. (b) Molecular structure of quinine, the molecule responsible for the fluorescence.

More specifically, the luminescence process arises from the de-excitation of an electron from an excited state to the ground state. The processes occurring between absorption and emission of light are usually represented by the Jablonski diagram, as shown in Fig. 4.4.

The singlet ground and first electronic states are denoted as S_0 and S_1. At each of these electronic energy levels, the fluorophores can exist in a number of vibrational energy levels, represented by S_{N0}, S_{N1}, and S_{N2}. Upon light absorption, the fluorophore is usually excited to some higher vibrational level of either S_1 or S_2. With few exceptions, molecules in

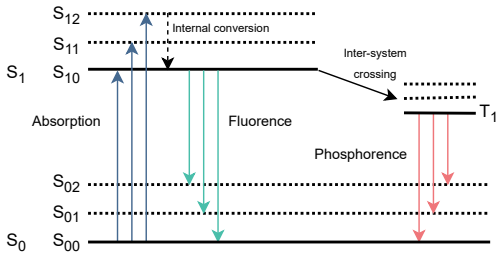

FIGURE 4.4: Fluorescence mechanism of an organic molecule with π-electron structure.

condensed phases rapidly relax to the lowest vibrational level of S_1. This process, called *internal conversion*, typically occurs within 10^{-12} s or less. Since fluorescence lifetimes are typically near 10^{-8} s, internal conversion is generally complete prior to emission. Molecules in the S_1 state can also undergo a spin conversion to the first triplet state, T_1. Emission from T_1 is termed *phosphorescence*, which is generally shifted to longer wavelengths (lower energy) relative to fluorescence. The conversion from S_1 to T_1 is called *intersystem crossing*. Transitions from T_1 to the singlet ground state are quantum-mechanically forbidden, resulting in decay times several orders of magnitude longer than fluorescence (ranging from 10^{-3} s to 1 s).

The Jablonski diagram reveals that the emission energy is typically lower than the absorption energy, an effect known as the *Stokes shift*. A common cause of the Stokes shift is the rapid relaxation to the lowest vibrational level of S_1. Moreover, fluorophores often decay to higher vibrational levels of S_0, with the excess vibrational energy dissipated through thermalization. Additional contributions to the Stokes shift may arise from solvent effects, excited-state reactions, complex formation, and/or energy transfer [83].

Another general property of fluorescence is that the same emission spectrum is generally observed regardless of the excitation wavelength. This behavior is explained by internal conversion processes: once an electron reaches a higher vibrational level, it undergoes rapid non-radiative relaxation to the lowest vibrational state, from which fluorescence emission

occurs.

In addition to luminescence, the scintillation mechanism relies on energy transfer between different fluorophores. In this process, two species must be present: a donor (D*) and an acceptor (A). The general reaction is given by

$$\text{Donor}^* + \text{Acceptor} \rightarrow \text{Donor} + \text{Acceptor}^*. \tag{4.2}$$

Two distinct types of energy transfer can occur:

- *Radiative energy transfer*, in which a photon is emitted by the donor and subsequently absorbed by the acceptor.
- *Non-radiative or resonant energy transfer*, where the transfer occurs without photon emission, typically through dipole–dipole interactions.

The most important mechanism for scintillator applications is resonant energy transfer (RET), because in the radiative method, photon transport is suppressed by the self-absorption phenomenon. This process was first described by Förster [84]. The rate of resonant energy transfer is given by

$$k_{\text{RET}} = \frac{1}{\tau_0}\left(\frac{R_0}{r}\right)^6, \tag{4.3}$$

where τ_0 is the donor fluorescence lifetime in the absence of the acceptor, r is the donor–acceptor distance, and R_0 is the Förster radius, defined as

$$R_0 = \left[\frac{3\ln(10)\,\Phi_F^0}{64\pi^5 N_A n^4}\int_0^\infty F_D(\lambda)\,\epsilon_A(\lambda)\,\lambda^4 d\lambda\right]^{\frac{1}{6}}, \tag{4.4}$$

with Φ_F^0 the donor fluorescence quantum yield in the absence of the acceptor, N_A Avogadro's number, n the refractive index of the medium, $F_D(\lambda)$ the normalized donor fluorescence spectrum, and $\epsilon_A(\lambda)$ the molar absorption coefficient of the acceptor. The Förster radius typically ranges from 1

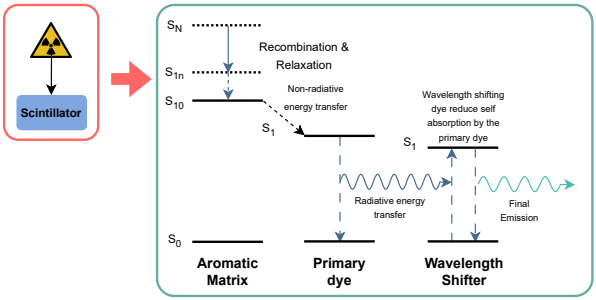

FIGURE 4.5: Scintillation mechanism of a detector under the effect of a radioactive source.

to a few nanometers and depends on the spectral overlap between donor emission and acceptor absorption.

The process of energy transfer is fundamental, since aromatic polymers typically exhibit an emission spectrum around 300 nm, where the detection efficiency is practically negligible because no photomultiplier is sensitive to this wavelength. For this reason, it is necessary to introduce a dye into the matrix, which, through energy transfer, is capable of shifting the final emission wavelength to approximately 370 nm. The addition of a further dye can shift the emission up to 420 nm. A graphical representation of the scintillation process under radiation exposure is reported in Fig. 4.5.

For the realization of efficient scintillators, it is essential to investigate the fluorescence properties of both the polymer matrix and the dissolved dyes. In particular, the energy transfer between the matrix and the primary dye, and subsequently between the primary dye and the wavelength shifter, must be optimized. Furthermore, the transparency of the scintillator to its own emission must be preserved to ensure high light collection efficiency.

Regarding the light yield, the relation between the deposited energy and the number of photons emitted per unit length is described by Birks' law [85]:

$$\frac{dL}{dx} = \frac{S\left(\frac{dE}{dx}\right)}{1 + k\left(\frac{dE}{dx}\right)} \tag{4.5}$$

where S, k, and B are constants depending on the material and on the type of radiation. The parameter k accounts for the quenching effect, which reduces the number of photons emitted for a given amount of deposited energy. This occurs, for example, with α particles, which deposit their energy in a very small volume, where the conversion into photons may become inefficient.

Before discussing innovative detector technologies, Table 4.1 summarizes the main physical and optical parameters of some commonly used commercial scintillators. As can be seen, inorganic scintillators exhibit higher light output and greater density. On the other hand, their decay time is significantly longer compared to organic scintillators.

Scintillator	Type	Density $\left[\mathrm{g/cm^3}\right]$	λ_{em} [nm]	Decay time [ns]	Light Yield [ph/MeV]
NaI(Tl)	Inorganic	3.67	415	230	38000
CsI(Tl)	Inorganic	5.51	540	1000	65000
EJ-212	Organic	0.90	423	0.9	10000
EJ-301	Organic (liquid)	0.87	425	3.2	12000

TABLE 4.1: Main characteristics of selected commercial scintillators.

4.3 Innovative 3D Scintillators

The development of scintillators is the main objective of the SHINE project, funded by INFN–CSN5. The ultimate goal is the development of ultrafast, low-cost scintillators fabricated via 3D printing using innovative materials such as perovskites and photocurable polysiloxanes. The results presented here arise from a collaboration between INFN, CNR Nanotec, CERN, and the Universities of Salento, Padova, Trento, and Bari.

The primary application of these scintillators is real-time clinical dosimetry, particularly in the context of hadron therapy, where beams of hadrons (p^+, ^{12}C ions, etc.) are employed for the treatment of specific tumor types. The main advantage of hadrons over photons lies in their distinct dose-deposition profile: whereas photon deposit energy more uniformly with depth, hadrons release most of their dose near the Bragg peak. By properly selecting the beam energy, it is therefore possible to target the tumor volume with high precision while sparing the surrounding healthy tissues [86].

The ultimate goal of this project is to enable the fabrication of 3D-printed scintillators that replicate the geometry of the anatomical region to be irradiated. Moreover, due to the flexibility of the base resin used, the scintillator can reproduce typical human body motions induced by respiration and blood circulation. This approach allows the radiation beam to be tested under near-real conditions without involving an actual patient.

The choice to include perovskites, and in particular $CsPbBr_3$, was motivated by the excellent scintillation properties that have recently emerged in the literature [33], [34], [36].

Several samples were produced using a phenyl-siloxane resin containing thiol groups (–S–H) as the base of the polymer matrix. This resin reacts with the commercial PSS100 resin, which contains C=C bonds, under UV irradiation [87]. As a reference, an alternative resin was also evaluated, namely the commercial "GENESIS Development Resin Base" (GDRB) produced by Thethon 3D.

For the $CsPbBr_3$ perovskite nanocrystals, two different synthesis techniques were explored. After synthesis, the nanocrystals were embedded within the polymer matrix. Further details on the fabrication procedure are reported in Section 4.4. Samples with different perovskite concentrations are shown in Figs. 4.6, 4.7, and 4.8.

Section 4.6 presents the results obtained during the characterization campaign, which represents the portion of the SHINE project carried out in Trento. The main objective of the characterization is to estimate the light yield (LY) of the different samples in order to identify the parameters that

should be optimized in the manufacturing process to maximize the light yield.

(A) Only matrix (B) PVK 0.05% wt (C) PVK 0.20% wt

FIGURE 4.6: Comparison of the three samples PSS–PVK–LNL

(A) Only matrix (B) PVK 0.3% wt (C) PVK 1% wt (D) PVK 3.0% wt (E) PVK 5.0% wt

FIGURE 4.7: Comparison of the three samples PSS–PVK–Ba

(A) Only matrix (B) PVK 0.3% wt (C) PVK 1% wt (D) PVK 3.0% wt (E) PVK 5.0% wt

FIGURE 4.8: Comparison of the three samples GEN–PVK–Ba

4.4 Scintillator Synthesis

The aim of this thesis is the characterization of the sensors developed within the SHINE project to maximize the light yield. Nevertheless, a concise description of the sensor synthesis process is provided here. The synthesis was carried out at the INFN Laboratories of Legnaro (LNL) and at the University of Salento.

This section describes the synthesis procedures of the three different types of samples investigated in this work, whose experimental results are presented in the following sections. Two different matrices were employed: a polysiloxane-based polymer and a commercial resin used as a reference material. Moreover, two different synthesis approaches were adopted for the perovskite (PVK) nanocrystals: the Gosh method, based on ball milling, and the ligand-assisted reprecipitation (LARP) method. The former is easier to implement, whereas the latter involves a more complex procedure; further details are provided below. The choice of employing two different synthesis routes was motivated by the aim of assessing the impact of the production method of the PVK on the scintillation efficiency. The detailed procedures are reported below.

Based on the available materials and synthesis routes, three distinct categories of samples were produced:

- **PSS-PVK-LNL**: polysiloxane-based resin with perovskites synthesized at the Legnaro laboratories;
- **PSS-PVK-Ba**: polysiloxane-based resin with perovskites synthesized at the department of Chemistry, University of Bari;
- **GEN-PVK-Ba**: commercial Genesis resin with perovskites synthesized at the department of Chemistry, University of Bari.

The acronyms listed below are used throughout this work to identify the different samples.

4.4.1 Commercial Resin

For the commercial matrix, a UV-curable acrylic resin known as *GENESIS Development Resin Base* (GDRB), produced by Thethon 3D, was employed. This resin was selected because it is suitable for the development of new UV-curable formulations for stereolithography through the inclusion of fillers. Furthermore, it does not exhibit compatibility issues when mixed with perovskite nanocrystals.

4.4.2 Synthesis of polysiloxane resin

A phenylsiloxane resin, (3-mercaptopropyl)trimethoxysilane (MPDP), providing thiol groups (−SH), reacts with the commercial PSS100 resin containing C=C bonds. Upon UV irradiation, a cross-linked polysiloxane network is formed. The resulting material exhibits high flexibility (see Fig. 4.10), a non-sticky surface, and optimal optical transparency. An additional advantage of this approach is its versatility, as all base reagents are commercially available. A schematic representation of the synthesis process is shown in Fig. 4.9. For brevity, in the following the material referred to as PSS100MPDP will be denoted simply as PSS.

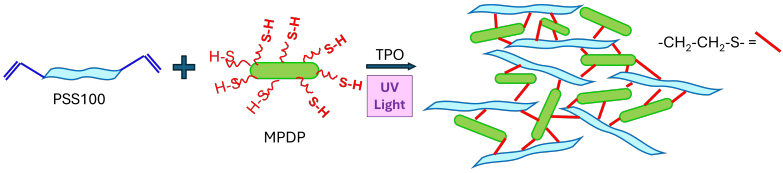

FIGURE 4.9: Schematic representation of the PSS100MPDP synthesis process.

4.4.3 Synthesis of PVK-LNL

The synthesis of PVK-LNL nanocrystals was carried out using a mechanochemical approach based on the Ghosh method [88]. Specifically, $PbBr_2$, CsBr, oleylamine, and zirconia milling spheres were directly loaded into a zirconia jar for ball milling. The presence of oleylamine is essential to ensure the stabilization and solubility of the perovskite nanoparticles

FIGURE 4.10: Flexible PSS sample obtained after UV curing.

within the polymer matrix [89]. The direct synthesis from the precursors is achieved through ball milling with zirconia spheres, leading to the formation of $CsPbBr_3$ nanocrystals. This technique uses moving spheres inside a rotating container to grind and mix powdered materials. During the milling process, the PVK deposits onto the spheres. To remove the PVK from the balls, toluene is added to dissolve the material. This solution is then mixed with the PSS before carrying out the crosslinking process. Fig. 4.11a shows the zirconia jar containing the reagents prior to the milling process, while Fig. 4.11b displays the final product under ambient light conditions. In Fig. 4.11c, the jar is illuminated with a UV lamp, qualitatively confirming the presence of perovskite nanocrystals through their characteristic green photoluminescence emission. The formation of $CsPbBr_3$ perovskite nanocrystals was further confirmed by X-ray diffraction (XRD) measurements, whose results are reported in Fig. 4.12. XRD is an analytical technique used to determine the crystal structure and phase purity of materials by measuring the diffraction patterns of X-rays interacting with the atomic planes. In perovskite research, it is commonly employed to verify the formation of the desired crystal structure and to detect possible impurities or secondary phases.

(A) (B) (C)

FIGURE 4.11: Representative images of the PVK-LNL production process: zirconia jar before ball milling (left), final product under ambient light (center), and under UV illumination highlighting green photoluminescence (right).

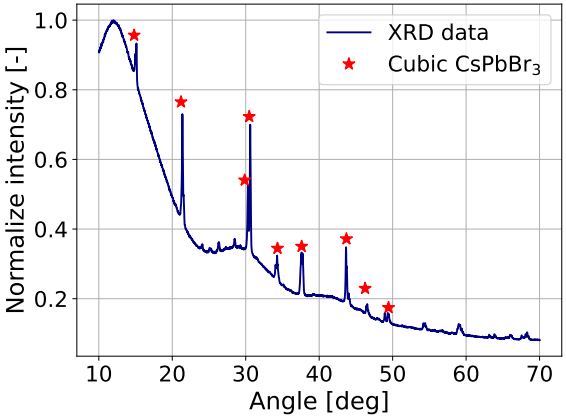

FIGURE 4.12: XRD spectrum

4.4.4 Syntesis of PVK-Ba

In the case of PVK-Ba, the PVK were synthesized at the Department of Chemistry of the University of Bari, the ligand-assisted reprecipitation (LARP) process was employed [90]. In this process, a precursor solution containing Cs-alkylcarboxylate is injected into a solution containing Pb and Br, in toluene and solvating agents, i.e. oleic acid, to allow solubilization of the precursor salt. The ligand DDAB is also added. As Cs precursor is added, perovskite nanocrystals start to grow with capping agents as protective shell and the addition of the polar aprotic solvent ethyl acetate causes the reaction to stop and the precipitation of nanocrystals. These nanocrystals, recovered in solution, are incorporated into the two resins, PSS and Genesis, before carrying out the crosslinking process. Then, successive steps of precipitation and redispersion in toluene are applied to get rid of unreacted precursors and uncapped nanocrystals. Finally, the supernatant is recovered and reused as the starting point for the next synthesis cycle. A schematic representation of the process is shown in Fig. 4.13.

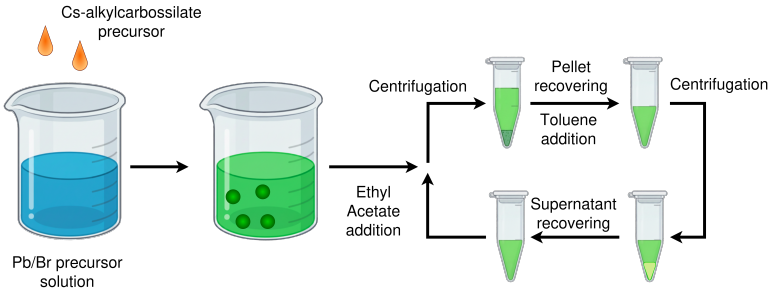

FIGURE 4.13: Representative images of the PVK-Ba production process.

4.5 Detector Energy Deposition Studies with GEANT4

As discussed in Chapter 3, the use of GEANT4 to evaluate the response of a detector to ionizing radiation is extremely useful for predicting its behavior. In the present case, however, several simplifications were required. In particular, an explicit simulation of the presence of PVK nanoclusters dispersed within the polymer matrix is computationally prohibitive. Moreover, the energy-transfer processes between the polymer matrix and the perovskite (PVK) phase are not directly implementable within the GEANT4 framework; furthermore, the very existence of an energy-transfer mechanism between the matrix and the PVK phase has not yet been experimentally demonstrated, nor is it currently established whether such a process actually occurs.

For these reasons, a set of simplified simulations was performed in order to obtain a qualitative understanding of the material response, using different particle types and energies. The goal of these simulations is to estimate the expected behavior in experimental measurements.

The first simulation considered only the polymer matrix, with the aim of evaluating the range of incident particles and ensuring that samples with sufficient thickness were available to fully stop them. Table 4.2 reports the simulated ranges for different particles and energies. As can be observed, for α particles and 3 MeV protons a sample thickness of 500 μm is sufficient to completely stop the particles and is also straightforward to fabricate. Consequently, this thickness was selected as the standard for all samples. Given this choice, and considering the organic nature of the polymer matrix, the commercial scintillator EJ-212 was selected as a reference detector (see Table 4.1 for further details). EJ-212 is commercially available in 500 μm-thick disks, allowing for direct comparisons with samples of identical thickness.

The second simulation was performed using the same polymer matrix geometry, but with the introduction of an inclined PVK layer embedded within it, as shown in Fig. 4.14. The inclined layer can be interpreted as an

Particle	Energy [MeV]	Range
α	5.5	30 μm
Proton	3.0	135 μm
Proton	30–200 MeV	14–226 mm

TABLE 4.2: Calculated range of different particles in the polymer matrix. The range of 30–200 MeV is simulated because it is used in hadron therapy)

ordered representation of PVK nanoclusters, whose total mass corresponds to the amount of PVK dissolved in the matrix for a given concentration.

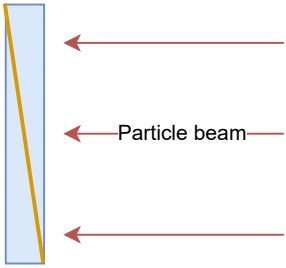

FIGURE 4.14: Schematic representation of the Geant4 geometry for γ-ray simulations. The polymer matrix is shown in blue, and the PVK layer in yellow.

This simulation allows estimating the fraction of energy directly deposited in the PVK through radiation–matter interactions, as well as the fraction deposited in the polymer matrix that could potentially be transferred to the PVK and contribute to scintillation. The results obtained by simulating a ^{241}Am source emitting 5.5 MeV α particles, and proton at 3 an 200 MeV, are reported in Table 4.3. As shown by the results, the vast majority of the deposited energy is absorbed by the polymer matrix. This behavior is mainly due to the low probability that the incident particles interact directly with the PVK nanoclusters.

In addition to charged particles, γ rays at different energies were also simulated, specifically at 10 keV, 100 keV, and 500 keV. The same geometry

Particle Energy	PVK concentration	E_{avg} PVK [MeV]	E_{avg} PSS [MeV]	E_{PVK}/E_{PSS}
α 5.5 MeV	0.5%	0.04	5.47	0.7%
	1.0%	0.08	5.46	1.4%
	2.5%	0.19	5.43	3.6%
	5.0%	0.39	5.37	7.4%
p^+ 3 MeV	0.5%	0.01	2.99	0.3%
	1.0%	0.02	2.98	0.7%
	2.5%	0.05	2.95	1.7%
	5.0%	0.09	2.93	3.0%
p^+ 30 MeV	0.5%	$4.6{\cdot}10^{-3}$	1.09	0.4%
	1.0%	$7.4{\cdot}10^{-3}$	1.09	0.7%
	2.5%	$20.0{\cdot}10^{-3}$	1.09	1.9%
	5.0%	$32.7{\cdot}10^{-3}$	1.08	3.1%
p^+ 200 MeV	0.5%	$4.9{\cdot}10^{-3}$	$259{\cdot}10^{-3}$	1.8%
	1.0%	$9.1{\cdot}10^{-3}$	$256{\cdot}10^{-3}$	3.5%
	2.5%	$17.0{\cdot}10^{-3}$	$255{\cdot}10^{-3}$	6.6%
	5.0%	$23.2{\cdot}10^{-3}$	$253{\cdot}10^{-3}$	9.1%

TABLE 4.3: Simulated average energy deposited in the PVK and in the PSS matrix for different particle types, energies, and PVK concentrations.

shown in Fig. 4.14 was used. In this case, particular attention was devoted to estimating the intrinsic detection efficiency. The results are reported in Table 4.4.

As reported in Table 4.4, the intrinsic detection efficiency (see Eq. 2.18) for 10 keV γ rays is relatively high. However, the deposited energy is very low, and the corresponding signal expected at the photomultiplier tube output is negligible, since the number of generated photons per interaction ($\sim$100 photons) is comparable to the intrinsic noise level. For 100 keV and 500 keV γ rays, the intrinsic efficiency is extremely low, at most of the order of 1%, with deposited energies of approximately 22 keV, resulting again in very weak signals. A similar conclusion applies to 500 keV γ rays, where an energy release of about 100 keV is obtained, slightly higher than

E_γ	Concentration PVK	Eff_{PVK}	Eff_{PSS}
10keV	0.5%	4%	58%
	1.0%	8%	57%
	2.5%	17%	53%
	5.0%	30%	48%
100keV	0.5%	0.10%	1.1%
	1.0%	0.19%	1.1%
	2.5%	0.43%	1.3%
	5.0%	0.85%	1.4%
500keV	0.5%	0.15%	0.60%
	1.0%	0.15%	0.61%
	2.5%	0.17%	0.61%
	5.0%	0.18%	0.63%

TABLE 4.4: Intrinsic γ-ray detection efficiency with the contributions from PVK interactions and the PSS matrix treated separately.

in the previous case; however, the corresponding efficiency is only about 0.6%. Based on these results, it is expected that real samples are essentially insensitive to γ radiation.

4.6 Characterization Results

This section presents the results of the measurements. For the PSS–PVK–LNL samples, the characterization has been completed. In contrast, for the PSS–PVK–Ba and GEN–PVK–Ba samples, proton irradiation has not yet been performed.

4.6.1 Optical measurement

4.6.1.1 Transmittance

As reported in [91], one of the fundamental properties that a scintillator must possess is transparency, since poor transparency prevents the transmission of light and therefore reduces the scintillation efficiency. To quantify the transparency of a sample, a transmittance measurement is performed. In this measurement, a light beam of known intensity strikes the sample, while a detector positioned behind it records the transmitted light.

The measurements were performed using a Double Beam UV-Visible Spectrophotometer Jasco V-570, a high-resolution UV-Visible spectrophotometer equipped with a double beam, single monochromator, variable spectral bandwidth, and a photomultiplier tube (PMT) detector. The transmittance spectra were acquired in the wavelength range $\lambda = [250, 800]$ nm.

Transmittance measurements were performed on all fabricated samples at different perovskite concentrations. The results are presented in Fig. 4.15 and Table 4.5. As expected, the incorporation of perovskite within the matrix leads to a reduction in optical transmittance as its concentration increases, due to a combination of effects including the intrinsic absorbance of the perovskite and increased light scattering arising from the inhomogeneities introduced by its presence. In particular, the behavior of samples with concentrations above 1% indicates that their transmittance becomes very low, which may exclude them as viable candidates for scintillator applications.

Another anomalous behavior is observed for the sample with 5% perovskite in the PSS–PVK–Ba matrix, which exhibits higher transmittance than the

other concentrations. For this reason, thickness measurements were performed to assess the dimensional homogeneity of the samples. These measurements (Table 4.5) revealed that this sample was significantly thinner than the others, suggesting that the observed transmittance is not representative of its intrinsic optical properties but is instead affected by fabrication issues. The thickness variability observed, particularly in the PSS–PVK–Ba samples, is attributed to the high viscosity of the material during production, which hinders the fabrication of homogeneous samples. Improving thickness uniformity is therefore essential to ensure reproducibility and to correctly evaluate and compare the transmittance of the samples.

Sample	Concentration PVK [%]	Transmittance at $\lambda = 520$nm [%]	Thickness [μm]
EJ-212	–	84.0	500±10
PSS-PVK-LNL	0.00	49.0	530±10
	0.05	27.0	490±10
	0.20	11.7	510±10
PSS-PVK-Ba	0.0	59.37	1270±10
	0.3	17.10	1470±10
	1.0	1.70	1220±10
	3.0	1.52	970±10
	5.0	0.26	300±10
GEN-PVK-Ba	0.0	39.3	1400±10
	0.3	0.17	760±10
	1.0	0.19	520±10
	3.0	0.11	450±10
	5.0	0.51	480±10

TABLE 4.5: Transmittance and measured thicknesses of the silicone-based samples. A caliper with a vernier scale having a 0.02 mm resolution was used to perform the measurements, taking care not to deform the sample under examination.

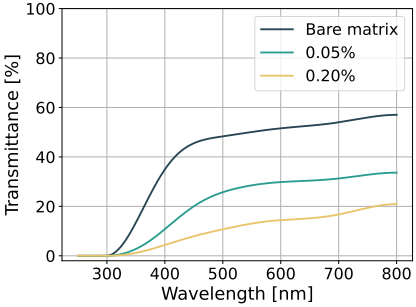

(A) PSS-PVK-LNL

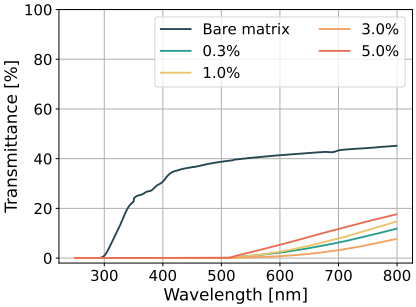

(B) PSS-PVK-Ba

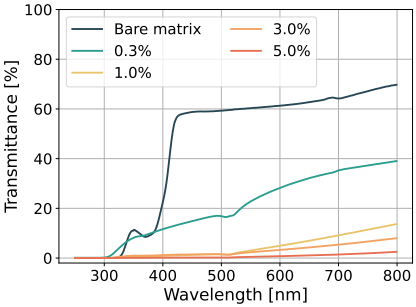

(C) GEN-PVK-Ba

FIGURE 4.15: Comparison of transmittance measurements for the two matrices at different sample.

4.6.1.2 Fluorescence

As discussed in Section 4.5, the interaction between radiation and matter leads to energy absorption by the host matrix. Through an energy-transfer process, this absorbed energy is subsequently transferred to a dye or a wavelength shifter, thereby enabling the scintillator to emit light. This mechanism can be investigated using a spectrofluorometer, as reported in [87].

To this end, a Jasco FP-6300 spectrofluorometer was employed. The samples were excited at $\lambda_{ex} = 280\,\text{nm}$, and the corresponding emission spectra were acquired. As shown in [92], an emission peak is expected at approximately $\lambda_{em} = 520\,\text{nm}$. The obtained results are presented in Fig. 4.16. In all three cases, an emission peak at 520 nm is clearly observed, whereas the emission peak of the matrix is comparatively much lower. It is important to emphasize that, based solely on these spectra, namely the comparison between the bare matrix and the matrix containing perovskite, it is not possible to conclusively assert the occurrence of a non-radiative energy transfer process between the matrix and the perovskite.

The peak intensity as a function of perovskite concentration is not reported. With the available instrumentation, the relative positioning of the sample with respect to both the excitation lamp and the detector introduces significant geometric uncertainties. As a result, quantitative comparisons are unreliable, whereas relative observations remain valid.

Once these measurements are obtained, the next step is to evaluate the scintillation light yield under excitation by a radioactive source, as described in Section 4.6.2.

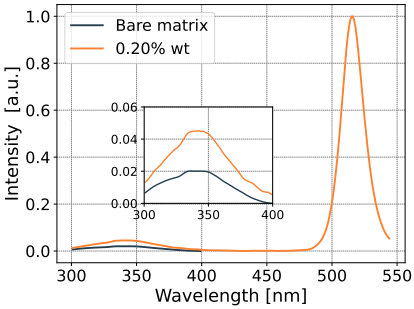

(A) PSS-PVK-LNL

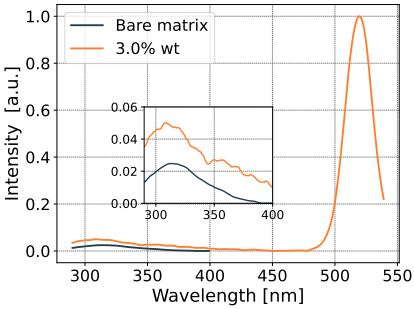

(B) PSS-PVK-Ba

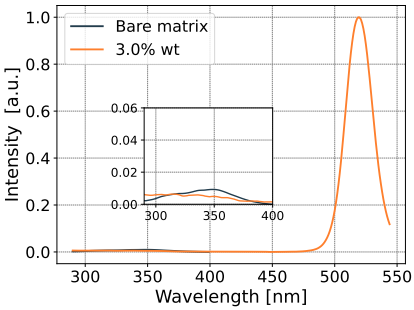

(C) GEN-PVK-Ba

FIGURE 4.16: Comparison of emission spectrum measurements for the two matrices at different sample.

4.6.1.3 Ion Beam Induced Luminescence

In addition to evaluating the emission peak of the samples under optical excitation at λ_{ex}, the emission was also investigated under proton beam irradiation. In particular, the measurement was performed at the CEDAD facility, where the Ion Beam Induced Luminescence (IBIL) spectrum was acquired using an Ocean Optics HDX spectrometer (further details on the facility are provided in Section 4.6.3).

In this measurement, the emission spectrum of the sample is acquired similarly to the optical fluorescence case; however, the excitation source, which was previously a light source, is replaced by a particle beam. This approach allows us to verify whether the scintillator emits at the same wavelength when excited by charged particles as when excited optically.

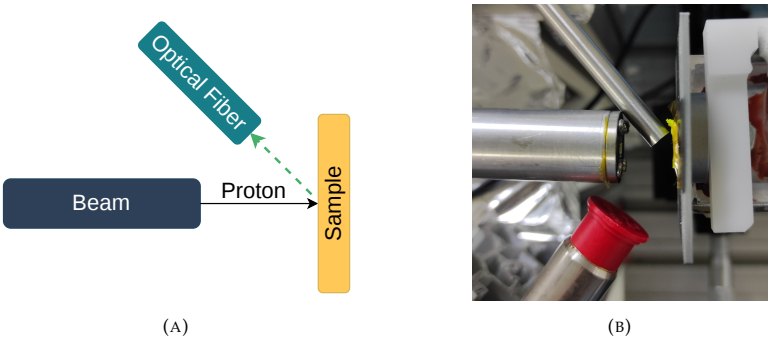

(A) (B)

FIGURE 4.17: Experimental setup for the IBIL measurement. The scintillation light is collected through an optical fiber and directed to the spectrometer.

Figure 4.18 shows the luminescence response of the PSS–PVK–LNL 0.2% sample under proton irradiation, with an emission peak at approximately 520 nm, consistent with the fluorescence measurements. This indicates that proton excitation also produces scintillation emission centered at 520 nm.

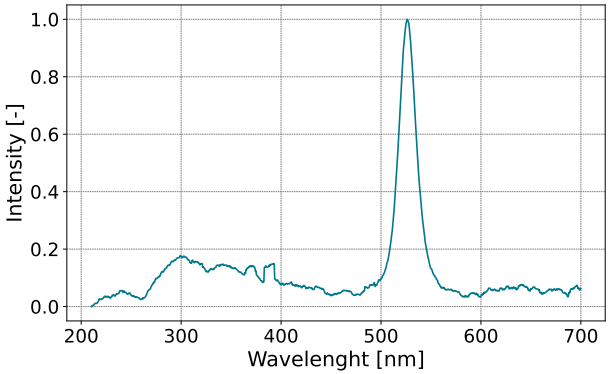

FIGURE 4.18: IBIL spectrum of the PSS–PVK–LNL with 0.2% PVK.

4.6.2 Scintillation measurements

The most straightforward method to verify the performance of a scintillator designed for particle detection consists of exposing it to a radioactive source. In this study, an ^{241}Am source was used, which emits α particles with energies of 5442.80 keV (13.1%) and 5485.56 keV (84.8%) [78]. Since it is well known that the energy resolution of organic scintillators is limited, the spectrum can be approximated by a single peak corresponding to the weighted average of the two emissions, rounded to 5.5 MeV. The activity of the source used in the measurement was 3.3 kBq.

In these measurements a two-inch Hamamatsu photomultiplier tube (PMT), model R7724-100, was used. The choice of a PMT was motivated by its well-established performance and intrinsically low noise, with respect to SiPM. The PMT was biased using an Iseg SHQ 112M high-voltage module. The bias voltage V_{bias} was selected to provide high gain while avoiding signal saturation; the same V_{bias} = -1250 V was used for all samples to allow a consistent comparison of the light yield.

Signal acquisition was performed with a CAEN DT5725 digitizer, providing a sampling frequency of 250 MS/s and a vertical resolution of 14 bits. The collected signal is an electrical signal; therefore, in principle, what is

measured is charge rather than a direct photon count. A proper calibration would thus be required to convert the signal into an absolute photon yield. However, for α-particle detectors this calibration is not straightforward due to the quenching effect. For this reason, the spectra are reported in terms of light output and expressed in arbitrary units (a.u.). Data were recorded using the ABCD (Acquisition and Broadcast of Collected Data) acquisition software [93]. A schematic representation of the setup and the interconnections between the various components is shown in Fig. 4.19.

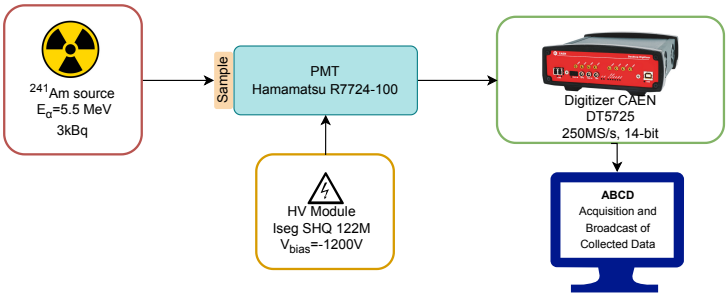

FIGURE 4.19: Experimental setup employed for the α-particle measurement with the PMT.

Scintillation measurements were performed using an alpha source collimated with a 3 mm diameter collimator. A "Background" acquisition was carried out without the source and without the sample, with only the photomultiplier tube (PMT) powered on, in order to characterize the intrinsic noise spectrum of the PMT. An additional measurement was performed with the source shielded by a sheet of paper and without a sample. In this configuration, the ^{241}Am source acts as a γ source with an energy of $E_\gamma = 59$ keV, directly irradiating the PMT. This configuration was used to verify that γ did not produce significant signals through interactions with the photocathode, which could otherwise overlap with alpha-induced events.

A further acquisition with the source ^{241}Am shielded with paper—thus emitting only 59 keV γ rays—was repeated for all samples to estimate the

light yield under γ irradiation. No signal above noise level was observed for any of the samples, as predicted in GEANT4 simulations. Since the resulting spectra were identical to the background, they were not included in the subsequent analysis.

The first measurement was performed on the EJ-212 reference sample. As shown in Fig. 4.20, a peak around channel 6100 channel was observed, corresponding to the α-particle emission peak at 5.5 MeV from ^{241}Am. The asymmetry of the peak is due to the measurement being carried out in air, which results in a reduction of the α-particle energy. In particular, particles impinging on the detector at non-perpendicular angles travel longer paths through air and therefore undergo greater energy loss. The optimal condition would be to perform the measurement under vacuum in order to avoid this effect; however, this is not feasible because operating the PMT under vacuum would cause damage to the device.

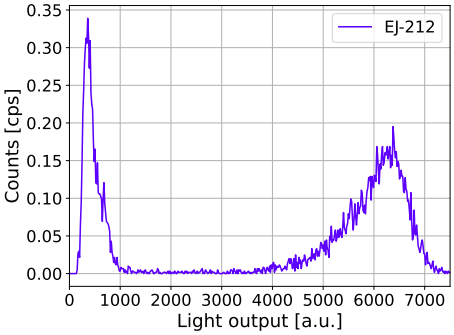

FIGURE 4.20: Energy spectrum of the EJ-212 sample.

Once the reference measurement was obtained, providing a known light output measured with our setup, measurements were performed on the PVK-based samples.

The first measurement was performed on the PSS–PVK–LNL samples. The corresponding energy spectrum, normalized to the acquisition time (T_{acq}), is shown in Fig. 4.21. To highlight the effect of the PVK, the contribution of the bare matrix was subtracted from the spectra, as shown in Fig. 4.21b.

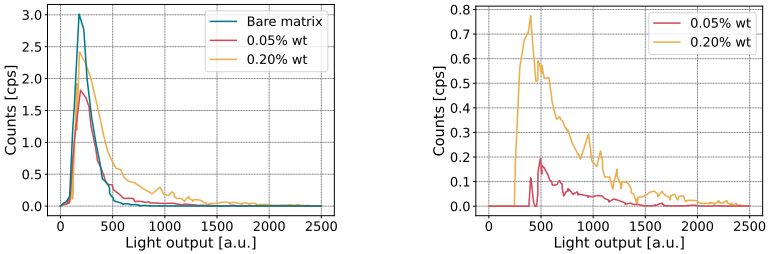

(A) All the samples

(B) Bare matrix subtracted

FIGURE 4.21: Energy spectrum of the PSS-PVK-LNL samples

As can be seen, a signal emerges above the noise level, indicating that the presence of perovskites enhances the scintillation light output and increases the number of detected events above the noise threshold.

The same approach was applied to the other available samples. The corresponding results are shown in Figs. 4.22 and 4.23 . As can be observed, in the case of the PSS–PVK–Ba samples, an increase in light output is observed with increasing PVK concentration. A less regular behavior is observed for the GEN–PVK–Ba samples; this effect is most likely due to the same issue of thickness inhomogeneity affecting the samples, as discussed previously.

Table 4.6 reports the numerical values of the average light output (LO) for the different samples. For PVK concentrations greater than 0%, the LO values reported correspond to measurements in which the contribution of the bare matrix has been subtracted.

As shown, for the all the samples, a slight increase in light output was observed as the perovskite concentration increased, consistent with the higher probability of energy transfer in samples containing more PVK.

Considering the number of observed counts, an increase in the count rate is observed with increasing PVK concentration in both the PSS–PVK–LNL and PSS–PVK–Ba samples. For the 5% PVK sample, the increase is particularly pronounced, most likely due to its reduced thickness. Since α particles have a range of approximately 30 μm, most of the scintillation occurs near the

surface; consequently, thinner samples enable more efficient light extraction due to their higher transmittance, as discussed in Section 4.6.1.1.

For the GEN–PVK–Ba samples, a less regular behavior was observed: the maximum light output occurred at a PVK concentration of 3%, corresponding to a high count rate, and then decreased for the 5% sample. This behavior can be attributed to the reduced optical transm

In conclusion, characterization with α particles indicates that the light output of the fabricated samples can reach up to 13% of LO respect to the commercial standard. Increasing the PVK concentration improves performance, but an optimal balance must be found between PVK content and sample transparency in order to maximize light output. A further improvement would be the fabrication of samples with well-controlled and comparable thicknesses, allowing a more accurate and systematic characterization and a better assessment of reproducibility. In this regard, 3D printing may help, as it provides improved control over the sample geometry.

These results can be considered as a reference point for a more systematic study of the different samples, with particular attention to the fabrication of samples with uniform thickness.

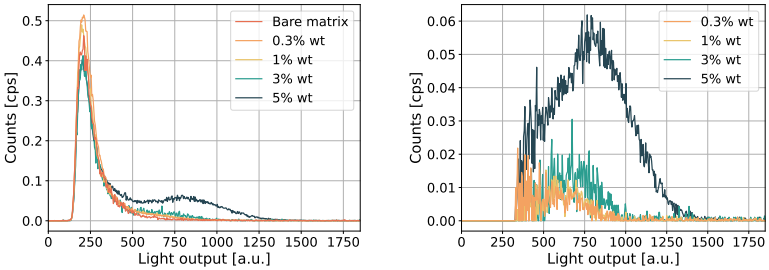

(A) No cut

(B) Bare matrix subtracted

FIGURE 4.22: Energy spectrum of the PSS–PVK–Ba sample.

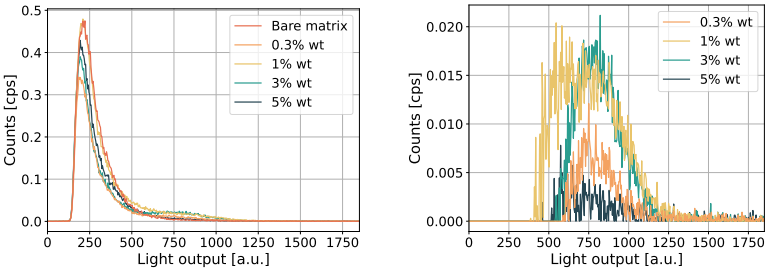

(A) No cut

(B) Bare matrix subtracted

FIGURE 4.23: Energy spectrum of the GEN–PVK–Ba sample.

Sample	PVK [%]	LO [a.u.]	$LE_{\text{Norm EJ-212}}$ [%]
EJ-212	–	$(61\pm2)\cdot10^2$	100±4
PSS-PVK-LNL	0.05 %	$(7\pm2)\cdot10^2$	11±3
	0.20 %	$(8\pm2)\cdot10^2$	13±3
PSS-PVK-Ba	0.30%	$(7\pm2)\cdot10^2$	11±3
	1.00%	$(7\pm2)\cdot10^2$	11±3
	3.00%	$(7\pm2)\cdot10^2$	11±3
	5.00%	$(8\pm2)\cdot10^2$	13±3
GEN-PVK-Ba	0.30%	$(7\pm3)\cdot10^2$	11±3
	1.00%	$(8\pm2)\cdot10^2$	13±3
	3.00%	$(8\pm2)\cdot10^2$	13±3
	5.00%	$(8\pm3)\cdot10^2$	13±3

TABLE 4.6: Absolute light output (LO) and light output relative to EJ-212 for the different samples.

4.6.2.1 Pulse Shape Discrimination (PSD)

Following the light-output characterization, additional measurements were performed to investigate pulse-shape differences between α-induced signals and background events. This study was motivated by the observation that pulses generated by α particles exhibit a noticeably longer decay time compared to PMT noise. Based on this evidence, a pulse-shape discrimination (PSD) analysis was applied.

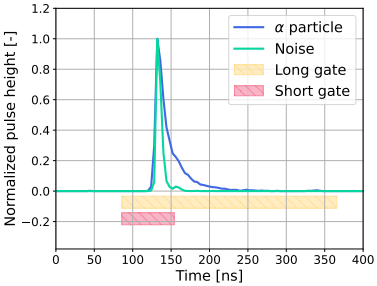

FIGURE 4.24: Signals acquired with the digitizer. The different pulse shapes produced by α particles and by noise are clearly visible.

The PSD parameter was defined as

$$\mathrm{PSD} = \frac{Q_{\mathrm{long}} - Q_{\mathrm{short}}}{Q_{\mathrm{long}}}, \tag{4.6}$$

where Q_{long} and Q_{short} are the signal integrals computed over a long and a short integration gate, respectively (see Fig. 4.24).

As shown in Fig. 4.24, α-particle signals present a significantly longer decay time than noise pulses. The extracted decay constants are $\tau_{\mathrm{noise}} = 3.71 \pm 0.08$ ns and $\tau_{\alpha} = 14.5 \pm 0.5$ ns. These values are considerably longer than the decay time reported for PVK under X-ray irradiation ($\sim$0.9 ns) in [94]. This difference may be attributed to the interaction mechanism. Indeed, considering the simulation results reported in Table 4.3, the majority of the energy deposition occurs within the polymer matrix rather than directly in the perovskite. This may suppress direct α–perovskite interactions in favour of a possible energy transfer process—although not yet demonstrated through fluorescence measurements—mediated by the polymer matrix and followed by secondary scintillation of the perovskite. This two-step mechanism results in an overall slower scintillation signal.

The two-dimensional PSD versus light-output distributions show that α-induced events populate a region clearly separated from noise. Once this behavior was identified, PSD analysis could not be repeated on the PSS–PVK–LNL samples, as they were no longer available. Consequently, the

analysis was restricted to the PSS–PVK–Ba and GEN–PVK–Ba samples.

As shown in Figs. 4.26 and 4.25, a distinct structure emerges around $Q_{\text{long}} \approx 800$, becoming more pronounced with increasing perovskite concentration. This feature is absent in samples without PVK, as illustrated in Fig. 4.27. A population of events characterized by PSD > 0.1 and $Q_{\text{long}} > 400$ was identified and isolated by applying a rectangular selection window in the PSD–Q_{long} plane.

The energy spectra reconstructed using this selection show an enhanced visibility of the scintillation signal and a clearer dependence on PVK concentration, as reported in Figs. 4.28 and 4.29. The corresponding average light-output values after PSD filtering are reported in Table 4.7. Notably, the PSD-based selection yields results comparable to those obtained via subtraction of the bare matrix contribution, with the advantage that PSD filtering can be implemented online during data acquisition.

Sample	PVK [%]	LO [a.u.]	$\text{LO}_{\textbf{Norm EJ-212}}$ [%]
EJ-212	–	$(61\pm2)\cdot10^2$	100±4
PSS-PVK-Ba	0.30%	$(7\pm2)\cdot10^2$	11±3
	1.00%	$(7\pm2)\cdot10^2$	11±3
	3.00%	$(7\pm2)\cdot10^2$	11±3
	5.00%	$(8\pm2)\cdot10^2$	13±3
GEN-PVK-Ba	0.30%	$(7\pm3)\cdot10^2$	11±3
	1.00%	$(8\pm2)\cdot10^2$	13±3
	3.00%	$(9\pm2)\cdot10^2$	14±3
	5.00%	$(7\pm2)\cdot10^2$	11±3

TABLE 4.7: Absolute light output (LE) and light output relative to EJ-212 for the different samples, based on the PSD cut.

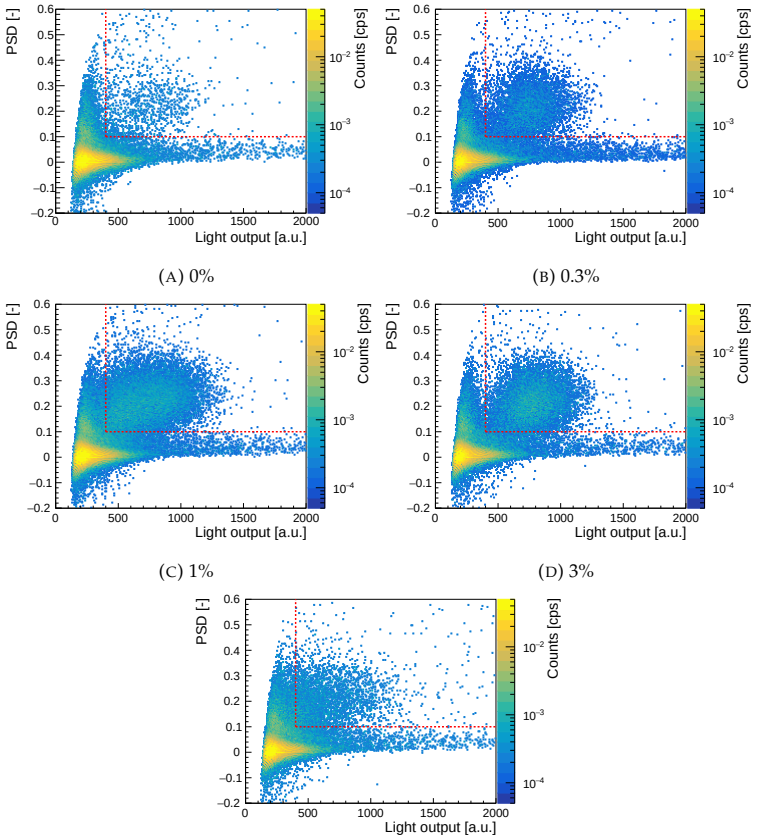

(A) 0%

(B) 0.3%

(C) 1%

(D) 3%

(E) 5%

FIGURE 4.25: Energy spectra with PSD versus light output for the PSS–PVK–Ba samples at different concentrations.

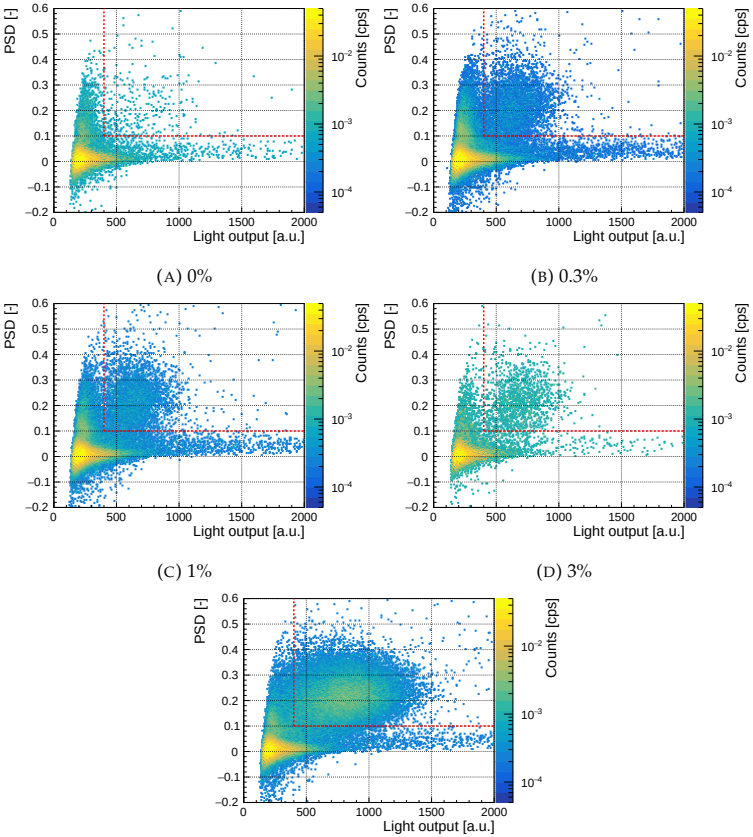

(A) 0%

(B) 0.3%

(C) 1%

(D) 3%

(E) 5%

FIGURE 4.26: Energy spectra with PSD versus light output for the PSS–PVK–Ba samples at different concentrations.

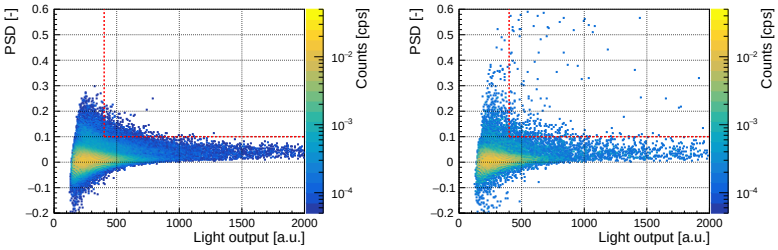

(A) Background (B) γ only PMT

FIGURE 4.27: Energy spectra with PSD versus light output for different configurations, used to validate that the events observed in the samples are not due to contamination from interactions unrelated to α-induced scintillation.

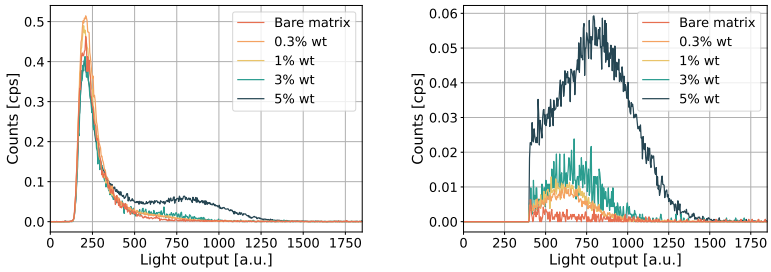

(A) No cut (B) With cut

FIGURE 4.28: Energy spectrum of the PSS–PVK–Ba sample.

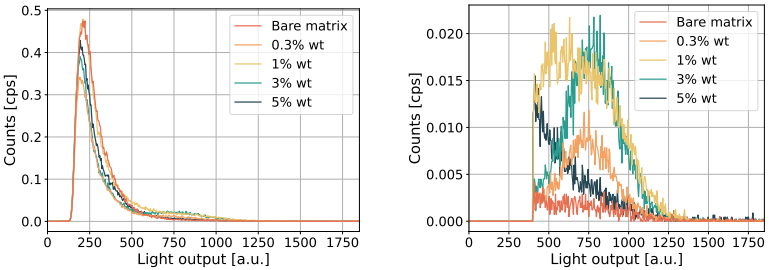

(A) No cut (B) With cut

FIGURE 4.29: Energy spectrum of the GEN–PVK–Ba sample.

4.6.3 Proton Beam Measurement

As previously described, the SHINE scintillator is designed for applications in proton therapy. For this reason, after the initial tests with the ^{241}Am source, the detector was characterized under proton beam irradiation. The measurements were carried out at the CEDAD – Center for Applied Physics, Dating, and Diagnostics at the University of Salento, where a 3 MV Tandetron accelerator is in operation. The proton beam current can be tuned in the range between 10 pA and 10 nA, with a maximum energy of 3.7 MeV. Before performing measurements on the detector samples, preliminary beam current measurements were carried out in order to evaluate the proton flux impinging on the detectors during irradiation.

4.6.3.1 Beam Current Measurement

Beam current is usually measured in vacuum using a Faraday cup (FC). However, when the proton beam is extracted in air, this type of measurement is not straightforward, since a correct determination of the external beam current is affected by ionization processes occurring along the beam path in the atmosphere. Moreover, in our case, the detector sample absorbs the entire beam, making it necessary to implement an indirect monitoring method to continuously evaluate beam stability.

In [95], a technique used at LABEC Laboratory, for the accurate estimation of the proton flux is reported. In particular, the method is based on the use of a Faraday cup and on the simultaneous measurement of the X-rays emitted by a Ni target mounted on a rotating chopper. The correlation between the Ni X-ray yield and the beam current should be established under vacuum conditions. Subsequently, the chopper is moved outside the vacuum system and positioned between the beam exit window and the sample. By measuring the X-rays emitted from the Ni target in this configuration, it is then possible to estimate the proton beam current. In the preliminary measurements at CEDAD we used a simplified approach to estimate the proton beam current using a slightly different, semi-quantitative approach, taking into account that the beam current measurement, performed without the vacuum component, is affected by a systematic error. Therefore, throughout this work, the term "estimated proton flux" will be used. A method for the direct measurement of the beam current, compatible with the experimental setup available at CEDAD, is currently under investigation.

In detail the calibration procedure consists of a simultaneous measurement of the beam current in air using a Faraday cup positioned at the same distance where the sample will later be mounted, together with the measurement of the X-ray yield induced by ionization of atmospheric argon by the proton beam (Particle Induced X-ray Emission), and not from the Ni target. This allows one to establish a relation between the current read by the FC in air and the number of X-rays produced. Once the sample is mounted, monitoring the number of X-rays produced makes it possible to estimate the current that a FC in air indicated, related to proton flux impinging on the detector. It is important to emphasize that the distances between the beam exit and the Faraday cup (or the sample, D_1) and between the interaction point and the X-ray detector (D_2) must be fixed at the beginning of the experiment and kept constant to avoid modifying the geometric efficiency of the X-ray detector (see Fig. 4.30b).

In our setup the Faraday cup consists of an aluminum cylinder with a total length of 70 mm and a graphite entrance tip of 10 mm length. The outer and inner diameters are 10 mm and 5 mm, respectively. The Faraday cup

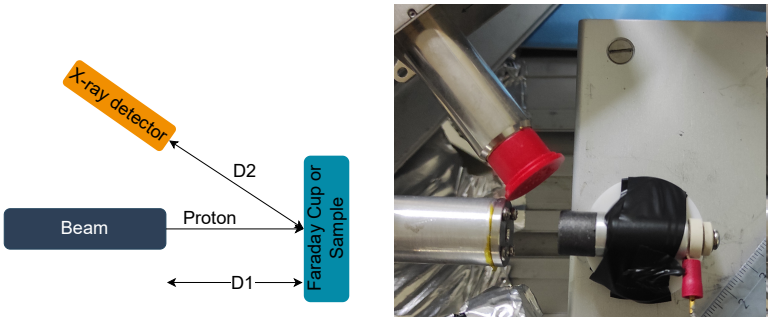

(A) (B)

FIGURE 4.30: Experimental setup for beam current measurement using a Faraday cup and X-ray monitoring.

is connected to a Keithley Series 6487 picoammeter with a resolution of 10 fA. A GPIB interface connects the picoammeter to the data acquisition computer, where a LabVIEW-based software records the instantaneous current and its integration over a set acquisition time, thus determining the impinging charge. Simultaneously with the irradiation, the X-ray spectrum is collected with an X-123SDD Silicon Drift Detector (SDD) X-ray spectrometer. Figure 4.31 shows the X-ray spectrum recorded for a current of 950 pA measured by the Faraday cup (FC). The acquisition time was $T_{\text{acq}} = 120$ s. The beam spot area was $\Sigma = 3$ mm^2. By measuring the average current with the Faraday cup (I_{meas}), the "estimated proton flux" on the detector surface Φ can be derived as follows:

$$\Phi_{ext} = \frac{dN}{d\Sigma\, dt} = \frac{I_{\text{meas}}}{e\,\Sigma} \quad \left[\frac{p^+}{\text{s} \cdot \text{cm}^2}\right], \tag{4.7}$$

where e is the elementary charge, and $I_{\text{meas}} = k\, I_{\text{true}}$. As discussed above, $k(I, E)$ is a parameter accounting for air-ionization effects and depends on both the beam current I and the beam energy E. At the present stage of our measurements, k is assumed to be constant and set equal to unity, i.e., $k = 1$. As reported in [95], this value, at a fixed energy, remains constant for beam currents above 3 nA, while it varies at lower currents. For this reason, in the

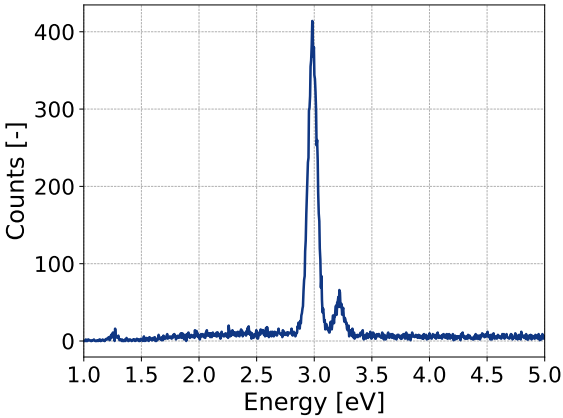

FIGURE 4.31: X-ray spectrum acquired with the SDD detector for a current of 950 pA measured by the Faraday cup (FC) and an acquisition time of 120 s.

following the comparison between the samples is performed by dividing the measurements into two classes: low-current and high-current regimes.

Several measurements were performed while varying the beam current, and the resulting correlation is shown in Fig. 4.32. The function used for the fit was $f(x) = m \cdot x$, to account for the fact that no X-rays are expected for zero beam current. The coefficient of determination ($R^2 = 0.99$) confirms the goodness of the fit and indicates that, to a first approximation, this value can be used as a conversion factor.

From the data in Fig. 4.32, a linear fit provides the relationship between the detected X-ray counts (N) and the proton flux Φ:

$$\Phi = \eta \cdot N, \tag{4.8}$$

where $\eta = (306 \pm 3) \times 10^7$ cm^{-2}s^{-1}cps^{-1}. It should be noted that this calibration factor depends on the experimental configuration: if either the detector or the sample is moved, the measurement must be repeated.

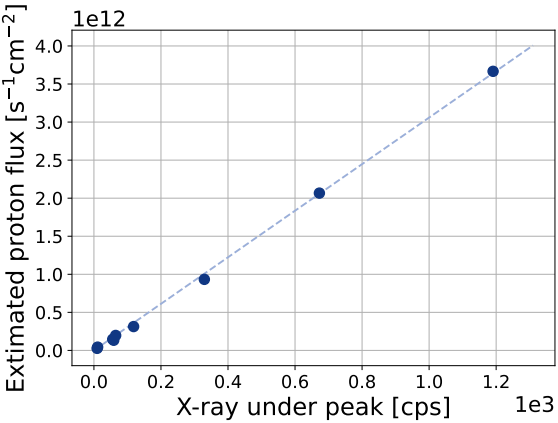

FIGURE 4.32: Correlation between proton beam current and X-ray yield induced in air.

4.6.3.2 Light yield under proton beam

After characterizing the proton beam to estimate the proton flux and testing the sensors with the α source, some of the samples were characterized under proton irradiation. For this purpose, a Newport 2832-C Dual-Channel High-Precision Optical Power Meter was used, coupled to an Optical Power Detector (spectral range 400–1100 nm). The power meter was chosen because the expected light output from a proton beam, at the typical current used at the CEDAD accelerator, is too high to be measured with a PMT, as in the case of α-particle scintillation.

In this configuration, the optical power emitted by the sample under proton irradiation was measured, since the ultimate goal is to operate these materials under proton beams. Figure 4.33 shows a photograph of the experimental setup: the sample was placed between the beam exit and the powermeter, and the measurement was therefore performed in transmission.

Figures 4.34 and 4.35 report the time evolution of the optical power measured from the various samples. The observed peaks are due to fluctuations

of the proton beam. These variations do not represent a major issue, as the beam current was determined by integrating the charge over the entire irradiation period, thereby accounting for such fluctuations. It should be noted that the flux values reported here are affected by a systematic uncertainty, as described in the previous section.

Once the time series was obtained, showing qualitatively that the light output increases with increasing beam current, the average optical power emitted by each sample was calculated as a function of the estimated proton flux. The results are reported in Table 4.8. As can be observed, the samples containing PVK exhibit a lower light output than EJ-212, while showing a higher output than the bare matrix without PVK. Regarding the analysis of the light yield as a function of the perovskite concentration, the limited number of collected data points required the measurements to be divided into two regimes, namely low-current and high-current conditions. In this way, light output values corresponding to very similar values of k can be compared. The results are shown in Fig. 4.36. As can be observed, the emitted optical power was normalized to the estimated proton flux in order to provide a semi-quantitative comparison. In the high-current regime, a clear increase in light output with increasing perovskite concentration is observed, whereas a less regular behavior is found in the low-current regime. This discrepancy may be attributed to experimental factors such as sample misalignment or local variations in sample thickness. Overall, the results appear promising; however, a larger dataset is required to draw more definitive conclusions.

FIGURE 4.33: Experimental powermeter setup.

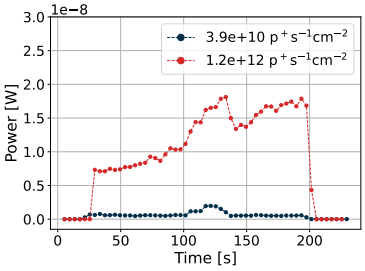

(A) 0.0%

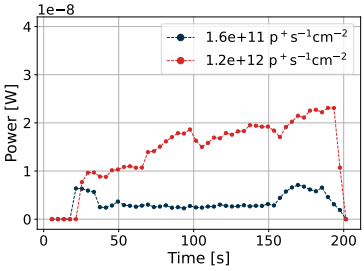

(B) 0.05%

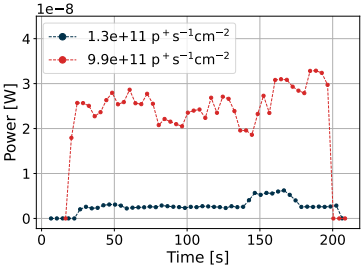

(C) 0.2%

FIGURE 4.34: Time evolution of the optical power measured for the PSS–PVK–LNL samples.

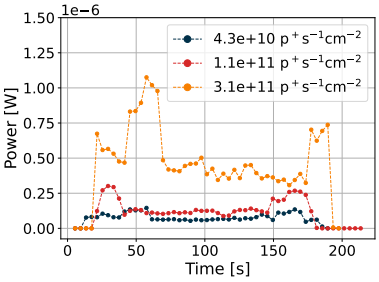

FIGURE 4.35: Time evolution of the optical power measured for the EJ-212 reference sample. The two spikes are due to beam instability.

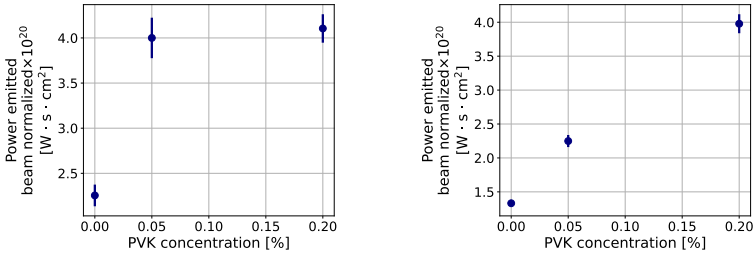

(A) Low beam current regime

(B) High beam current regime

FIGURE 4.36: Correlation between the measured optical power and the estimated PVK concentration in the (a) low and (b) high beam current regimes.

Sample	Extimated proton flux $\left[s^{-1}cm^{-2}\right]$	LO [W]
EJ-212	$(28 \pm 1)\cdot 10^{9}$	$(9.4\pm0.3)\cdot 10^{-8}$
	$(69 \pm 2)\cdot 10^{9}$	$(17.0\pm0.7)\cdot 10^{-8}$
	$(201 \pm 6)\cdot 10^{9}$	$(5.6\pm0.2)\cdot 10^{-7}$
Bare matrix	$(25\pm 1)\cdot 10^{9}$	$(5.7\pm0.2)\cdot 10^{-10}$
	$(75\pm 2)\cdot 10^{10}$	$(9.9\pm0.2)\cdot 10^{-9}$
PVK 0.05%	$(104\pm 3)\cdot 10^{9}$	$(4.2\pm0.2)\cdot 10^{-9}$
	$(76 \pm 2)\cdot 10^{10}$	$(17.0\pm0.5)\cdot 10^{-9}$
PVK 0.20%	$(82 \pm 2)\cdot 10^{9}$	$(34\pm1)\cdot 10^{-10}$
	$(63 \pm 2)\cdot 10^{10}$	$(25.3\pm0.4)\cdot 10^{-9}$

TABLE 4.8: Light output (LO), expressed in watts, measured under proton beam irradiation using a power meter.

4.7 First Printing Test

The ultimate goal of the SHINE project is the development of 3D-printable scintillation sensors based on additive manufacturing, using liquid, photocurable resin as the base material. For this reason, test samples with a gyroid geometry were fabricated at the laboratories of the University of Padova using digital light processing (DLP), as demonstrated by preliminary tests performed with an Asiga PICO 2 system (Japan) starting from the bare resin. This geometry was selected because it represents a complex structure that is particularly challenging to fabricate using 3D-printing techniques.

Photographs of the first printed samples are shown in Fig. 4.37. As can be observed, the scintillators exhibit a well-defined geometry and do not present any macroscopic structural defects. One of these samples was also tested under a proton beam to verify that the additive manufacturing process does not negatively affect the scintillation light emission.

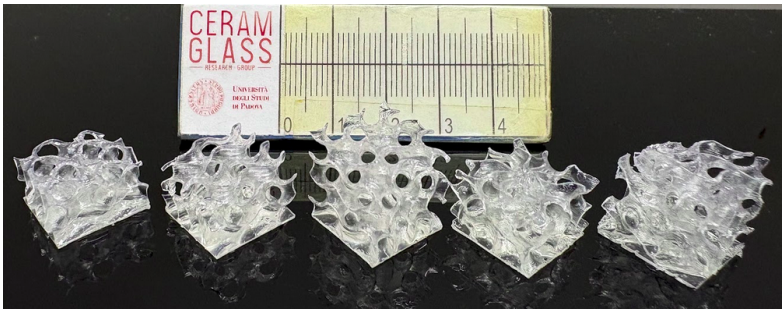

FIGURE 4.37: Examples of 3D-printed scintillators with gyroid geometry.

4.8 Future Perspectives

As extensively discussed in this chapter, this innovative class of scintillators shows promising characteristics from a scintillation performance point of view. The results obtained so far represent a solid starting point, as they indicate that achieving an optimal light yield requires a careful balance between optical transmittance and light emission efficiency.

Future work will focus on the production of a larger number of samples in order to increase the available statistics and to perform a more systematic analysis of the scintillator performance as a function of the perovskite concentration. This approach will allow the identification of the optimal configuration.

Once this optimization phase is completed, a crucial step will be the development of an efficient light-readout system tailored to these complex geometries. At present, light collection is limited to flat surfaces that can be easily coupled to a photomultiplier tube (PMT). One promising solution is the adoption of silicon photomultipliers (SiPMs), which, due to their compact dimensions, could significantly reduce the overall size of the experimental setup.

An additional upgrade consists in embedding optical fibers directly inside the scintillator volume. This solution would allow a more efficient light collection and transport toward the SiPMs, potentially leading to a further improvement in the overall detector performance.

Chapter 5

Conclusion

This PhD thesis presented two distinct yet strongly complementary research studies, both aimed at the development of next-generation radiation detectors capable of addressing the increasingly demanding requirements of modern scientific and clinical applications. In particular, the work focused on improving detection efficiency, enabling geometrical flexibility, and fostering device customization through the combined use of advanced materials, three-dimensional architectures, and multi-scale simulation methodologies.

The first part of the thesis, discussed in Chapter 3, was dedicated to the design, optimization, and performance evaluation of a novel thermal neutron imaging detector based on 3D silicon sensor technology, developed within the INFN HYDE2 project. A comprehensive multi-level simulation framework integrating GEANT4, TCAD, and ALLPIX^2 was established and validated. GEANT4 simulations demonstrated that 3D micro-structured detectors offer a substantial performance enhancement with respect to conventional planar devices, with ^{10}B-based configurations achieving neutron capture efficiencies exceeding 30%.

TCAD simulations provided detailed insight into the charge transport mechanisms, revealing that the charge collection efficiency (CCE) is critically influenced by both the cavity geometry and the quality of surface passivation. Transient analyses confirmed the strong sensitivity of the detector response to surface recombination effects and cavity dimensions. In

this context, ALLPIX^2 emerged as a powerful and computationally efficient tool capable of accurately reproducing TCAD results while enabling extensive parametric studies. The combined simulation approach allowed the definition of clear and quantitative design guidelines, representing one of the main original contributions of this thesis and laying the foundation for the experimental optimization of future devices.

The fabrication and preliminary testing of the first prototype structures highlighted several technological challenges, which were promptly identified and interpreted through the developed simulation framework. In particular, insufficient surface passivation following deep reactive ion etching (DRIE) of the cavities resulted in increased recombination losses, while difficulties in achieving uniform filling of the cavities with the active material limited the detector performance. Although these issues currently represent the main limiting factors, the overall device concept has proven to be highly promising. Once these technological aspects are addressed, the proposed detector architecture is expected to be fully validated in the target operational environment for thermal neutron imaging.

The second part of this thesis, discussed in Chapter 4, focused on the development and characterization of innovative, fast, and cost-effective scintillators fabricated via 3D printing, employing novel materials such as perovskites embedded in photocurable polysiloxanes. This activity was carried out within the SHINE project, funded by INFN–CSN5. A systematic optical characterization, including transmittance and fluorescence measurements, enabled the identification of material compositions most suitable for scintillation applications. Fluorescence measurements confirmed the characteristic emission of the perovskite at approximately 520 nm; however, they did not provide conclusive evidence for the occurrence of non-radiative energy transfer between the polymer matrix and the perovskite. Transmittance measurements highlighted a reduction in optical transparency with increasing perovskite concentration, attributable to a combined effect of intrinsic perovskite absorbance and enhanced light scattering caused by matrix inhomogeneities. This effect therefore sets an upper limit on the maximum usable perovskite concentration, beyond which the device

would become effectively opaque.

In addition to optical measurements, radiation tests were performed using α particles and proton beams, providing a realistic assessment of the scintillation performance. The results are particularly encouraging, as light yields on the order of 10% relative to a commercial reference scintillator were achieved for perovskite concentrations between 3% and 5% under α-particle irradiation. Moreover, α-particle measurements revealed the generation of slower scintillation signals compared to those observed in standalone perovskite samples, demonstrating the potential to explore pulse shape discrimination (PSD) techniques with this class of scintillators. Proton irradiation tests, although limited to a subset of samples, represent a solid starting point for future investigations.

These findings constitute a significant step forward in the development of 3D-printable scintillators and represent a solid starting point for future systematic studies aimed at optimizing dopant concentration, light yield, timing properties, and radiation hardness. Moreover, the successful demonstration of 3D printing confirmed the strong potential of additive manufacturing for the realization of complex, customizable detector geometries.

Overall, this thesis demonstrates that the integration of advanced materials, three-dimensional detector architectures, additive manufacturing techniques, and multi-scale simulation approaches represents a powerful and versatile strategy for the development of high-performance radiation detectors. While several technological challenges remain to be addressed, the results obtained provide clear directions for future research and underline the significant potential impact of the proposed solutions. The methodologies and design principles developed in this work are expected to be applicable to a broad range of radiation detection systems, spanning applications from fundamental research to medical diagnostics and radiotherapy, thus contributing to the advancement of the state of the art in radiation detector technology.

Acknowledgements

I would like to express my sincere gratitude to my supervisors, Prof. Alberto Quaranta and Prof. Gian-Franco Dalla Betta, for their constant guidance, patience, and invaluable support. Their expertise and encouragement have been fundamental in shaping the direction and quality of this thesis; I am truly honored to have worked under their mentorship.

Special thanks go to Prof. Lucio Pancheri for his generous advice and insights, which provided essential perspective throughout the project.

I am deeply grateful to my family for their unwavering support and understanding over the years. Their belief in my potential has been a constant source of motivation. To the OpenSpace, the RoboGang, and all my friends—especially Giulia—for the good times and the constant support.

Finally, I want to thank three people who were instrumental in my decision to pursue this PhD and who taught me so much along the way. My heartfelt thanks to Prof. Sandra Moretto, Dr. Sara Maria Carturan, and Dr. Eduardo Felix Pino Andrades for their mentorship and support. I look forward to our future collaborations.

Bibliography

[1] R. T. Kouzes, A. T. Lintereur, and E. R. Siciliano, "Progress in alternative neutron detection to address the helium-3 shortage," *Nuclear Instruments and Methods in Physics Research Section A: Accelerators, Spectrometers, Detectors and Associated Equipment*, vol. 784, pp. 172–175, 2015.

[2] M. Henske, M. Klein, M. Köhli, *et al.*, "The 10B based jalousie neutron detector–an alternative for 3he filled position sensitive counter tubes," *Nuclear Instruments and Methods in Physics Research Section A: Accelerators, Spectrometers, Detectors and Associated Equipment*, vol. 686, pp. 151–155, 2012.

[3] F Pino, C. Fontana, J Delgado, *et al.*, "Characterization of a medium-sized cllb scintillator: Single neutron/gamma detector for radiation monitoring," *Journal of Instrumentation*, vol. 16, no. 11, P11034, 2021.

[4] J. C. Delgado, C. Provenzano, M. Marra, *et al.*, "Study of a metal-halide perovskite cspbbr3 thin film deposited on a 10b layer for neutron detection," *Journal of Physics D: Applied Physics*, vol. 57, no. 5, p. 055 501, 2023.

[5] F. Pino, J. C. Delgado, S. M. Carturan, *et al.*, "Novel flexible and conformable composite neutron scintillator based on fully enriched lithium tetraborate," *Scientific Reports*, vol. 13, no. 1, p. 4799, 2023.

[6] A. Favalli, B. W. Wiggins, M. Iliev, *et al.*, "Next-generation neutron detection using a 6li glass scintillator composite," *Communications Physics*, vol. 8, no. 1, p. 10, 2025.

[7] F Pino, L. Stevanato, D. Cester, G Nebbia, L Sajo-Bohus, and G. Viesti, "Detecting fast and thermal neutrons with a boron loaded liquid

scintillator, ej-339a," *Applied Radiation and Isotopes*, vol. 92, pp. 6–11, 2014.

[8] M. Polo, F. Pino, J. C. A. Delgado, D. Fabris, and S. Moretto, "Assessment of a nail detector performance for radiation monitoring applications," *The European Physical Journal Special Topics*, vol. 232, no. 10, pp. 1477–1486, 2023.

[9] H. Pleinert, E. Lehmann, and S. Körner, "Design of a new ccd-camera neutron radiography detector," *Nuclear Instruments and Methods in Physics Research Section A: Accelerators, Spectrometers, Detectors and Associated Equipment*, vol. 399, no. 2, pp. 382–390, 1997, ISSN: 0168-9002. DOI: https://doi.org/10.1016/S0168-9002(97)00944-3. [Online]. Available: https://www.sciencedirect.com/science/article/pii/S0168900297009443.

[10] E. Lukosi, E. Herrera, D. Hamm, *et al.*, "Lithium indium diselenide: A new scintillator for neutron imaging," *Nuclear Instruments and Methods in Physics Research Section A: Accelerators, Spectrometers, Detectors and Associated Equipment*, vol. 830, pp. 140–149, 2016.

[11] E. Herrera, D. Hamm, B. Wiggins, *et al.*, "Lise pixel detector for neutron imaging," *Nuclear Instruments and Methods in Physics Research Section A: Accelerators, Spectrometers, Detectors and Associated Equipment*, vol. 833, pp. 142–148, 2016.

[12] K. Ahmed, R. Dahal, A. Weltz, *et al.*, "Solid-state neutron detectors based on thickness scalable hexagonal boron nitride," *Applied Physics Letters*, vol. 110, no. 2, p. 023 503, 2017.

[13] L. Liu, X. Ouyang, R. Gao, P. Wan, and X. Ouyang, "Latest developments in room-temperature semiconductor neutron detectors: Prospects and challenges," *Science China Physics, Mechanics & Astronomy*, vol. 66, no. 3, p. 232 001, 2023.

[14] G Bruckner, A Czermak, H Rauch, and P Weilhammer, "Position sensitive detection of thermal neutrons with solid state detectors (gd si planar detectors)," *Nuclear Instruments and Methods in Physics Research Section A: Accelerators, Spectrometers, Detectors and Associated Equipment*, vol. 424, no. 1, pp. 183–189, 1999.

[15] D. S. McGregor, M. Hammig, Y.-H. Yang, *et al.*, "Design considerations for thin film coated semiconductor thermal neutron detectors—i: Basics regarding alpha particle emitting neutron reactive films," *Nuclear Instruments and Methods in Physics Research Section A: Accelerators, Spectrometers, Detectors and Associated Equipment*, vol. 500, no. 1-3, pp. 272–308, 2003.

[16] M Voytchev, M. Iñiguez, R Méndez, A Mañanes, L. Rodrıguez, and R Barquero, "Neutron detection with a silicon pin photodiode and 6lif converter," *Nuclear Instruments and Methods in Physics Research Section A: Accelerators, Spectrometers, Detectors and Associated Equipment*, vol. 512, no. 3, pp. 546–552, 2003.

[17] J. Shultis and D. McGregor, "Design and performance considerations for perforated semiconductor thermal-neutron detectors," *Nuclear Instruments and Methods in Physics Research Section A: Accelerators, Spectrometers, Detectors and Associated Equipment*, vol. 606, no. 3, pp. 608–636, 2009, ISSN: 0168-9002. DOI: https://doi.org/10.1016/j.nima.2009.02.033. [Online]. Available: https://www.sciencedirect.com/science/article/pii/S016890020900391X.

[18] S. L. Bellinger, R. Fronk, W. McNeil, *et al.*, "Improved high efficiency stacked microstructured neutron detectors backfilled with nanoparticle ^{6}lif," *IEEE Transactions on Nuclear Science*, vol. 59, no. 1, pp. 167–173, 2011.

[19] Q Shao, L. Voss, A. Conway, R. Nikolic, *et al.*, "High aspect ratio composite structures with 48.5% thermal neutron detection efficiency," *Applied Physics Letters*, vol. 102, no. 6, 2013.

[20] K.-C. Huang, R. Dahal, J. J.-Q. Lu, *et al.*, "High detection efficiency micro-structured solid-state neutron detector with extremely low leakage current fabricated with continuous pn junction," *Applied Physics Letters*, vol. 102, no. 15, 2013.

[21] R. Mendicino and G.-F. Dalla Betta, "Three-dimensional detectors for neutron imaging," *Nuclear Instruments and Methods in Physics Research Section A: Accelerators, Spectrometers, Detectors and Associated Equipment*, vol. 878, pp. 129–140, 2018, Radiation Imaging Techniques and Applications, ISSN: 0168-9002. DOI: https://doi.org/

10.1016/j.nima.2017.07.062. [Online]. Available: https://www.sciencedirect.com/science/article/pii/S0168900217308379.

[22] G.-F. Dalla Betta and M. Povoli, "Progress in 3d silicon radiation detectors," *Frontiers in Physics*, vol. 10, p. 927 690, 2022.

[23] T. Ochs, R. Fronk, S. Bellinger, and D. McGregor, "Design and performance considerations for dual-sided microstructured semiconductor neutron detectors," *Nuclear Instruments and Methods in Physics Research Section A: Accelerators, Spectrometers, Detectors and Associated Equipment*, vol. 951, p. 163 006, 2020.

[24] W. J. McNeil, S. L. Bellinger, T. C. Unruh, *et al.*, "1-d array of perforated diode neutron detectors," *Nuclear Instruments and Methods in Physics Research Section A: Accelerators, Spectrometers, Detectors and Associated Equipment*, vol. 604, no. 1-2, pp. 127–129, 2009.

[25] R. G. Fronk, S. L. Bellinger, L. C. Henson, *et al.*, "Dual-sided microstructured semiconductor neutron detectors (dsmsnds)," *Nuclear Instruments and Methods in Physics Research Section A: Accelerators, Spectrometers, Detectors and Associated Equipment*, vol. 804, pp. 201–206, 2015.

[26] T. Ochs, B. Beatty, S. Bellinger, *et al.*, "Wearable detector device utilizing microstructured semiconductor neutron detector technology," *Radiation Physics and Chemistry*, vol. 155, pp. 164–172, 2019.

[27] R. Nikolić, C. L. Cheung, C. Reinhardt, and T. Wang, "Roadmap for high efficiency solid-state neutron detectors," in *Optoelectronic Devices: Physics, Fabrication, and Application II*, SPIE, vol. 6013, 2005, pp. 36–44.

[28] R. J. Nikolic, A. M. Conway, C. E. Reinhardt, *et al.*, "Pillar structured thermal neutron detector," in *2008 9th International Conference on Solid-State and Integrated-Circuit Technology*, IEEE, 2008, pp. 2361–2364.

[29] P. Singh, G. Dosovitskiy, and Y. Bekenstein, "Bright innovations: Review of next-generation advances in scintillator engineering," *ACS nano*, vol. 18, no. 22, pp. 14 029–14 049, 2024.

[30] Q. Dong, Y. Fang, Y. Shao, *et al.*, "Electron-hole diffusion lengths> 175 μm in solution-grown ch3nh3pbi3 single crystals," *Science*, vol. 347, no. 6225, pp. 967–970, 2015.

[31] D. Shi, V. Adinolfi, R. Comin, *et al.*, "Low trap-state density and long carrier diffusion in organolead trihalide perovskite single crystals," *Science*, vol. 347, no. 6221, pp. 519–522, 2015.

[32] S. D. Stranks and H. J. Snaith, "Metal-halide perovskites for photovoltaic and light-emitting devices," *Nature nanotechnology*, vol. 10, no. 5, pp. 391–402, 2015.

[33] H. Wei and J. Huang, "Halide lead perovskites for ionizing radiation detection," *Nature communications*, vol. 10, no. 1, p. 1066, 2019.

[34] Y. He, L. Matei, H. J. Jung, *et al.*, "High spectral resolution of gamma-rays at room temperature by perovskite cspbbr3 single crystals," *Nature communications*, vol. 9, no. 1, p. 1609, 2018.

[35] F. Maddalena, A. Xie, X. Y. Chin, *et al.*, "Deterministic light yield, fast scintillation, and microcolumn structures in lead halide perovskite nanocrystals," *The Journal of Physical Chemistry C*, vol. 125, no. 25, pp. 14 082–14 088, 2021.

[36] Q. Chen, J. Wu, X. Ou, *et al.*, "All-inorganic perovskite nanocrystal scintillators," *Nature*, vol. 561, no. 7721, pp. 88–93, 2018.

[37] M Kobayashi, K Omata, S Sugimoto, *et al.*, "Scintillation characteristics of cspbcl3 single crystals," *Nuclear Instruments and Methods in Physics Research Section A: Accelerators, Spectrometers, Detectors and Associated Equipment*, vol. 592, no. 3, pp. 369–373, 2008.

[38] V. Mykhaylyk, H Kraus, V Kapustianyk, *et al.*, "Bright and fast scintillations of an inorganic halide perovskite cspbbr3 crystal at cryogenic temperatures," *Scientific Reports*, vol. 10, no. 1, p. 8601, 2020.

[39] A. P. Caricato, S. Moretto, M. R. Guascito, *et al.*, "High scintillation yield and fast response to alpha particles from thin perovskite films deposited by pulsed laser deposition," *Frontiers in Physics*, vol. 10, p. 957 991, 2022.

[40] E. Technology, *Ej-200, ej-204, ej-208, ej-212 – plastic scintillators*, `https://eljentechnology.com/products/plastic-scintillators/ej-200-ej-204-ej-208-ej-212`, Accessed: 2025-09-22, 2021.

[41] A. Quaranta, S Carturan, M Cinausero, *et al.*, "Characterization of polysiloxane organic scintillators produced with different phenyl

containing blends," *Materials Chemistry and Physics*, vol. 137, no. 3, pp. 951–958, 2013.

[42] A. Quaranta, S. M. Carturan, T. Marchi, *et al.*, "Optical and scintillation properties of polydimethyl-diphenylsiloxane based organic scintillators," *IEEE Transactions on Nuclear Science*, vol. 57, no. 2, pp. 891–900, 2010.

[43] M. Bowen, S. Majewski, D. Pettey, J. Walker, R. Wojcik, and C. Zorn, "A new radiation-resistant plastic scintillator," *IEEE Transactions on Nuclear Science*, vol. 36, no. 1, pp. 562–566, 1989. DOI: 10.1109/23.34501.

[44] J Harmon, J Gaynor, V Feygelman, and J Walker, "Linear polydiorganosiloxanes as plastic bases for radiation hard scintillators," *Nuclear Instruments and Methods in Physics Research Section B: Beam Interactions with Materials and Atoms*, vol. 53, no. 3, pp. 309–314, 1991.

[45] C. Zorn, S. Majewski, R. Wojcik, and K. Johnson, "Progress in the design of a radiation-hard plastic scintillator," *IEEE transactions on nuclear science*, vol. 38, no. 2, pp. 194–199, 1991.

[46] G. F. Knoll, *Radiation detection and measurement*. John Wiley & Sons, 2010.

[47] K. S. Krane, *Introductory nuclear physics*. John Wiley & Sons, 1991.

[48] R. D. Evans and R. Evans, *The atomic nucleus*. McGraw-Hill New York, 1955, vol. 582.

[49] M. B. Chadwick, M. Herman, P Obložinskỳ, *et al.*, "Endf/b-vii. 1 nuclear data for science and technology: Cross sections, covariances, fission product yields and decay data," *Nuclear data sheets*, vol. 112, no. 12, pp. 2887–2996, 2011.

[50] G. Lutz *et al.*, "Semiconductor radiation detectors," 2007.

[51] R. Mendicino, "Development of 3d silicon radiation detectors for neutrons and high energy charged particles," Ph.D. dissertation, University of Trento, 2017.

[52] S. Agostinelli, J. Allison, K. Amako, *et al.*, "Geant4—a simulation toolkit," *Nuclear Instruments and Methods in Physics Research Section A: Accelerators, Spectrometers, Detectors and Associated Equipment*, vol. 506, no. 3, pp. 250–303, 2003, ISSN: 0168-9002. DOI: https://doi.org/10.

1016/S0168-9002(03)01368-8. [Online]. Available: https://www.sciencedirect.com/science/article/pii/S0168900203013688.

[53] Synopsys, Inc., *Synopsys TCAD (Technology Computer-Aided Design), Sentaurus Device, Version 2019.12*, Available: https://www.synopsys.com/manufacturing/tcad.html, Accessed: Aug. 26, 2025, 2019.

[54] S. Spannagel, K. Wolters, D. Hynds, *et al.*, "Allpix2: A modular simulation framework for silicon detectors," *Nuclear Instruments and Methods in Physics Research Section A: Accelerators, Spectrometers, Detectors and Associated Equipment*, vol. 901, pp. 164–172, 2018, ISSN: 0168-9002. DOI: https://doi.org/10.1016/j.nima.2018.06.020. [Online]. Available: https://www.sciencedirect.com/science/article/pii/S0168900218307411.

[55] D. Laramore, S. Sharma, K. C. Smallfoot, *et al.*, "Simulation of charge drift in surface doped, pixelated micro-structured semiconductor neutron detectors," *Nuclear Instruments and Methods in Physics Research Section A: Accelerators, Spectrometers, Detectors and Associated Equipment*, vol. 978, p. 164 351, 2020.

[56] S. K. Dwivedi, M. Vishwakarma, and P. Soni, "Advances and researches on non destructive testing: A review," *Materials Today: Proceedings*, vol. 5, no. 2, Part 1, pp. 3690–3698, 2018, 7th International Conference of Materials Processing and Characterization, March 17-19, 2017, ISSN: 2214-7853. DOI: https://doi.org/10.1016/j.matpr.2017.11.620. [Online]. Available: https://www.sciencedirect.com/science/article/pii/S2214785317328936.

[57] Paul Scherrer Institute, *What is neutron imaging?* https://www.psi.ch/en/lns-applied-materials/what-is-neutron-imaging, Accessed: 2025-07-30, n.d.

[58] N. Kardjilov, I. Manke, A. Hilger, *et al.*, "Neutron imaging in materials science," *Materials Today*, vol. 14, no. 6, pp. 248–256, 2011.

[59] K. Hellwege and O Madelung, "Semi-conductor, intrinsic properties of group iv elements and iii–v, ii–vi and i–vii compounds," *Landolt-Bornstein New Series, Group III*, vol. 22, no. 2019, p. 9, 1987.

[60] S. Ramo, "Currents induced by electron motion," *Proceedings of the IRE*, vol. 27, no. 9, pp. 584–585, 1939. DOI: 10.1109/JRPROC.1939.228757.

[61] R. Ballabriga, M. Campbell, and X. Llopart, "An introduction to the medipix family asics," *Radiation Measurements*, vol. 136, p. 106 271, 2020, ISSN: 1350-4487. DOI: https://doi.org/10.1016/j.radmeas.2020.106271. [Online]. Available: https://www.sciencedirect.com/science/article/pii/S1350448720300354.

[62] S. Inc., *Part 2 – what is the bosch process (deep reactive ion etching)?* https://www.samcointl.com/news-events/tutorials/what-is-the-bosch-process/, Accessed: 27 agosto 2025.

[63] R Hezel and K Jaeger, "Low-temperature surface passivation of silicon for solar cells," *Journal of the Electrochemical Society*, vol. 136, no. 2, p. 518, 1989.

[64] M. Barbagallo, L. Cosentino, V. Forcina, *et al.*, "Thermal neutron detection using a silicon pad detector and 6lif removable converters," *Review of Scientific Instruments*, vol. 84, no. 3, p. 033 503, Mar. 2013, ISSN: 0034-6748. DOI: 10.1063/1.4794768. eprint: https://pubs.aip.org/aip/rsi/article-pdf/doi/10.1063/1.4794768/13630653/033503_1_online.pdf. [Online]. Available: https://doi.org/10.1063/1.4794768.

[65] W. M. Haynes, *CRC handbook of chemistry and physics*. CRC press, 2016.

[66] M. Chadwick, M. Herman, P. Obložinský, *et al.*, "ENDF/B-VII.1 nuclear data for science and technology: Cross sections, covariances, fission product yields and decay data," *Nuclear Data Sheets*, vol. 112, no. 12, pp. 2887 –2996, 2011, Special Issue on ENDF/B-VII.1 Library, ISSN: 0090-3752. DOI: 10.1016/j.nds.2011.11.002. [Online]. Available: https://www.sciencedirect.com/science/article/pii/S009037521100113X.

[67] Geant4 Collaboration, *Guide for physics lists*, Release 11.3, Revision 9.0 (6 Dec 2024), Revision 9.1 (14 Jun 2025), CERN, 2024. [Online]. Available: https://geant4.web.cern.ch/documentation/dev/plg_pdf/PhysicsListGuide.pdf.

[68] M. J. Berger, J. Coursey, M. Zucker, J Chang, *et al.*, *Stopping-power and range tables for electrons, protons, and helium ions*. NIST Physics Laboratory Gaithersburg, MD, 1998.

[69] R. Mendicino, A Bagolini, M Boscardin, *et al.*, "Semiconductor neutron detectors," in *Proceedings of Science-24th Workshop on Vertex Detectors (Vertex 2015)*, SISSA, 2015.

[70] C. K. Maiti, *Introducing Technology Computer-Aided Design (TCAD): Fundamentals, Simulations, and Applications*. Jenny Stanford Publishing, 2017.

[71] W. Shockley and W. Read Jr, "Statistics of the recombinations of holes and electrons," *Physical review*, vol. 87, no. 5, p. 835, 1952.

[72] D. J. Roulston, N. D. Arora, and S. G. Chamberlain, "Modeling and measurement of minority-carrier lifetime versus doping in diffused layers of n+-p silicon diodes," *IEEE Transactions on Electron Devices*, vol. 29, no. 2, pp. 284–291, 2005.

[73] P. Dreier, "High resistivity silicon for detector applications," *Nuclear Instruments and Methods in Physics Research Section A: Accelerators, Spectrometers, Detectors and Associated Equipment*, vol. 288, no. 1, pp. 272–277, 1990, Proceedings of the Fifth European Symposium on Semiconductors Detectors, ISSN: 0168-9002. DOI: https://doi.org/10.1016/0168-9002(90)90499-V. [Online]. Available: https://www.sciencedirect.com/science/article/pii/016890029090499V.

[74] S. M. Sze, Y. Li, and K. K. Ng, *Physics of semiconductor devices*. John wiley & sons, 2021.

[75] A. G. Aberle, "Surface passivation of crystalline silicon solar cells: A review," *Progress in Photovoltaics: Research and Applications*, vol. 8, no. 5, pp. 473–487, 2000.

[76] C. Ferrero, C. Neubüser, L. Pancheri, and A. Rivetti, "Monte carlo simulations of fully depleted cmos pixel sensors for radiation detection applications," in *2023 18th Conference on Ph. D Research in Microelectronics and Electronics (PRIME)*, IEEE, 2023, pp. 101–104.

[77] CAEN, "Caen tools for discovery - official site," *https://www.caen.it/*, 2025.

[78] M. Basunia, "Nuclear data sheets for a = 237," *Nuclear Data Sheets*, vol. 107, no. 8, pp. 2323–2422, 2006, ISSN: 0090-3752. DOI: https://doi.org/10.1016/j.nds.2006.07.001. [Online]. Available: https://www.sciencedirect.com/science/article/pii/S0090375206000585.

[79] R. Mendicino and G.-F. Dalla Betta, "A cmos-mems pixel sensor for thermal neutron imaging," *Micromachines*, vol. 14, no. 5, p. 952, 2023.

[80] H. P. K. E. Committee, *PHOTOMULTIPLIER TUBES, Basics and Applications*. Hamamatsu Photonics K.K.Electron Tube Division, 2017.

[81] D. Cester, G. Nebbia, L. Stevanato, F. Pino, L. Sajo-Bohus, and G. Viesti, "A compact neutron–gamma spectrometer," *Nuclear Instruments and Methods in Physics Research Section A: Accelerators, Spectrometers, Detectors and Associated Equipment*, vol. 719, pp. 81–84, 2013, ISSN: 0168-9002. DOI: https://doi.org/10.1016/j.nima.2013.04.032. [Online]. Available: https://www.sciencedirect.com/science/article/pii/S0168900213004373.

[82] F. Acerbi, A. Gola, V. Regazzoni, *et al.*, "High efficiency, ultra-high-density silicon photomultipliers," *IEEE Journal of Selected Topics in Quantum Electronics*, vol. 24, no. 2, pp. 1–8, 2017.

[83] J. R. Lakowicz, *Principles of fluorescence spectroscopy*. Springer, 2006.

[84] T. Forster, "10th spiers memorial lecture. transfer mechanisms of electronic excitation," *Diss. Faraday Soc.*, vol. 27, pp. 7–17, 1959.

[85] J. B. Birks, *The theory and practice of scintillation counting: International series of monographs in electronics and instrumentation*. Elsevier, 2013, vol. 27.

[86] R. Orecchia, M. Krengli, and P. Fossati, "Adroterapia," in *Tumori della testa e del collo: Integrazione terapeutica nella conservazione della funzione d'organo*. Milano: Springer Milan, 2011, pp. 181–194, ISBN: 978-88-470-1806-8. DOI: 10.1007/978-88-470-1806-8_13. [Online]. Available: https://doi.org/10.1007/978-88-470-1806-8_13.

[87] S. M. Carturan, H. Skliarova, G. Franchin, *et al.*, "Additive manufacturing of high-performance, flexible 3d siloxane-based scintillators through the sol-gel route," *Applied Materials Today*, vol. 39, p. 102 313, 2024, ISSN: 2352-9407. DOI: https://doi.org/10.1016/j.apmt.

2024.102313. [Online]. Available: https://www.sciencedirect.com/science/article/pii/S2352940724002580.

[88] J. Ghosh, J. O'Neill, M. G. Masteghin, *et al.*, "Surfactant-dependent bulk scale mechanochemical synthesis of cspbbr3 nanocrystals for plastic scintillator-based x-ray imaging," *ACS applied nano materials*, vol. 6, no. 16, pp. 14 980–14 990, 2023.

[89] S. Mourdikoudis and L. M. Liz-Marzán, "Oleylamine in nanoparticle synthesis," *Chemistry of Materials*, vol. 25, no. 9, pp. 1465–1476, 2013.

[90] M. Giancaspro, R. Grisorio, G. Alò, *et al.*, "Molecular insights into the growth and time evolution of surface states of cspbbr 3 nanoparticles synthesized using a scalable room temperature approach," *Materials Chemistry Frontiers*, vol. 7, no. 13, pp. 2637–2650, 2023.

[91] M. Hamel, *Plastic scintillators*. Springer, 2021.

[92] M. Calora, A. Giuri, N. Vanni, *et al.*, "2d metal-halide perovskite-thin polycrystalline films enable bright and fast scintillations," *ACS Applied Optical Materials*, vol. 2, no. 5, pp. 862–870, 2024.

[93] C. L. Fontana, M. Lunardon, F. E. Pino, *et al.*, "A distributed data acquisition system for signal digitizers with on-line analysis capabilities," in *2017 IEEE Nuclear Science Symposium and Medical Imaging Conference (NSS/MIC)*, 2017, pp. 1–5. DOI: 10.1109/NSSMIC.2017.8533063.

[94] A. Giuri, A. C. Chekkallur, M. Calora, *et al.*, "3d printed ultra-fast plastic scintillators based on perovskite-photocurable polymer composite," *Advanced Functional Materials*, vol. 35, no. 12, p. 2 417 653, 2025.

[95] M. Chiari, A Migliori, and P. Mandò, "Measurement of low currents in an external beam set-up," *Nuclear Instruments and Methods in Physics Research Section B: Beam Interactions with Materials and Atoms*, vol. 188, no. 1-4, pp. 162–165, 2002.